Analysis of metallofullerenes using a mass reflectron

V. I. Karataev

A. F. Ioffe Physicotechnical Institute, Russian Academy of Sciences, St. Petersburg
(Submitted October 15, 1997)
Pis'ma Zh. Tekh. Fiz. **24**, 1–5 (March 12, 1998)

A high-resolution mass reflectron has been used to analyze an extract of a fullerene mixture containing the metallofullerene $Gd@C_{82}$. It is shown that various metallofullerenes can be analyzed by means of thermal desorption followed by electron impact ionization. The C_{60}, C_{82}, and $Gd@C_{82}$ ion currents are obtained as functions of the evaporation temperature. Doubly charged $(Gd@C_{82})^{2+}$ metallofullerene ions are identified in the mass spectra. © *1998 American Institute of Physics.* [S1063-7850(98)00103-7]

Mass spectrometry is one of the fundamental methods of analyzing fullerenes and metallofullerenes.[1,2] The gadolinium-containing fullerene C_{82}, conventionally denoted as $Gd@C_{82}$, is considered here. The samples were analyzed by a technique which involves thermal desorption by electrical heating followed by electron-impact ionization of the vapor and separation of the product positive ions in a ''mass reflectron'' time-of-flight mass spectrometer.[3] When this technique is applied to fullerenes,[4] a sample in the form of soot particles, an extract, or a solution of fullerenes in organic solvents weighing ~ 0.1 mg, is placed in a ~ 5 mm^3 quartz crucible and inserted in an electrically heated tantalum furnace fitted with a thermocouple. The maximum heating temperature is ~ 900 °C. The rate of heating can be varied between 10 and 100 °C/min. The energy of the ionizing electrons can be varied between 5 and 100 eV.

The composition of the fullerene ions in the mass spectrum depends on the evaporation temperature of the sample, and as the temperature increases, a gradual yield of heavier clusters is observed for both fullerenes and metallofullerenes. Figure 1 gives the C_{60}, C_{82}, and $Gd@C_{82}$ ion current as a function of the sample evaporation temperature. It can be seen that fullerenes of different mass exhibit different thermal desorption kinetics. Desorption of C_{82} and $Gd@C_{82}$ takes place at almost the same temperature but with an appreciable shift toward higher temperature for the metallofullerene. The evaporation curves have a similar profile. The minimum desorption temperature for $Gd@C_{82}$ was ≈ 400 °C. It should be noted that in the thermal desorption technique the quantitative result of the analysis is an averaged value obtained for total evaporation of the sample, so that it is more accurate to measure the total ion currents of all types of fullerenes over the entire evaporation time, for which the maximum evaporation temperature should ensure evaporation of the heaviest clusters. The composition of the sample vapor is frequently given at a particular evaporation temperature, which provides sufficient information.

Figure 2 gives the complete mass spectrum of the fullerenes in this extract sample at $T = 600$ °C. An increased content of heavy fullerenes is observed, extending as far as C_{120}. The mass reflectron can resolve all combinations of Gd isotopes with C_{82} isotope lines, as can be seen clearly from Fig. 3, which shows part of the mass spectrum between C_{94} and C_{96}, including the $Gd@C_{82}$ metallofullerene lines with masses between 1138 and 1148 u. Doubly charged $Gd@C_{82}^{2+}$ ions were recorded along with the singly charged ions, and the ratio of the singly charged to the doubly charged ion current was similar to the ratio C_{82}^{+}/C_{82}^{2+} for empty fullerenes. It is interesting to note that the $Gd@C_{82}/C_{82}$ current ratio which characterizes the efficiency of the yield of filled fullerenes to empty fullerenes was ~ 0.5.

On the basis of these results, it may be concluded that some metallofullerenes possess extremely good thermal stability and that prolonged thermal action does not impair their integrity, as had been supposed previously.[2] It should be noted that the thermal desorption method gives fairly reproducible results and in particular, does not depend on the homogeneity of the sample microstructure. The dependence of the mass spectrum of metallofullerenes on the method of conversion of the molecules to the gas phase[2,5] is a major disadvantage of mass spectrometric analysis. In this respect, the thermal desorption method is potentially useful for analyzing metallofullerenes, since it has a minimal affect on the initial composition of the sample.

Thus, the method of thermal desorption followed by electron impact ionization of the vapor in a conventional ion source can be used in the mass spectrometric analysis of various metallofullerenes. Another commonly used method

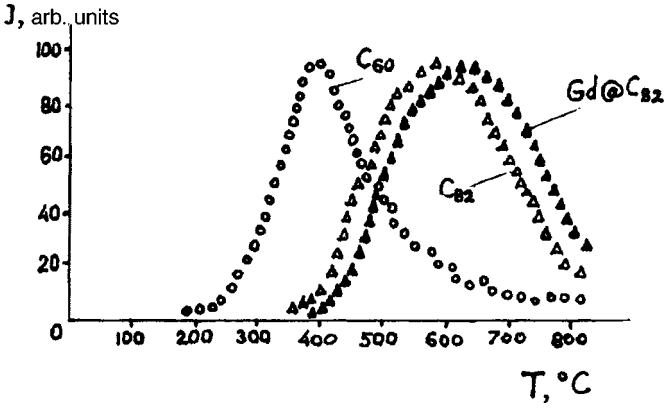

FIG. 1. C_{60}, C_{82}, and $Gd@C_{82}$ ion current versus evaporation temperature of sample.

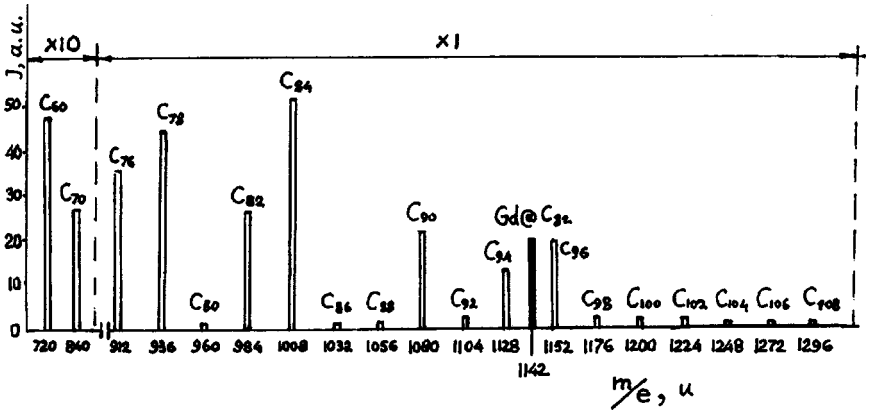

FIG. 2. Complete mass spectrum of fullerene extract containing $Gd@C_{82}$ metallofullerene at T_{ev}=600 °C.

involves laser desorption of the sample followed by ionization of the vapor using another laser which delivers a photoelectron flux. It should be noted that both methods give similar qualitative results for the same sample but differ quantitatively as a result of the very different conditions used to convert the molecules to the gas phase, i.e., the temperature and duration of the action on the sample material.

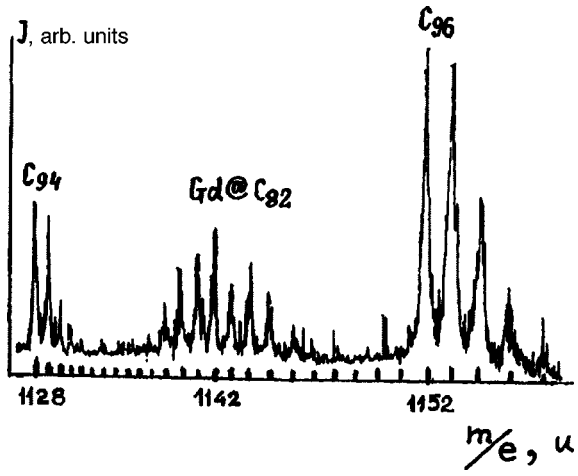

FIG. 3. Thermal desorption section of the mass spectrum of the extract between C_{94} and C_{96} including $Gd@C_{82}$ isotopic multiplets with masses between 1138 and 1148 u.

To conclude, the author is deeply grateful to Yu. S. Grushko (St. Petersburg Institute of Nuclear Physics, Russian Academy of Sciences) for kindly supplying samples of $Gd@C_{82}$ metallofullerene.

This work was carried out under Project No. 94006 as part of the Russian Scientific-Technical Program ''Fullerenes and Atomic Clusters.''

[1] D. C. Bethune, R. D. Johnson, J. R. Salem, M. S. De Vries, and C. S. Yannoni, Nature **366**(11), 123 (1993).
[2] L. Moro, R. S. Ruoff, C. H. Becker, D. C. Lorents, and R. Malhotra, J. Phys. Chem. **97**, 6801 (1993).
[3] B. A. Mamyrin, V. I. Karataev, D. V. Shmikk, and V. A. Zagulin, Zh. Éksp. Teor. Fiz. **64**, 82 (1973) [Sov. Phys. JETP **37**, 45 (1973)].
[4] V. I. Karataev, Pis'ma Zh. Tekh. Fiz. **19**(15), 65 (1993) [Tech. Phys. Lett. **19**, 498 (1993)].
[5] C. S. Yannoni *et al.*, Synth. Met. **59**, 279 (1993)

Translated by R. M. Durham

Cross linking and thermal destruction processes in thin films formed from dilute solutions of a copolymer of trifluorochloroethylene and vinylidene fluoride

A. O. Pozdnyakov, B. M. Ginzburg, O. F. Pozdnyakov, and B. P. Redkov

Institute of Problems in Mechanical Engineering, Russian Academy of Sciences, St. Petersburg;
A. F. Ioffe Physicotechnical Institute, Russian Academy of Sciences, St. Petersburg
(Submitted August 20, 1997)
Pis'ma Zh. Tekh. Fiz. **24**, 6–10 (March 12, 1998)

Thermal desorption mass spectrometry has been used to investigate the mechanisms for thermal destruction of films prepared from dilute solutions of a copolymer of trifluorochloroethylene and vinylidene fluoride. It is shown that compared with films obtained from concentrated solutions, the ratio of the intensities of the low- and high-temperature stages of HCl and HF release changes substantially in this case. It is concluded that the low-temperature stage of hydrogen halide release is attributable to cross-linking processes rather than to intramolecular reactions caused by the formation of double bonds in the chain. © *1998 American Institute of Physics.* [S1063-7850(98)00203-1]

It has been shown in various studies[1–3] that the monotonic heating of the copolymer of trifluorochloroethylene and vinylidene fluoride is accompanied by the two-stage release of hydrogen halides (HF and HCl). In an earlier study[4] we noted that the high-temperature stage is observed in the same temperature range as the yield of chain destruction products. Since the solubility of the copolymer decreases at the low-temperature stage of hydrogen halide formation,[1–3] we attributed[4] this release of hydrogen halides to the formation of intermolecular cross links. At the same time, some cross links may also be formed between independent sections of the same chain (intramolecular cross links). In addition to this mechanism of hydrogen halide formation at the low-temperature stage, there is also an alternative mechanism caused by intramolecular HF and HCl detachment reactions accompanied by the formation of a system of conjugate bonds. This mechanism is confirmed by a change in the color of the samples and by the detection of double bonds through infrared spectroscopy.[1–3] Thus, there are two possible mechanisms for the release of hydrogen halides at the low-temperature stage. In view of this, we used thermal desorption spectroscopy to carry out experiments which confirmed one of these mechanisms, i.e., cross linking. Information on the materials and experimental method can be found in Ref. 4.

The concept of the experiments is as follows. It is known that when polymers crystallize, the degree of ordering (crystallinity) depends very strongly on the crystallization conditions.[5] In particular, it has been established that the crystallization conditions strongly influence the structure of the copolymer.[6] During crystallization from melts or concentrated solutions, steric hindrances always increase the fraction of noncrystallizing sections of the chains, which form an amorphous phase (Fig. 1a). However, highly dilute solutions, from which the solvent evaporates very slowly,[5] are used to obtain polymer single crystals (Fig. 1b). It is quite clear that the maximum number of contacts between different macromolecules or independent sections of the same macromolecule is achieved for single crystals (in both cases we shall call these contacts ''interchain contacts''). These contacts only participate in the formation of hydrogen halides by cross linking, not by the formation of double bonds. Note that the increased number of interchain contacts formed in films obtained from dilute solutions is clearly conserved when these films are then heated above the melting point, as a result of the well-known ''genetic memory'' effect.[7,8] Thus, if the release of hydrogen halides at the low-temperature stage is caused by cross-linking reactions, an increase in the number of contacts should lead to an increased probability of intermolecular contacts between halogen atoms and hydrogen atoms, and thereby increase the quantity of released hydrogen halides. However, if the mechanism of hydrogen halide formation is the result of intrachain recombination between neighboring halogen and hydrogen atoms, this dependence should not be found.

To vary the number of interchain contacts, we prepared copolymer films from dilute ethyl acetate solutions (initial concentration less than 0.05%). The temperature dependence

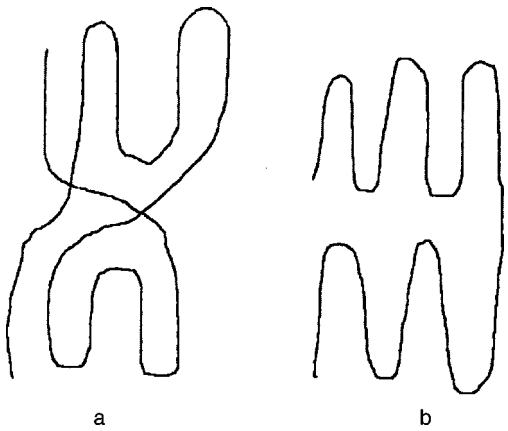

FIG. 1. Diagram showing supermolecular organization of a polymer formed by crystallization from a concentrated solution or melt (a) and from a dilute solution (b).

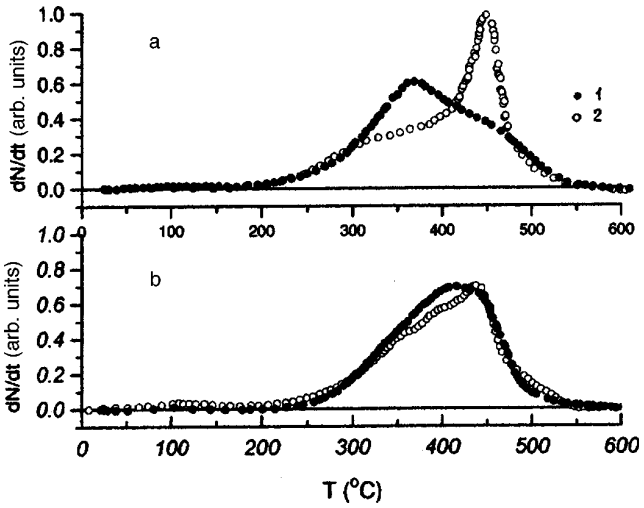

FIG. 2. Temperature dependences of the formation of HCl (a) and HF (b) by heating films prepared on the surface of a steel substrate using a dilute solution (around 0.05 wt. %) shown by the filled circles (*1*) and films formed from a concentrated solution shown by the empty circles (*2*). Rate of heating ~10 K/s.

of the formation of the main volatile products (HCl and HF) obtained for these films differed substantially from that obtained by heating films prepared from more concentrated solutions (initial concentration higher than 2–3%). For convenience of comparison, the curves giving the formation of HCl (Fig. 2a) and HF (Fig. 2b) obtained by heating films prepared from dilute and concentrated copolymer solutions are normalized to the quantity of heated sample.

A comparison of the curves reveals that the concentration of the initial polymer solution has two main effects on the formation of volatile products. The first involves a substantial increase in the intensity of the low-temperature hydrogen halide formation peak compared with the high-temperature peak for films obtained from the dilute solution. The second effect involves a reduction in the specific quantity of chain destruction products which is evidenced by a decrease in the specific quantity of hydrogen compounds other than halides and of one of the comonomers—CF_2CFCl—at the high-temperature stage (not shown in the Figure; see Ref. 4 for the release kinetics of the comonomer). From this it follows that the formation of hydrogen halides at the low-temperature stage is undoubtedly caused by the creation of interchain contacts. Quantitative estimates show that for films obtained from dilute solutions, the cross-linking density increases by approximately an order of magnitude, i.e., is 10–20 links per two macromolecules as compared with 1–2 for films obtained from concentrated solutions.

This work was carried out as part of the Russian Scientific-Technical Program ''Fullerenes and Atomic Clusters'' (''Tribol'' project).

[1] T. G. Degteva, Vysokomol. Soedin. **3**(5), 671 (1961).
[2] T. G. Degteva, I. M. Sedova, and A. S. Kuz'minskiĭ, Vysokomol. Soedin. **5**(3), 378 (1963).
[3] T. G. Degteva, I. M. Sedova, and A. S. Kuz'minskiĭ, Vysokomol. Soedin. **5**(10), 1485 (1963).
[4] A. O. Pozdnyakov and B. M. Ginzburg, Pis'ma Zh. Tekh. Fiz. **23**(17), 87 (1997) [Tech. Phys. Lett. **23**, 694 (1997)].
[5] P. H. Geil, *Polymer Single Crystals* (Wiley Interscience, New York, 1963; Leningrad, 1968).
[6] G. C. Adams and R. J. Stein, J. Polymer Sci. A2 **6**, 31 (1968).
[7] V. G. Baranov and K. A. Gasparyan, J. Polymer Sci. A2 **8**, 1015 (1970).
[8] J. Petermann and H. Gleiter, J. Macromol. Sci. B **11**, 359 (1975).

Translated by R. M. Durham

Bistability and response to hydrogen adsorption in nanostructured films based on mixed tin and titanium oxides

B. Sh. Galyamov, S. A. Zav'yalov, G. G. Postovalova, and Yu. E. Roginskaya

L. Ya. Karpov Physicochemical Scientific-Research Institute, Moscow
(Submitted August 4, 1997)
Pis'ma Zh. Tekh. Fiz. **24**, 11–16 (March 12, 1998)

It is shown that the strong response to hydrogen adsorption exhibited by the electrical conductivity of thin nanostructured films based on mixed tin and titanium oxides and its rapid relaxation to the initial value in an adsorption–desorption cycle are caused by the ''trigger'' properties of this system relative to changes in the composition of the gaseous atmosphere. © *1998 American Institute of Physics.* [S1063-7850(98)00303-6]

The strong response of the electrical conductivity σ to adsorption of molecular hydrogen exhibited by nanostructured films formed of mixed tin and titanium oxides (subsequently called 10ST, where the coefficient indicates the content of the titanium component in mol.%) suggests that these materials may be potentially useful gas-sensitive elements for use in gas sensors.[1,2] The increase in the electrical conductivity of ST films accompanying the adsorption of H_2 is similar to that resulting from strong metal–carrier interaction in oxides, particularly TiO_2, with deposited particles of platinum-group metals, in which σ also increases in the presence of hydrogen. It is postulated that this effect is caused by reduction of the carrier as a result of hydrogen spillover from the metal to the oxide, with the hydrogen diffusing to the carrier in the form of protons.[3] However, unlike a metal–carrier system, the particles dispersed in a 10ST film are nanometer-scale interacting oxide–titanium particles combined to form ensembles, rather than metal particles.[1,4] It is thus predicted that the adsorption response of the electrical conductivity of these systems may have a certain specificity. This is the main focus of the present study.

As in Refs. 1 and 2, the films were prepared by coprecipitation of solutions of tin and titanium chlorides on quartz substrates coated with a conducting ITO layer, followed by thermolysis at 450°. The samples obtained were thin (of the order of 100 nm) transparent films. The electromechanical characteristics were determined by a conventional technique using a 1N H_2SO_4 solution.

Figure 1 shows an image of part of the surface of an 10ST film obtained by scanning tunneling microscopy, which shows that the samples are inhomogeneous at the nanometer scale. The maximum particle sizes do not exceed 20 nm. Precision x-ray phase analysis and x-ray photoelectron spectroscopy revealed that away from the surface these particles consist of a partially crystallized, hydrated formation, enriched in the titanium oxide component, no larger than 10 nm (i.e., the oxide–titanium particles are in fact hydrated solid solutions) and an outer shell formed predominantly of disordered tin oxides. No distinct boundary exists between the core and the shell with continuations of the shell in the form of extended inclusions of amorphous SnO_2 being observed in the oxide–titanium particles. Samples of other compositions do not exhibit this nanoheterogeneity: 5ST films are single-phase solid solutions of tin and titanium oxides while 15ST films are two-phase solid solutions of the same oxides with particle sizes between two and three times greater.

In order to study effects associated with proton transport, oxidation and reduction processes (redox processes) in ST films of different composition were investigated by cyclic measurement of the current–voltage characteristics in acidic electrolyte solutions. Cycling was carried out in a range of potentials which eliminates other electrochemical processes associated with charge exchange between the electrode and the electrolyte. Typical current–voltage characteristics are plotted in Fig. 2, which clearly shows that the 10ST films have the highest electrical capacitance. This observation is quite consistent with previous results which suggest that the 10ST sample is an extremely sensitive adsorbent for molecular hydrogen.[1,2] Redox processes also take place at TiO_2 and SnO_2 electrodes, but are considerably weaker.

Similar processes for 5ST and 15ST films are comparable with those for 10ST, which is unexpected since the electrical conductivity of these films has a response to adsorption of molecular hydrogen similar to that of TiO_2 and SnO_2 films. From this it can be concluded that like 10ST, the 5ST and 15ST films are good proton acceptors, but unlike 10ST, they are not very sensitive to the adsorption of molecular hydrogen. Thus, the 10ST film must contain adsorption centers not present in samples of different composition, at which hydrogen is activated and then migrates as H^+ over the film. In the absence of any activator center the filmis unaffected by the adsorption of molecular hydrogen.

The nature of these centers, which are unique to 10ST, may be identified by analyzing its real structural characteristics. As was noted in Refs. 1 and 2, only in 10ST films are all the electrons localized in oxide–titanium particles dispersed in the matrix with no conduction electrons being present. As a result, the usual screening is impossible and the nanoparticles combine to form extended ensembles in which all the oxide–titanium particles are intercoupled by electrostatic forces of attraction or repulsion. The corresponding electric

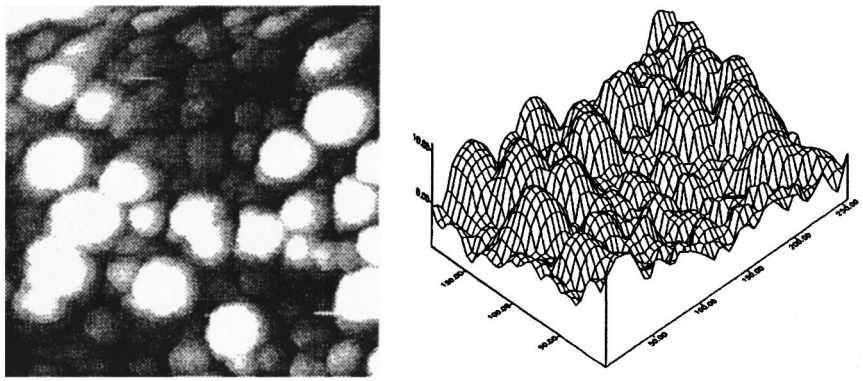

FIG. 1. Scanning tunneling microscope image of part of the surface of 10ST film. Left—relief topology, right—three-dimensional representation. Scan: 130×130 nm. The maximum height of the irregularities is less than 20 nm.

field strength between these particles may reach 10^5 V/cm. It is known that the rate constant of chemical reactions in a strong electric field is an exponentially increasing function of its strength, so that the most probable centers for dissociative chemisorption of hydrogen are local sections of the matrix between interacting oxide–titanium particles. These fields are responsible for separation of the protons and electrons and their subsequent migration to different oxide–titanium particles.

As a result of this charge redistribution, the functional properties of various sections of the film undergo local changes. Electrons are localized near some oxide–titanium particles and are involved in the reduction of their nearest neighbors. According to Ref. 3, this reduction not only suppresses the acidity of the surface but also increases the concentration of proton acceptors, thereby promoting further dissociative chemisorption of hydrogen. Protons are injected into the hydrated oxide–titanium particles along extended inclusions of amorphous SnO_2, creating local fluctuations in the density of proton-containing particles. This results in disproportionation of Ti(III) ions, for example to give Ti(IV) and a Ti(II) ion, which is unstable in a proton medium and is oxidized rapidly and irreversibly in the presence of water by a reaction of the form

$$=\mathrm{Ti(II)}\ldots\mathrm{OH_2}\rightarrow=\mathrm{Ti(IV)}=\mathrm{O}+\mathrm{H_2}.$$

This reaction is thermodynamically favorable, since the redox potential is $\mathrm{Ti}^{2+}/\mathrm{Ti}^{4+}=-0.5$ V, which makes this process irreversible.[5] Thus, dissociative chemisorption of hydrogen at ensembles of interacting oxide–titanium particles creates effective adsorption centers which are probably responsible for the rapid relaxation of σ to its initial value for the 10ST film after the removal of hydrogen from the gas phase.

The reversibility of the adsorption response of the electrical conductivity suggests that the initial structure and composition of the 10ST films are stable. The electron distribution is thermodynamically nonequilibrium. This conclusion is supported by the results of an investigation of the photoconductivity in the absence of hydrogen.[4] The photogenerated electron–hole pairs in the tin oxide matrix are separated by the electrostatic fields between the interacting particles. Nonequilibrium holes, migrating along random fields, reach oxide–titanium particles and recombine with localized electrons. As a result, without any change in its composition, the 10ST system also becomes equilibrium in terms of charge, i.e., is converted to a stable state, which is observed as an irreversible change in the electrical conductivity under illumination.[4]

To conclude, controlled thermohydrolysis conditions can be used to prepare thin films whose structure and composition are stabilized before thermodynamic charge equilibrium is established. In the absence of external influences, the initial state is stable (slow sample aging processes are not considered here). Dissociative adsorption of hydrogen takes place in the surface layer of nanoparticles and is initiated by the strong fields which bind these particles into ensembles while desorption takes place via hydrated oxide–titanium particles. During adsorption, the composition of the film changes and the system is converted from the initial metastable state to another charge-equilibrium state which is only

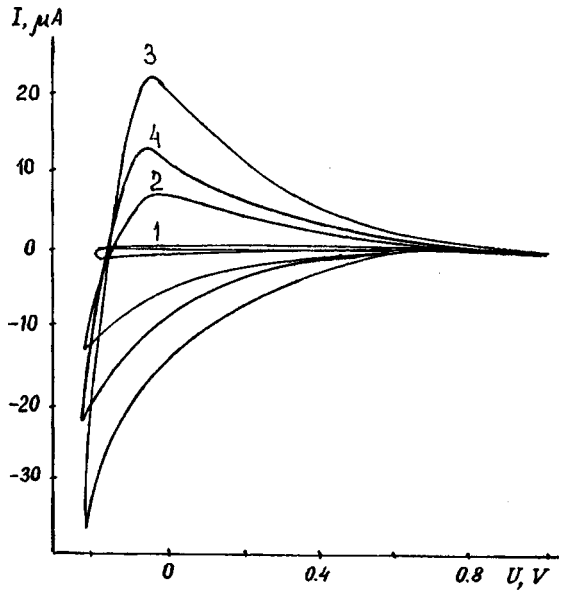

FIG. 2. Cyclic current–voltage characteristics of ST films of different composition in 1N H_2SO_4 solution: *1*—SnO_2, *2*—5 ST, *3*—10 ST, *4*—15 ST. The potentials are given relative to a silver chloride electrode.

stable in a hydrogen atmosphere. When the hydrogen is removed, the system relaxes rapidly to the initial state. Thus, the hydrogen adsorption–desorption processes are accompanied by relaxation of the system between different metastable states and the reversible adsorption response is caused by the ''trigger'' properties of the 10TS film relative to changes in the composition of the gas atmosphere.

This work was supported by the Russian Fund for Fundamental Research.

[1] B. Sh. Galyamov and S. A. Zav'yalov, Pis'ma Zh. Tekh. Fiz. **22**(21), 14 (1996) [Tech. Phys. Lett. **22**, 869 (1996)].
[2] B. Sh. Galyamov, S. A. Zav'yalov, O. V. Morozova, L. A. Zav'yalova, L. Yu. Kupriyanov, and Yu. E. Roginskaya, Zh. Fiz. Khim. **69**, 1071 (1995).
[3] V. V. Rozanov and O. V. Krylov, Usp. Khim. **66**(2), 117 (1997).
[4] B. Sh. Galyamov and S. A. Zav'yalov, Pis'ma Zh. Tekh. Fiz. **20**(17), 77 (1994) [Tech. Phys. Lett. **20**, 716 (1994)].
[5] N. T. Denisov, S. I. Kobeleva, and A. F. Shestakov, Kinet. Katal. **33**, 1055 (1991).

Translated by R. M. Durham

Distortion of the spatial distribution of a laser beam reflected by a VO_2 mirror

A. I. Sidorov

Scientific-Research Institute of Laser Physics, S. I. Vavilov State Optical Institute Scientific Center, St. Petersburg

(Submitted July 8, 1997)
Pis'ma Zh. Tekh. Fiz. **24**, 17–22 (March 12, 1998)

The switching of controllable VO_2 mirrors with $dR/dT>0$ or $dR/dT<0$ under the action of a Gaussian-profile laser beam is modeled. It is shown that when a high-intensity laser beam is reflected by a VO_2 mirror, it undergoes appreciable spatial distortion during switching. © *1998 American Institute of Physics.* [S1063-7850(98)00403-0]

The change in the reflection coefficient of a vanadium dioxide (VO_2) film accompanying a reversible semiconductor–metal phase transition[1] has been used to fabricate controllable mirrors for the visible[1] and for the middle infrared.[2,3] It was shown in Ref. 3 that multilayer VO_2 mirrors with $dR/dT>0$ or $dR/dT<0$ may be fabricated for $\lambda = 3-11$ μm, where the reflection coefficient varies between $R_{\min}=5-10\%$ and $R_{\max}=95-98\%$ as the temperature of the VO_2 film varies. When these mirrors are used to control laser radiation (including intracavity control[2,6]), the heat from a high-intensity laser beam may be an additional factor, or even the main factor, responsible for switching the mirror.[6] When a VO_2 mirror is exposed to a spatially inhomogeneous laser beam, the reflection coefficient of the VO_2 mirror will be spatially modulated, which will distort the spatial distribution of the reflected beam. Here the deformation of a laser beam with a Gaussian profile reflected by VO_2 mirrors with $dR/dT>0$ and $dR/dT<0$ is modeled for the case where the laser beam is the main factor responsible for switching the VO_2 mirror.

The VO_2 mirror is a multilayer thin-film interference system incorporating a VO_2 film (of thickness $h = 0.2-0.3$ μm) deposited on a thick substrate. The reflection coefficient of the mirror as the temperature of the VO_2 film changes may be approximated by the linear functions

$$R(T)=\begin{cases} R_{\min}(R_{\max}), & T\leqslant 60\ ^\circ\mathrm{C}, \\ R_{\min}(R_{\max})+(-)\alpha[T-60], & 60\leqslant T\leqslant 70\ ^\circ\mathrm{C}, \\ R_{\max}(R_{\min}), & T\geqslant 70\ ^\circ\mathrm{C}, \end{cases} \tag{1}$$

where the symbols in parentheses refer to mirrors with $dR/dT<0$, and $\alpha=0.1$ ($R_{\max}$–$R_{\min}$). The following expression is valid for VO_2 mirrors with a thin ($h\approx 0.1$ μm) metal film inserted between the interference system and the substrate,[3]

$$J_{\mathrm{ab}}(T)=J_{\mathrm{inc}}[1-R(T)], \tag{2}$$

where J_{ab} is the power density of the radiation absorbed by the VO_2 film and J_{inc} is the intensity of the incident radiation on the mirror. The absorption coefficient of VO_2 is between three and four orders of magnitude higher than that of the other materials contained in the interference system of the mirror. Thus, the heat release accompanying the absorption of radiation is concentrated mainly in the VO_2 film. However, for $t>1$ μs the temperature becomes equalized all the way through the interference system because of its small thickness. This means that in the thermophysical sense, the system can be considered to be a homogeneous body with averaged thermophysical parameters. For typical film materials used in the interference system of a VO_2 mirror designed for $\lambda=10.6$ μm—ZnSe, ZnS, Ge, and BaF_2—the average thermophysical parameters are $d=5.1$ g/cm^3, $c=0.45$ J/gK, and $k=0.2$ W/cm·K. Thus, the thermal mirror model may be reduced to the approximation of an unbounded homogeneous plate in thermal contact with a semibounded homogeneous body. In cases of high radiation intensity and short heating times, the influence of heat conduction along the surface of the mirror can be neglected. Then the heat source formed on the VO_2 mirror by the radiation may be represented by means of point sources. According to Ref. 7, the temperature at the surface of the mirror for each source is then given by

$$T(t)=\frac{4J^*\sqrt{t}}{\eta_1(1+K)}\sum_{n=0}^{\infty}M^n\times ierfc\left(\frac{2n+1}{2\sqrt{\mathrm{Fo}}}\right), \tag{3}$$

where $\eta=(kcd)^{1/2}$, k is the thermal conductivity, c is the specific heat, d is the specific weight, $\vartheta=k/dc$ is the thermal diffusivity, $K=\eta_2/\eta_1$, the subscripts 1 and 2 refer to the film and the substrate, respectively, $M=(1-K)/(1+K)$, and J^* is the specific power of the heat source, and $\mathrm{Fo}=\vartheta t/h^2$ is the Fourier criterion. In accordance with expression (2), J^* may be given by

$$J^*(t,r)=J_0\exp[-(r/r_0)^2](1-R(t,r)), \tag{4}$$

where r_0 is the radius of a Gaussian source at the $1/e$ level, and J_0 is the radiation intensity at its center. The intensity of the radiation reflected by the VO_2 mirror is given by

$$J_{\mathrm{ref}}(t,r)=J_0\exp[-(r/r_0)^2]R(t,r). \tag{5}$$

The modeling was performed for a VO_2 mirrors and laser beam with the parameters $R_{\min}=5\%$, $R_{\max}=98\%$, $\alpha=0.093$, $J_0=2$ kW/cm^2, $r_0=3.2$ mm, and the substrate material was SiO_2.

Figure 1 shows the temporal variation in the reflection coefficient of a VO_2 mirror with $dR/dT>0$ under the action of a laser beam (a) and the change in the profile of the re-

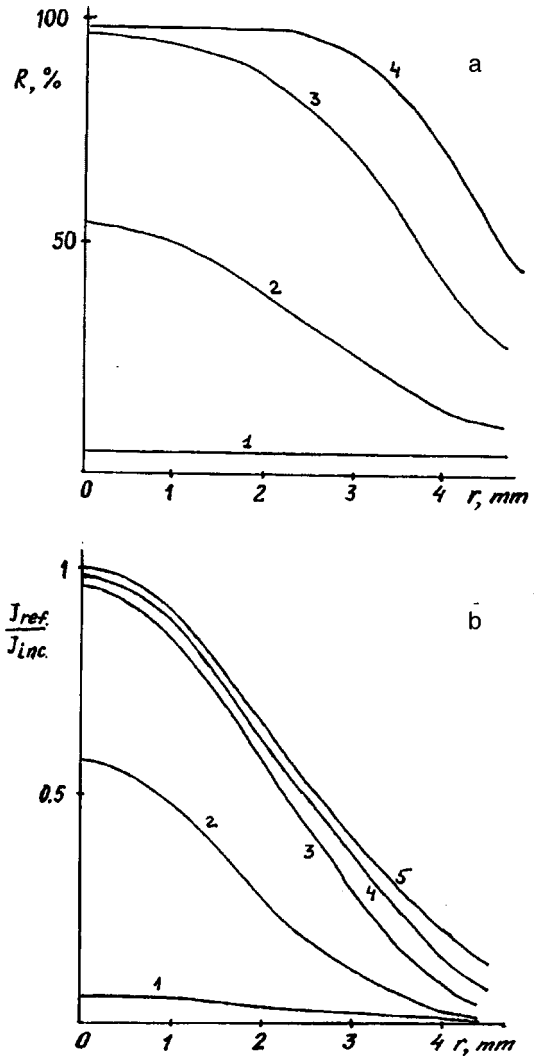

FIG. 1. Changes in the profile of the reflection coefficient (a) and profile of the reflected beam (b) during switching of a VO_2 mirror with $dR/dt>0$: *1*—$t=0$ μs, *2*—3, *3*—10, *4*—20, and *5*—$J_{inc}(r)$.

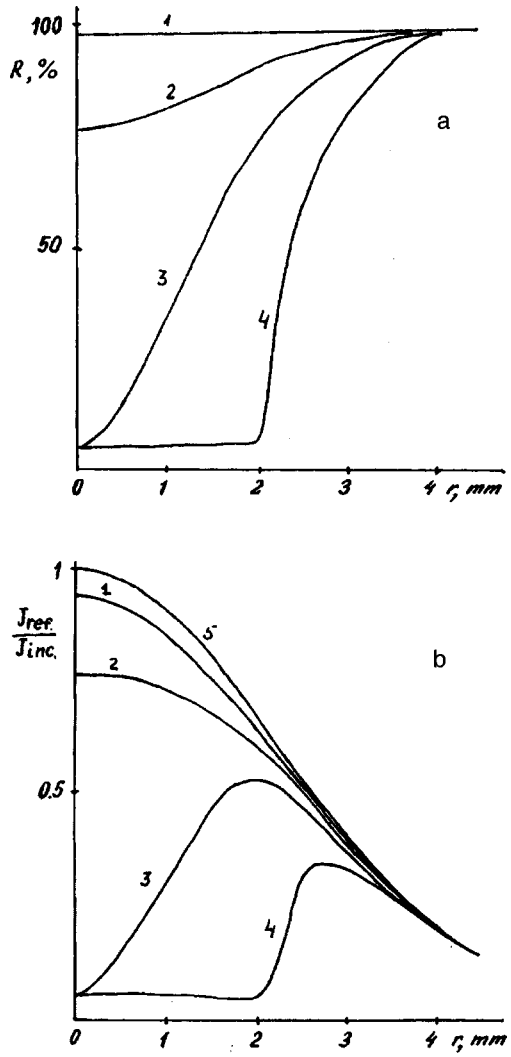

FIG. 2. Changes in the profile of the reflection coefficient (a) and profile of the reflected beam (b) during switching of a VO_2 mirror with $dR/dt>0$: *1*—$t=0$ μs, *2*–10, *3*—15, *4*—25, and *5*—$J_{inc}(r)$.

flected beam (b). At $t=0$ the mirror is homogeneous and the profile of the reflected beam corresponds to that of the initial beam. For $t<1$ μs $J_{ref}(r)$ narrows to approximately 0.7 of the width of $J_{inc}(r)$ (at the $1/e$ level). As R increases in the central part of the mirror, the region of maximum absorption of radiation by the mirror shifts to the wings of the distribution, causing a reduced rate of increase of R in the central part of the mirror and broadening of the profiles $R(r)$ and $J_{ref}(r)$. When the reflection coefficient reaches R_{max}, the part of the beam reflected from the region with R_{max} reproduces the initial profile of the beam, while at the wings of the distribution, distortion is observed up to $t\approx 40$ μs.

It can be seen from Figs. 2a and 2b that when a VO_2 mirror with $dR/dT<0$ is switched by radiation, the profile of the reflected beam shows stronger distortion in comparison with that described above. As R decreases in the central part of the mirror, the central part of the reflected beam profile is ''cut out'' with the initial distribution conserved at the wings. After the central part of the mirror has reached R_{min}, the part of the beam reflected from this region reproduces the initial profile.

It can be seen from these examples that when VO_2 mirrors are used as switches for high-intensity laser radiation, the spatial distribution of the reflected beam undergoes appreciable distortions at the switching stage. When VO_2 mirrors are used inside cavities, these effects may lead to deformation of the laser cavity modes.

[1] A. A. Bugaev, B. P. Zakharchenya, and F. A. Chudnovskiĭ, *Metal–Semiconductor Phase Transition and its Applications* [in Russian], Nauka, Leningrad (1979), 183 pp.
[2] J. S. Chivian, M. W. Scott, W. E. Case *et al.*, IEEE J. Quantum Electron. **QE-21**, 383 (1985).
[3] O. B. Danilov, O. P. Konovalova, A. L. Sidorov, and I. I. Shaganov, Technical Digest of Papers Presented at the Eighth Laser Optics Conference, St. Petersburg, 1995, Vol. 2, p. 55.
[4] O. P. Konovalov, A. I. Sidorov, and I. I. Shaganov, Opt. Zh. No. 1, 43 (1995) [J. Opt. Technol. **62**, 41 (1995)].
[5] A. A. Bugaev, B. P. Zakharchenya, V. V. Shkunov *et al.*, Pis'ma Zh. Tekh. Fiz. **1**, 593 (1975) [Sov. Tech. Phys. Lett. **1**, 267 (1975)].
[6] A. I. Sidorov, Opt. Zh. **64**(1), 25 (1997) [J. Opt. Technol. **64**, 19 (1997)].
[7] B. A. Grigor'ev, *Pulsed Heating by Radiation*, Vol. 2 [in Russian] Nauka, Moscow (1974), 727 pp.

Translated by R. M. Durham

Kinetics of adsorption and recombination of hydrogen atoms at a solid surface

V. F. Kharlamov, K. M. Anufriev, E. P. Krutovskiĭ, Yu. V. Mosin, E. A. Zlotkin, and I. V. Emel'yanov

Orlovo State Technical University
(Submitted June 4, 1997)
Pis'ma Zh. Tekh. Fiz. **24**, 23–27 (March 12, 1998)

A description is given of an experimental apparatus to study fast processes at the interface between solids and gases, which has no counterpart elsewhere. The kinetic adsorption curves of the reactants and the rates of the heterogeneous chemical reaction were both determined for the first time as a result of direct measurements for the recombination of hydrogen atoms. As a result, the dependence of the reaction rate on the concentration of chemisorbed particles revealed that pre-adsorbed particles participate in the reaction. © *1998 American Institute of Physics.* [S1063-7850(98)00503-5]

It is known that observations of the rate of adsorption of gas molecules at the surface of solids can be used to study short-lived pre-adsorption states of molecules (precursor states) and their role in adsorption. Similar data are not available for the time dependence of the rate of heterogeneous chemical reactions accompanied by abrupt changes in the concentration of reactants at moderate and high gas pressures because the necessary technical facilities and methods of investigation are lacking. Consequently, chemical processes involving molecules trapped by a surface from the gas phase in short-lived states have been very little studied.

We developed an experimental apparatus to make relaxation measurements in heterogeneous catalysis by simultaneously determining the kinetic adsorption curves of the reactants and the rate of the heterogeneous chemical reaction. In order to make real-time measurements of the rate of a chemical reaction taking place at the interface between a solid and a gas, we recorded the dynamic effect $F(t) = P_r(t) - P = GJ(t)$ of this reaction, where t is the time, P_r is the gas pressure at the surface of the catalyst, P is the gas pressure at the walls of the vessel, G is a coefficient which depends on the momenta of reactant molecules and reaction products, and J is the rate of this reaction.[1–3] A glass cup containing the sample was suspended by a quartz coil in a continuous-flow reactor. The vertical displacements of the cup were recorded automatically by using a capacitative pickup with a sensitivity of 70 V/mm (using capacitance–frequency–voltage conversion). This pickup consisted of a horizontal metal plate suspended from the cup by long threads and two fixed horizontal capacitor plates (Fig. 1). The detector signal was recorded with an N307 recording millivoltmeter. The sensitivity of this automatic weighing system, calibrated with a 1 mg load, was 4×10^{-8} N with a time constant of 1 s.

The time variation of the dynamic effect of the $H+H\rightarrow H_2$ or $O+O\rightarrow O_2$ reaction was observed experimentally after switching on the atom source, an rf electric discharge in molecular gas. Spectrally pure hydrogen was supplied by diffusion across heated nickel; the oxygen was supplied by thermal dissociation of $KMnO_4$ in vacuum. Gas at 50 Pa pressure was pumped continuously through the vacuum chamber containing the sample. A ZnS–Cu powder phosphor with a specific surface area of 1 $m^2\ g^{-1}$ and highly disperse nickel powder consisting of spherical particles with an average diameter of 10 nm were used. The adsorption of gas at the surface of the sample was monitored using quartz piezoresonance weights with a sensitivity of 10^{-3} monolayers. A piezoelectric transducer with the material being studied deposited on both surfaces was placed alongside the weighing cup containing the same substance. The experiments were carried out with different quantities of material deposited on the piezoelectric transducer, which were determined from the decrease in the natural frequency f ($f=12$ MHz) of the piezoresonance weights ($\Delta f_s = 10-120$ kHz). ''Idle'' experiments ($\Delta t_s = 0$) were also carried out. The frequency f was measured with a ChZ-33 frequency meter.

The samples were preliminarily outgassed in gaseous atomic hydrogen whose concentration was $10^{13}\ cm^{-3}$ near the sample. The temperature of the glass walls of the vacuum chamber containing the sample was held for 5 h at $T=350$ K and the removal of adsorbed contaminants was monitored from the piezoweight readings. The kinetics of the dynamic effect of the reaction and the atomic adsorption kinetics were recorded after a pause in the excitation of the sample by the atomic gas, during which recombination desorption of chemisorbed atoms takes place from the surface.

The profile of the adsorption and desorption curves $f(t)$ does not depend on the quantity of material deposited on the piezoelectric transducer, and the decrease in f as a result of the adsorption of gas is proportional to the quantity of deposited material. The rate of adsorption of H atoms from the atomic–molecular hydrogen mixture is more than two orders of magnitude higher than the rate of adsorption of H_2 molecules under the same conditions. The rate of establishment of adsorption equilibrium after switching on or off the source of H atoms increases with temperature. Hydrogen atoms expel adsorbed H_2 molecules from the surface of the ZnS and Ni crystals after prolonged (hundreds of minutes) exposure of the samples to molecular hydrogen, which leads to a slow

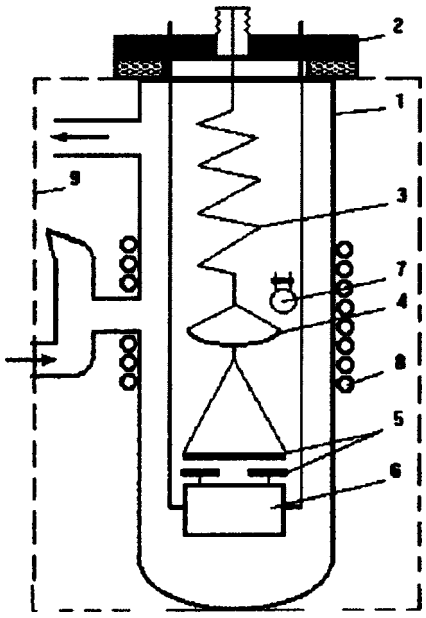

FIG. 1. Schematic of apparatus: *1*—continuous-flow reactor, *2*—vacuum chamber lid with manipulator and electrical leads; *3*—quartz coil, *4*—cup containing sample, *5*—capacitative detector, *6*—oscillator, *7*—piezoelectric transducer, *8*—nichrome coil, and *9*—shield.

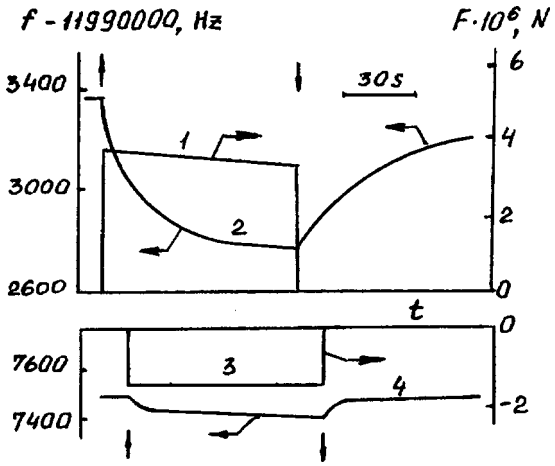

FIG. 2. Time dependence of the dynamic effect of the reaction (*1*, *3*) and of the frequency of the piezoresonance weights (*2*, *4*) after switching on (↑) and switching off (↓) the hydrogen atom source for the adsorption and heterogeneous recombination of H atoms at the surface of nickel before (*1*, *2*) and after (*3*, *4*) its treatment with atomic oxygen: $T=350$ K; $n=10^{13}$ cm^{-3}.

decrease in the quantity of adsorbed hydrogen under the action of the H atoms. The dynamic effect of the reaction increases monotonically as the surface of the samples is purified from adsorbed molecules by the action of H atoms or heating. For the recombination of hydrogen atoms at the surface of ZnS the dynamic effect satisfies $F<0$ which, according to theory,[2,3] corresponds to the desorption of product H_2 molecules at thermal rates. For nickel, on the other hand, we find $F>0$, i.e., the H_2 molecules leaving the surface have an excess kinetic energy of translational motion.

For Ni and ZnS crystals whose surface has been purified of molecules after switching on and off the source of hydrogen atoms, the dynamic effect of the $H+H\rightarrow H_2$ reaction changes abruptly and the kinetic curves of the dynamic effect $F(t)$ are close to rectangular. In this case, the adsorption and desorption of hydrogen atoms takes place slowly and the curves $F(t)$ and $f(t)$ have different profiles. Treatment of nickel with atomic oxygen sharply reduces its adsorption capacity for H atoms and changes the sign of the dynamic effect of the $H+H\rightarrow H_2$ reaction (Fig. 2) which is caused by a decrease in the velocity of desorbed H_2 molecules as a result of a change in their interaction potential with the surface. A comparison of the curves $f(t)$ and $F(t)$ shows that the reaction rate does not increase as the concentration of chemisorbed atoms increases (it does not depend on this concentration or decreases slightly).

When atomic oxygen interacts with ZnS and Ni, the samples reversibly adsorb large quantities ($\Delta f\approx 1$ kHz) of oxygen atoms; the dynamic effect of the $O+O\rightarrow O_2$ reaction is low.

The experimental results for the $H+H\rightarrow H_2$ process may be explained using a reaction model[3,4] in which under these experimental conditions, the reaction channel $HZ+HZ\rightarrow H_2+2Z$ predominates in the heterogeneous recombination of H atoms at the surface of solids, where HZ is a pre-adsorbed atom, Z is an adsorption center, and k_3 is the rate constant of the reaction. The estimated concentration of pre-adsorbed atoms is $N_{p.s.}\approx 10^9$ cm^{-2} and lies outside the limits of sensitivity of the adsorption measurements. According to numerical analyses using the model,[4] the theoretical curves $J(t)$ and $N(t)$, where N is the concentration of chemisorbed atoms, have the same profile as the experimental curves provided that the following conditions are satisfied: $k_1\gg k_5$, $k_3\gg k_4>10^5 k_5$, where k_1, k_4, and k_5 are the rate constants of the reactions $H+Z^{k_1}\rightarrow HZ$, $HZ+(HZ)^{k_4}\rightarrow H_2+2Z$, and $H+Z^{k_5}\rightarrow(HZ)$, where (HZ) is a chemisorbed atom.

To conclude, we have developed an experimental apparatus to study fast processes at the interface between solids and gases, which has no counterpart elsewhere. As a result of direct measurements for the recombination of hydrogen atoms, we have determined for the first time the kinetic adsorption curves of the reactants and the heterogeneous chemical reaction rates. From the dependence of the reaction rate on the concentration of chemisorbed particles we established that pre-adsorbed particles are involved in the reaction.

[1] V. F. Kharlamov, V. N. Lisetskiĭ, and G. G. Savel'ev, Khim. Fiz. **9**, 603 (1990).
[2] V. F. Kharlamov, Poverkhnost' No. 11, 122 (1993).
[3] V. F. Kharlamov, *Recombination of Atoms at the Surface of Solids and Accompanying Effects* [in Russian], Tomsk State University Press, Tomsk (1994), 207 pp.
[4] V. F. Kharlamov, Ukr. Zh. Khim. **71**, 678 (1997).

Translated by R. M. Durham

Study of the formation of contact between rough surfaces based on the particle method

V. E. Rubtsov, S. G. Psakh'e, and A. V. Kolubaev

Institute of Physics of Strength of Materials and Materials Science, Siberian Branch of the Russian Academy of Sciences, Tomsk
(Submitted August 28, 1997)
Pis'ma Zh. Tekh. Fiz. **24**, 28–32 (March 12, 1998)

A model is proposed for the rough surface of a solid based on the particle method. Although the particle size is selected arbitrarily in this study, the evolution of the actual area of contact and the change in stress at the points of contact show fairly good agreement with concepts derived from experimental investigations. The experiments show that as two surfaces converge, the pressure at the contacts is considerably higher than the nominal value, and this leads to plastic deformation of the surface layers much greater than the bulk deformation. The model clearly shows the controlling factors and how the stressed state of the surface layer is formed. The model can be used to analyze interaction between surfaces, not only for the stationary case, but also when these undergo relative displacement.
[S1063-7850(98)00603-X]

When modeling friction and wear processes and also when solving problems of heat and electrical conduction involving contact between rough surfaces, there is a need to determine the real area of contact, the stress distribution, and the structural changes in the surface layers. In addition, for materials which may undergo phase transformations, allowance must be made for changes in the phase composition of the surface layers. It is extremely difficult to realistically estimate contact interaction with allowance for these physicomechanical and chemical properties of rough surfaces using numerical methods of the mechanics of continuous media. One approach to solve these problems may involve using physical concepts developed using the particle method.

In the particle method[1,2] the system being modeled is represented by a set of elements having given properties and interacting according to specific laws. The real structure inside the element is not generally taken into account explicitly, and is incorporated in the model via the laws of interaction and the properties of the elements. Thus, the behavior of a condensed medium is determined by the properties of its constituent elements, the nature of the interaction, and also by the initial and boundary conditions.

In the present study the process of contact formation between two normally converging rough surfaces was modeled using the particle method in a two-dimensional formulation. An investigation was made of the process of contact formation between two surfaces with different degrees of roughness.

In the proposed model, the material was represented by a set of elements of the same species and size. The Lennard–Jones potential was used to describe the interaction between the elements inside the bulk of the material during compression. Under tension it was assumed that the material undergoes elastic–plastic deformation after reaching the yield stress. The interaction between the elements of different surfaces was assumed to be elastic before the yield stress was reached and elastic–plastic beyond the yield stress. The area of contact was taken to be the area of the cross section formed by the geometric intersection of the microirregularity profiles as they approach one another.

The microgeometry of the surface was taken into account as follows:

Each surface element of the contacting layer was made to correspond to an irregularity in the form of a spherical segment (the radius of the segment was assumed to be equal to the radius of curvature of the tips of the irregularities for a given roughness);

The spacing of the microirregularities was defined by the size of the elements;

The undulation was defined by varying the coordinates of the elements of the surface layer (it was assumed to be sinusoidal and characterized by period and height);

The roughness was defined by varying the heights of the irregularities (the coordinates of the corresponding elements in the surface layer) relative to the wave (it was assumed that the heights obey a normal distribution in a certain range Δh and the center of the distribution coincides with the average height of the microirregularities for a given roughness).

The proposed model offers the following possibilities:

1) The surface microrelief can be defined explicitly.

2) Any law of deformation of irregularity under loading can be defined.

3) The number of contacting irregularities, the deformation, and the area of each contact can be determined.

4) The variation in the height distribution of the irregularity tips caused by deformation of the entire surface can be taken into account.

In addition, in the particle method the properties of individual elements can be varied during the modeling process and the influence of possible phase transformations can be investigated.

The system being modeled consisted of a sample and an abradant. The sample was attached to a rigid base and the upper layer of the abradant moved at a constant velocity of

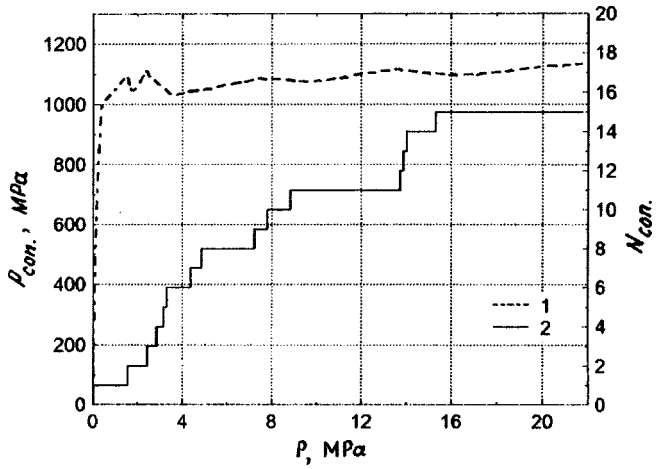

FIG. 1.

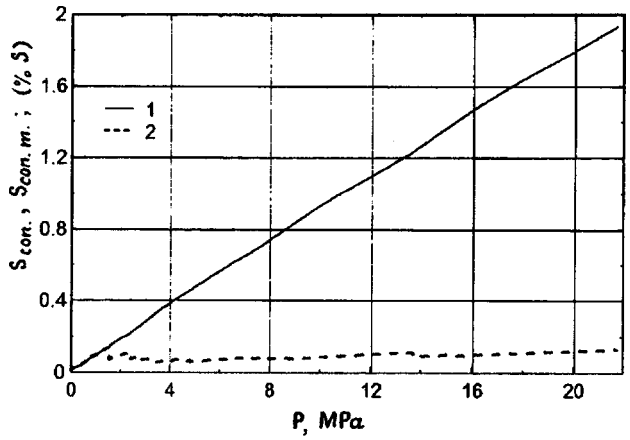

FIG. 2.

10 cm/s. The sides of the sample and the abradant were assumed to be free. The sample contained 100 elements in the surface layer and the abradant contained 72, their sizes being 40 and 55 μm, respectively. The selected parameters of the microgeometry corresponded to polished surfaces.[3,4]

The parameters of the sample material and the abradant were broadly consistent with the characteristics of average-strength structural steel: density 7800 kg/m^3, modulus of elasticity 200 GPa, modulus of elasticity under elastic–plastic deformation 7 GPa, and maximum elastic deformation 0.5%.

As the surfaces converged, the number of contacts was determined and calculations were made of the strain and pressure at the contact points, the actual contact area, and the nominal pressure, which was taken as the ratio of the force of resistance to approach to the total area of the sample (nominal area).[5]

Figure 1 gives the average pressure at the contact points P_{con} (curve *1*) and the number of contacting irregularities N_{con} (curve *2*) as a function of the nominal pressure P. At the initial stage of convergence when only one contact spot has formed, the transition from elastic to elastic–plastic deformation can be clearly seen. The pressure at the single contact increases rapidly and after the transition to elastic–plastic deformation, the pressure increases more slowly. Further convergence leads to an increased number of microcontacts and also causes an increasing number of contacting irregularities to undergo a transition from elastic to elastic–plastic deformation.

As each new irregularity comes into contact, the actual area of contact increases and consequently, pulsations of the average contact pressure are observed for a small number of interacting irregularities. As the number of contacts increases, these pulsations are smoothed and the average pressure at the microcontact remains approximately constant. The real area of contact of the interacting surfaces S_{con} increases linearly with increasing load (Fig. 2, curve *1*), whereas the average area of contact of a single irregularity $S_{\text{con·m}}$ remains almost constant (Fig. 2, curve *2*). Thus, the real area of contact increases mainly as a result of an increase in the number of interacting irregularities.

All these results are quite consistent with current ideas on the mechanics of contact between rough surfaces[3–5] although they were obtained using a fairly simple realization of the particle method which only takes into account the central interaction of the elements. In future work we propose to extend the model to obtain a more adequate description of the plastic deformation process and interaction between surfaces, which can be used to model sliding friction with allowance for adhesion and surface roughness.

[1] R. W Hockney and J. W. Eastwood, *Computer Simulation Using Particles* (McGraw–Hill, New York, 1981; Mir, Moscow, 1987).
[2] D. Potter, *Computational Physics* (Wiley Interscience, New York, 1973; Mir, Moscow, 1975).
[3] I. V. Kraĭgel'skiĭ, M. N. Dobychin, and V. S. Kombalov, *Principles of Friction and Wear Calculations* [in Russian], Mashinostroenie, Moscow (1977).
[4] N. B. Demkin, *Contact Between Rough Surfaces* [in Russian] Nauka, Moscow (1970), 227 pp.
[5] É. D. Braun, N. A. Bushe, I. Ya. Buyanovskiĭ , *Principles of Tribology (Friction, Wear, and Lubrication)*, in *Textbook for Technical Universities*, edited by A. V. Chichinadze [in Russian], published by ''Nauka i Tekhnika'' Center, Moscow (1995), 778 pp.

Translated by R. M. Durham

Equilibrium states of an ion-beam plasma with magnetized electrons at low pressures

S. V. Dudin, A. V. Zykov, A. V. Ushakov, and V. I. Farenik

Kharkov State University; Scientific Physicotechnological Center, Kharkov
(Submitted July 18, 1997)
Pis'ma Zh. Tekh. Fiz. **24**, 33–38 (March 12, 1998)

Results are presented of an experimental investigation of an ion-beam plasma with magnetized electrons in the cathode channel of an ion accelerator with an anode layer. New data are reported on the spatial distributions of the local plasma parameters (plasma potential, electron temperature, electron and ion densities) as functions of the external parameters of the discharge (magnetic field strength, anode voltage, and working gas pressure) in regions with strong, nonuniform electric and magnetic fields. © *1998 American Institute of Physics.* [S1063-7850(98)00703-4]

Earlier studies[1,2] of an ion-beam plasma with magnetized electrons in the conducting cathode channel of an ion accelerator with an anode layer revealed fundamental differences between its properties and those of other active, nonisothermal plasmas—an ion-beam plasma in the absence of electric (**E**) and magnetic (**H**) fields,[3] a positive glow-discharge column at low pressures,[4] and an ion-beam plasma with magnetized electrons in an accelerator with a dielectric exit channel.[5] The main differences are as follows:

1. A nonuniform electric field $E=(1-200)$ V/cm exists in the direction of the ion flux as a result of the strong magnetization of the electrons.

2. A locally equilibrium, near-Maxwellian electron energy distribution function f_e and large electron temperature gradients $dT_e/dz \sim 10$ eV/cm are established, where the z axis is in the direction of the ion beam.

3. For $H > H_{cr} \approx 1$ Oe there is a steady-state electron current to the cathodes, which is not compensated by the ions and is comparable with the discharge current I_p.

However, because of a lack of experimental data on the spatial distribution and dynamics of the local plasma parameters (T_e, the plasma potential φ_{pl}, the electron density n_e, and the ion density n_i) as functions of the discharge conditions (H, I_p, anode voltage U_a, and working gas pressure p), it was impossible to estimate the role of two-dimensional effects and diffusion processes associated with the strong n_e and T_e gradients in the electron current transport to the anode. Thus, the aim of the present study is to measure these dependences and use them as the basis to determine the characteristic states of an ion-beam plasma with magnetized electrons. These data are important for establishing the relationship between the parameters of the ion-beam plasma in the beam transport space and the processes of ion generation in the anode layer and also for developing a self-consistent model of Hall-type ion plasma systems as a whole.

The experimental investigations were carried out using the ''Radikal'' Hall ion source.[1,6] As in Ref. 2, the diagnostic equipment includes a single cylindrical probe, a directional probe, and a multigrid electrostatic analyzer. The parameters T_e and φ_{pl} were determined by double differentiation of the probe current with respect to the probe potential,[7] n_e was calculated from the saturation electron current and T_e, and the ion beam density n_i was determined by measuring the ion current density and the ion energy spectrum.

Data on the evolution of f_e from the ion-beam plasma to the anode layer, and also the dependence of φ_{pl} and T_e on the probe–anode distance z_{pr} for typical operating conditions of the ion source ($p=4\times10^{-4}$ Torr, $H=1.5$ kOe, $U_a=1.5$ kV, and ion beam density $j_i=1$ mA/cm^2) are presented in Ref. 2. Measurements of the local plasma parameters as a function of U_a, H, and p, the results of which are presented here, were made under the same discharge conditions. The working gas was nitrogen.

The experimental measurements required for this problem are complicated by the relative nature of the boundaries of the transition region, which is essentially an ion-beam plasma with magnetized electrons. Another factor is the mobility of the boundaries both in the direction of the ion beam transport space and in the direction of the anode layer with varying U_a, H, and p. For example, Fig. 1 gives the electron and ion densities as a function of the magnetic field for a fixed position of the probe $z_{pr}=7$ mm. Also plotted for comparison are the electron density $n_{al}=1/4\pi mc^2 \nu_i/\nu_0 H^2$ in the anode layer and the layer thickness $l_{al}=\sqrt{2mc^2/e\nu_0/\nu_i U_a}\times 1/H$ calculated using the Zharinov–Kervalishvili model,[8] where ν_i is the frequency of ionization by electrons and ν_0 is the frequency of elastic electron–atom collisions. It can be seen from these curves that for small H the thickness of the anode layer is of the order of the probe–anode distance, while the electron density n_e is of the same order as n_{al} and two or three times higher than n_i. As H increases, the thickness of the anode layer decreases, the difference between n_e and n_i decreases, and for $H \geqslant 1.5$ kOe the electron and ion densities are comparable. Note that according to earlier measurements,[2] at the boundary of the anode layer f_e has a Maxwellian core, the electron temperature is $T_e \approx 10-12$ eV, and the plasma potential φ_{pl} may reach 60–100 V.

Using these data, the results of measurements of φ_{pl}, $T_e=f(H,U_a,p,z)$ were generalized on a diagram showing the equilibrium states of an anisotropic plasma with intensive ionization (Fig. 2). The diagram is based on the dependence

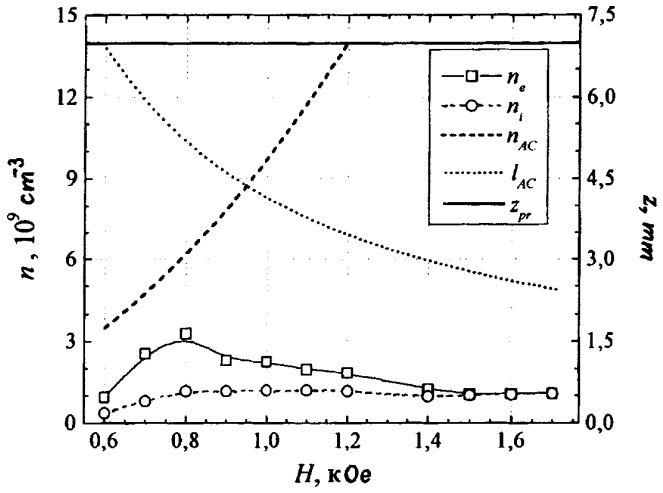

FIG. 1. Experimental values of the electron density n_e and ion density n_i as functions of the magnetic field H for $z_{pr}=7$ mm, $U_a=1.5$ kV, and $p=4\times10^{-4}$ Torr, along with the electron density N_{al} in the anode layer and thickness l_{al} of the anode layer as given by the Zharinov–Kervalishvili model.[8]

$\varphi_{pl}=f(T_e)$, calculated from the continuity equation $dj_x/dx+dj_z/dz=\nu_i n_e+\nu_{ii}n_i$, where ν_{ii} is the frequency of ionization by the ion beam, j_z and j_x are the densities of the currents to the anode and the cathode, respectively ($\mathbf{x}\|\mathbf{H}$, $\mathbf{z}\|\mathbf{E}$). It assumes a Maxwellian function f_e and a linear approximation of the ionization cross section, when $j_x=en_e\sqrt{T_e/2\pi m_e}\exp\{-e\varphi_{pl}/T_e\}$ and $\nu_i=4C_i\times\sqrt{(T_e/2\pi m_e)}n_a(I+2T_e)\exp\{-I/T_e\}$, where I is the ionization potential, n_a is the atomic density, and C_i is a constant which depends on the type of working gas and has dimensions of electron volts per square centimeter (Ref. 9). Assuming that the wall layer is thin compared with the thickness d of the cathode channel, in the absence of ionization amplification of the electron current in the direction of the electric field ($dj_z/dz=0$) and neglecting ionization by the beam ($\nu_{ii}=0$), we readily obtain the relation $e\varphi_{pl}=I+\alpha T_e$, where $\alpha\approx-\ln[0.42pd(I+2T_e)]$ for nitrogen. The dependence $\alpha=f(p)$ for $T_e=1$, 10, and 25 eV is plotted in Fig. 2a (curves *1*, *2*, and *3*, respectively) while Fig. 2b gives $\varphi_{pl}=f(T_e)$ for $p=4\times10^{-4}$ Torr (curve *1*). Also plotted are the experimental data $\varphi_{pl}=f(T_e)$ for the same pressure p for various dependences: curve *2*—for the spatial distributions φ_{pl}, $T_e=f(z)$ for $H=1.5$ kOe, $U_a=1.5$ kV; curve *3*—for φ_{pl}, $T_e=f(H)$ for $z_{pr}=7$ mm, $U_a=1.5$ kV; region *4*—for φ_{pl}, $T_e=f(U_a)$ for $z_{pr}=7$ mm and $H=1.5$ kOe. The right-hand axis in Fig. 2b gives the nonlinear scales which display the correspondence between the experimental points $\varphi_{pl}=f(T)_e$ and the parameters H and z.

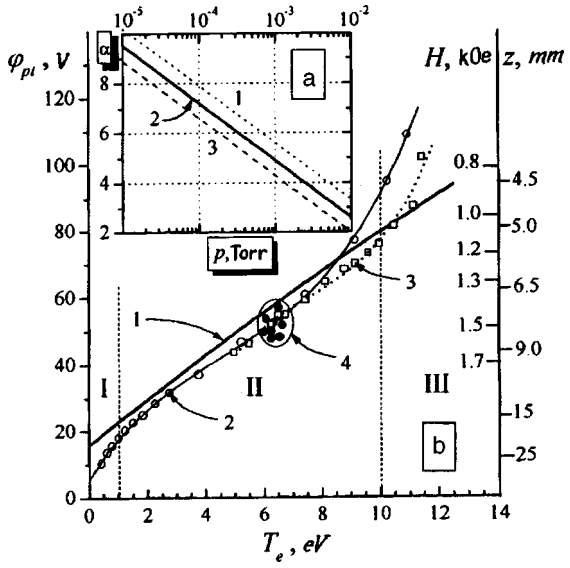

FIG. 2. a—Coefficient of proportionality α between the plasma potential φ_{pl} and the electron temperature T_e as a function of the pressure p for various T_e: *1*—$T_e=1$ eV, *2*—$T_e=10$ eV, *3*—$T_e=25$ eV; b—plasma potential versus electron temperature for $p=4\times10^{-4}$ Torr; *1*—using the ionization equilibrium model; curve *2*—for the spatial distributions φ_{pl}, $T_e=f(z)$ at $H=1.5$ kOe, $U_a=1.5$ kV; curve *3*—for φ_{pl}, $T_e=f(H)$ at $z_{pr}=7$ mm, $U_a=1.5$ kV; region *4*—for φ_{pl}, $T_e=f(U_a)$ at $z_{pr}=7$ mm and $H=1.5$ kOe.

As a result of analyzing this diagram, we can identify the following characteristic ionization equilibrium states in an ion-beam plasma with magnetized electrons:

I. $T_e<1$ eV—the experimental points $\varphi_{pl}=f(T_e)$ lie substantially ($\sim50\%$) lower than the equilibrium line, which corresponds to the beam ions contributing appreciably to the ionization.

II. $T_e=1-10$ eV—the experimental points coincide with the equilibrium state ($dj_z/dz=0$) to within 10%, when the product electrons mainly drift to the cathode.

III. $T_e>10$ eV—the experimental points lie above the equilibrium line, which corresponds to the onset of ionization amplification of the electron flux to the anode ($dj_z/dz>0$).

It can be seen from the state diagram that regions I, II, and III systematically alternate with decreasing H and z. A decrease in U_a and p causes a negligible ($\sim10-20\%$) increase in φ_{pl} and T_e for constant H and z.

To conclude, the experimental data and a theoretical analysis of the ionization amplification of the electron current indicate that in the ion-beam plasma–anode layer transition region in Hall systems at low pressures and strong magnetic fields, conditions are established where the electron pressure gradient impedes the evolution of electron avalanches and causes the newly formed electrons to drift to the cathodes. The determining factor for the existence of this region is the formation of a locally equilibrium function f_e, where the high-voltage boundary is defined by the condition $T_{al}<(2-3)I$ and the boundary value of the potential $\varphi_{al}=I+\alpha T_{al}\sim100$ V increases with decreasing pressure, i.e., a considerable fraction of the applied potential difference falls within the transition region.

In addition, estimates have shown that at pressures $p>10^{-5}$ Torr at the high-voltage boundary of an ion-beam plasma with magnetized electrons, the frequency of Maxwellizing electron–electron collisions is $\nu_{ee}\ll\nu_i$, i.e., a Langmuir paradox is found as in the positive column of a low-pressure glow discharge.[4] The evolution of small-amplitude diocotron oscillations in the anode layer observed in systems with $H>1$ kOe, may well be a factor responsible for the significant expansion of the transition region in the direction of large φ_{pl} and T_e.

[1] S. V. Dudin, A. V. Zykov, and A. V. Ushakov, Pis'ma Zh. Tekh. Fiz. **21**(2), 25 (1995) [Tech. Phys. Lett. **21**, 54 (1995)].
[2] S. V. Dudin, A. V. Zykov, A. V. Ushakov, and V. I. Farenik, Pis'ma Zh. Tekh. Fiz. **22**(23), 43 (1996) [Tech. Phys. Lett. **22**, 969 (1996)].
[3] S. V. Dudin, A. V. Zykov, and V. I. Farenik, Pis'ma Zh. Tekh. Fiz. **17**(6), 22 (1991) [Sov. Tech. Phys. Lett. **17**, 431 (1991)].
[4] V. L. Granovskiĭ, *Electric Current in Gas* [in Russian] Nauka, Moscow (1971), 544 pp.
[5] Yu. V. Sanochkin and V. L. Kalashnikov, Zh. Tekh. Fiz. **44**, 2512 (1974) [Sov. Phys. Tech. Phys. **19**, 1554 (1974)].
[6] Yu. P. Maishev, Élektron. Promysh. No. 5, 15 (1990).
[7] S. V. Dudin, Prib. Tekh. Éksp. **4**, 78 (1994).
[8] N. A. Kervalishvili and A. V. Zharinov, Zh. Tekh. Fiz. **35**, 2194 (1965) [Sov. Phys. Tech. Phys. **10**, 1682 (1965)].
[9] Yu. P. Raĭzer, *Gas Discharge Physics* [Springer, New York (1991); Nauka, Moscow (1987), 592 pp.].

Translated by R. M. Durham

Laser autodyne interferometry of the dynamic parameters of biological specimens

D. A. Usanov, Al. V. Skripal', A. Yu. Varagin, An. V. Skripal', V. V. Potapov, T. T. Shmakova, and S. S. Mosiyash

N. G. Chernyshevskiĭ State University, Saratov

(Submitted September 4, 1997)
Pis'ma Zh. Tekh. Fiz. **24**, 39–43 (March 12, 1998)

A method based on the use of autodyne detection effects in a semiconductor laser is proposed to analyze the dynamic state of biological specimens. The advantages of this method compared with conventional photoelectric methods are demonstrated. Results are presented of the use of the proposed method to investigate the heart beat frequency and amplitude of Daphnia as a function of the degree of toxicity of the aqueous medium. © *1998 American Institute of Physics.* [S1063-7850(98)00803-9]

Methods based on estimates of the physiological parameters of biological test specimens are widely used to assess the degree of environmental contamination. Daphnia freshwater crayfish (*Daphnia magna Straus*) are used as test specimens to monitor the state of water. It was shown in Refs. 1 and 2 that the heartbeat rate of Daphnia depends strongly on the concentration of hydroquinone in the water and that the phenol concentration influences the respiration rate. However, since the photoelectric methods used in these studies possessed low sensitivity and could not be used to record the radiation transmitted by a biological specimen, it was impossible to make elaborate investigations of the changes in the physiological parameters of the specimens.

In order to increase the number of informative parameters characterizing the behavior of Daphnia in a toxic medium, we developed a method using an autodyne detection effect in a semiconductor laser.

The method of recording the dynamic state of the specimens is based on the principle of forming an external autodetection signal by returning some of the radiation reflected by the monitored object to the cavity of a semiconductor laser.[3,4] The method was implemented using the apparatus shown schematically in Fig. 1. Radiation from a semiconductor laser *7* (ILPN-206), stabilized by a current source *8*, was focused by a lens *6* into the heart region of Daphnia *4* which was inserted in a channel *3* on a transparent stage *5*. A night viewing device *1* was used to observe the infrared semiconductor laser radiation and its focusing into the heart region. Some of the radiation reflected by the Daphnia heart was returned to the semiconductor laser cavity, where the change in its output power was recorded by a photodetector *9*. The photodetector signal was passed via an amplifier *10* and an analog-to-digital converter *11* to a computer *12*. The Daphnia heart rate was determined after calculating the spectrum of the detected signal using a fast Fourier transformation.

Daphnia freshwater crayfish (*Daphnia magna Straus*) were bred under standard laboratory conditions. For the ex-

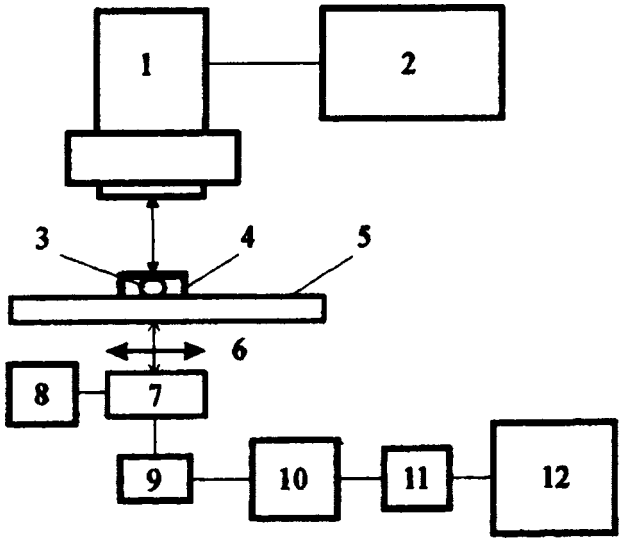

FIG. 1. Schematic of apparatus to measure Daphnia heart rate.

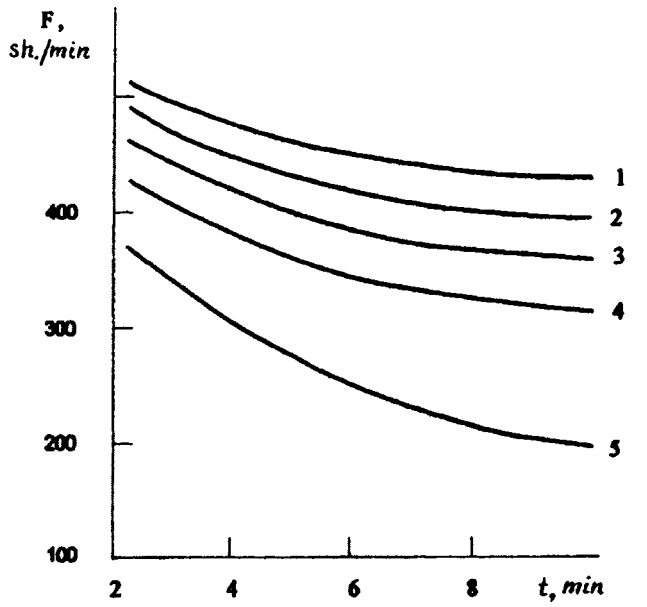

FIG. 2. Daphnia heart rate F versus time of exposure to water containing various concentrations of phenol: *1*—control batch, *2*—1.2 mg/liter, *3*—2.5 mg/liter, *4*—5 mg/liter, and *5*—10 mg/liter.

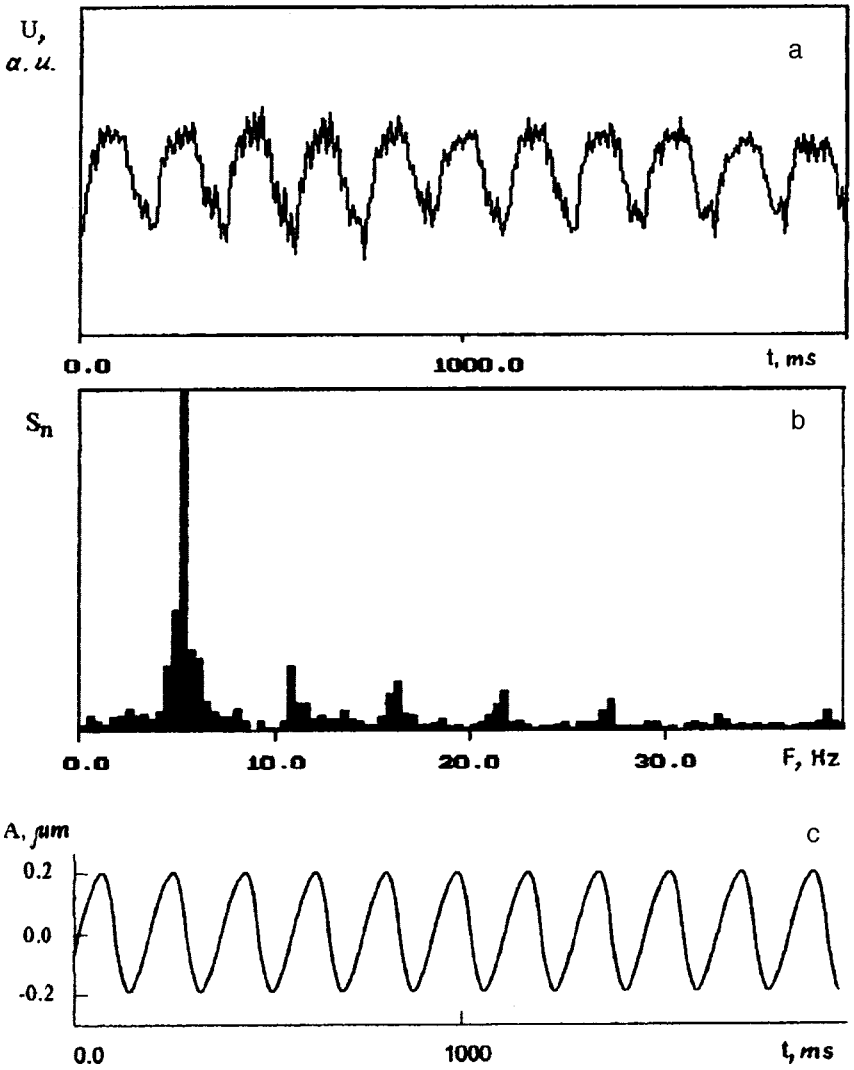

FIG. 3. Results of measurements and analysis of the detected signal: a—instantaneous values of the normalized detected signal U versus time t for a phenol concentration of 5 mg/liter in the water; b—spectrum of detected signal normalized to the amplitude S_n of the largest harmonic. The heart rate is 375 beats/min; c—instantaneous values of the displacement of the Daphnia heart A versus time t when the phenol concentration in the water is 5 mg/liter.

periments we used specimens between one and three days old, measuring 0.7–1.5 mm. An aqueous solution of phenol with concentrations between 0.3 and 10 mg/liter was used as the toxic factor. The water in which the Daphnia were raised was used for control measurements. A single crayfish from the aquarium was placed in a chamber which contained the toxic solution and restricted the movement of the crayfish. The chamber was attached to a microscope stage. The optical system was directed toward the heart and the apparatus tuned to the maximum signal.

The results of measurements of the Daphnia heart rate for various concentrations of phenol dissolved in the water are plotted in Fig. 2. The results show that the Daphnia heart rate varies negligibly in the control measurements and stabilizes after adaptation for 5 min. A decrease in the Daphnia heart rate was recorded for phenol concentrations exceeding 1.2 mg/liter. The largest reduction in the heart rate was observed for phenol concentrations of $\sim$10 mg/liter. In this case, the heart rate was 200 beats per minute at the end of the exposure period.

Other parameters which can be recorded using this laser autodyne system are the amplitude and profile of the detected signal. Figure 3a gives the instantaneous values of the detected signal as a function of time when phenol is present in the water. Figure 3b gives the results of calculations of the detected signal spectrum. The Daphnia heart rate was determined from the harmonic having the largest amplitude in a given range of variation of the vibration frequency of the biological specimen and the amplitude of the oscillations was determined from the set of spectral harmonics.[5,6] Figure 3c gives the time dependence of the instantaneous values of the displacement of the Daphnia heart, calculated using the results of the measurements. It can be seen that when phenol was present in the water, the amplitude of the Daphnia heart beats was 0.2 μm, which is substantially smaller than that in the absence of phenol (0.4 μm).

To sum up, we have shown that a method based on an autodyne detection effect in a semiconductor laser is promising for analyses of the dynamic state of biological specimens.

[1] G. S. Kiknadze, B. P. Esakov, S. B. Kuz'minykh, and V. M. Komarov, *Experiment to Estimate the Degree of Contamination of an Aqueous Medium from Changes in the Heart Rate of Daphhnia* [in Russian], published by Scientific Center of Biological Research, Academy of Sciences of the USSR, Pushchine, 1983, 13 pp.

[2] B. I. Kolupaev, *Methods for Biological Testing of Water*, edited by A. I. Kraĭnyukovoĭ [in Russian], Chernogolovka (1988), 103 pp.
[3] H. Olesen, J. H. Osmundsen, and B. Tromborg, IEEE J. Quantum Electron. **22**, 762 (1986).
[4] E. M. Gershenzon, B. N. Tumanov, and B. I. Levit, Izv. Vyssh. Uchebn. Zaved. Radiofiz. **23**(5), 535 (1980).
[5] D. A. Usanov, A. V. Skripal', V. A. Vagarin, and M. R. Vasil'ev, Zarubezh. Radioélektron. No. 6, 43 (1995).
[6] D. A. Usanov, A. V. Skripal', and V. A. Vagarin, Prib. Tekh. Éksp. **6**, 162 (1994).

Translated by R. M. Durham

Determination of the uniformity of the carrier lifetime in a material from the profile of the amplitude spectrum of an ion detector

N. B. Strokan

A.F. Ioffe Physicotechnical Institute, Russian Academy of Sciences, St. Petersburg
(Submitted October 22, 1997)
Pis'ma Zh. Tekh. Fiz. **24**, 44–50 (March 12, 1998)

An analysis is made of charge transport in the neutral base of a p^+-n structure as a result of its diffusion to the boundary of the p-n junction under conditions where nonequilibrium carriers are generated by single α-particles. It is assumed that nonuniformity of the carrier lifetime (τ), described by a Gaussian distribution, exists over the area of the structure. The profile of the transported charge spectrum is calculated for these conditions and its correlation with the measure of nonuniformity τ is obtained. Since the tracks of the diffusing α-particles occupy an extremely small volume, recording them is equivalent to local probing of the material for τ. It is suggested that the calculated function should be used as a calibration function to determine the spread of τ values in materials. The method is tested on Si for a surface-barrier structure by recording 8.78 MeV α-particles. © *1998 American Institute of Physics.*
[S1063-7850(98)00903-3]

It is known that semiconductor detectors use an ''ionization'' principle to record hard radiation. By analogy with a gas-filled ionization chamber, the working zone of the detector is a region of electric field in which nonequilibrium electron–hole pairs separate and drift to the electrodes of a capacitor equivalent in the detector configuration. In practice, this is achieved in the structure of a reverse-biased p^+-n junction.

Here we show that by using diffusive carrier transport, which is uncharacteristic of a detector, it is possible to determine the nonuniformity of parameters such as the carrier lifetime over the area of the p^+-n structure. This nonuniformity is determined from the width of the spectrum of signal amplitudes obtained using a standard spectroscopic apparatus.

It has already been established[1,2] that the width δ of the amplitude spectrum (at half-maximum) is extremely sensitive to the trapping of nonequilibrium charge. In this case, δ is a linear function of the charge loss at the signal formation stage. The coefficient of proportionality of this dependence is determined by the nonuniformity of the carrier transport in the detector structure.

In Ref. 1 this was demonstrated for the case of carrier trapping. The implication is that a carrier is confined by some trapping center for a time exceeding that required by the electronics to form the signal (usually of the order of microseconds). Ultimately, as the carrier drifts, it only passes through part of the gap of the equivalent capacitor, which leads to an amplitude deficit. In Ref. 2 an analysis was made of another type of trapping, direct recombination of carriers generated in a dense ion track after the comparatively short stage in which the field responsible for the drift is screened. In this case, the electron–hole pair is completely excluded from the formation of the signal amplitude.

The task is to determine how the spectral line profile and its width depend on the charge losses accompanying diffusion transport when the main loss channel is recombination of minority carriers. In our opinion, the results appear to be a useful method of analyzing the inhomogeneity of a material. Thus, irradiation by 8.78 MeV monochromatic α-particles which is standard for detector practice is considered (in Si the range is 56.5 μm and in GaAs it is 39 μm). The radiation intensity is low so that single particles are recorded.

1. The amplitude spectrum of the transported charge q is constructed by the following steps. First, dN/dq is formed, where dN is the number of cases (pulses) in the amplitude interval dq. It is assumed that the nature of the spectrum (the spread of q values) is caused by fluctuations of the nonequilibrium carrier lifetime τ. The α-particle tracks are dense bunches of electron–hole pairs whose diameters are only of the order of tens of micron. Thus, when each particle is recorded, the transport conditions show up in the microscopic volume. As a result of the random incidence of particles on the detector, the statistics of the lifetime τ over the area of the sample appears as the parameter most sensitive to structural defects. Then, we can write $dN/dq=(dN/d\tau)\times(d\tau/dq)$ and the question arises as to the form of the τ distribution and the function $q=f(\tau)$ under carrier diffusion conditions.

Let us take the distribution of τ to be Gaussian. A Gaussian distribution is most likely when the deviations of the value from the mean are smaller than the mean: $dN/dq=(dN/d\tau)(d\tau/dq)$. Thus, we take

$$dN/d\tau=\frac{\exp[-(\tau-\tau_0)^2/2\sigma^2]}{\sqrt{2\pi}\sigma}. \tag{1}$$

The correlation between q and τ for charge generation with the profile typical of α-particles (the Bragg curve) and subsequent diffusion to the boundary of the p^+-n junction was examined in Ref. 3. It was assumed that the end point a

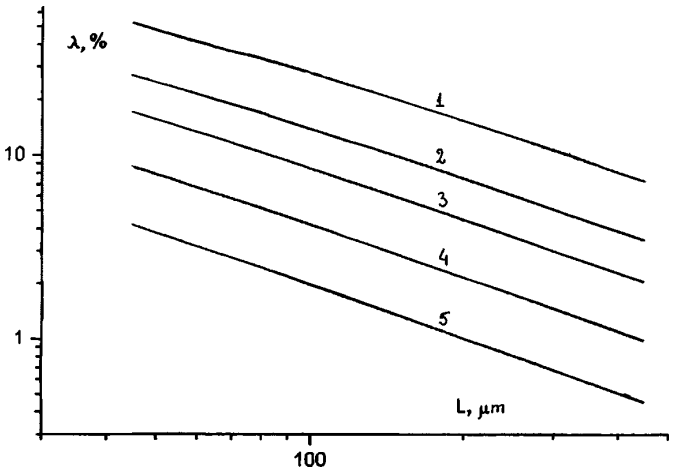

FIG. 1. Losses caused by recombination of electron–hole pairs in α particle track versus diffusive displacement length. A 56 μm particle track protrudes into the region of diffusive transport by the length a, μm; *1*—56, *2*—36, *3*—26, *4*—16, and *5*—10.

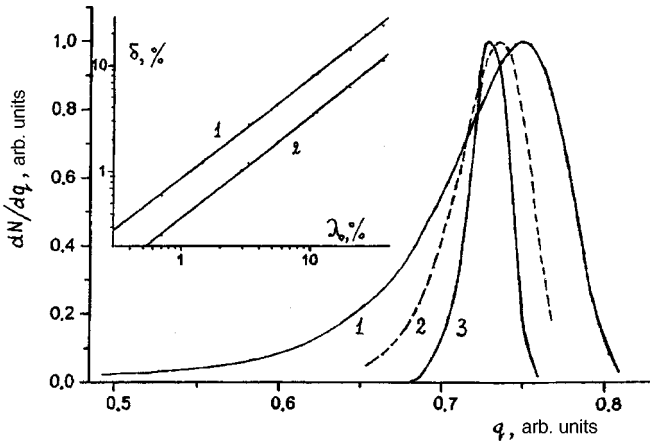

FIG. 2. Amplitude spectra for various nonuniformities of the carrier lifetime $\Delta\tau/\tau_0$ (calculated). Diffusion conditions: $L_0=100$ μm, $a=56$ μm. Values of $\Delta\tau/\tau_0$, %: *1*—100, *2*—50, *3*—25. Inset—spectral line width versus average carrier losses. Width taken at 0.1 (*1*) and 0.5 (*2*) of maximum.

of a particle track of length R can only be situated in the region of diffusion transport. The charge deficit $\lambda=1-q$ as a function of a' was calculated for various values of the diffusive displacement length $L=(D\tau)^{1/2}$, where D is the diffusion coefficient. These data are plotted in Fig. 1 on the required scale $\lambda=f(L)$ for various values of a. The dependence $\lambda(L)$ was conveniently approximated in the form

$$\lambda=A_0+A_1/L+A_2/L^2, \tag{2}$$

where A_0 is cubic and A_1 and A_2 are quadratic parabolas relative to a. Then, for the required spectrum $dN/dq=f(q)$, neglecting the numerical factors, we obtain a system of two equations:

$$dN/dq=(L/L_0)^2 \times\frac{\exp\{-[(L/L_0)^2-1]^2/0.362(\Delta\tau/\tau_0)^2\}}{(A_1/L+2A_2/L^2)}, \tag{3}$$

$$q=1-(A_0+A_1/L+A_2/L^2).$$

Here, by analogy with δ, the width of the spectrum of τ values is introduced as $\Delta\tau=2.35\sigma$. The system (3) can be used to construct the spectra of signal amplitudes for various average values of $L_0=(D\tau_0)^{1/2}$, $\Delta\tau/\tau_0$, and the parameter a.

Figure 2 shows the amplitude spectra for the case where a corresponds to the particle range, i.e., $a=R=56$ μm. Despite the value $L_0=100$ μm (almost twice a), an average charge deficit of the order of 25% is observed. As the lifetime becomes more variable, the profiles of the spectra acquire a characteristic asymmetry. An extended section with small amplitudes appears on the left wing. If the relative nonuniformity reaches 100% ($\Delta\tau/\tau_0=1$), up to 50% losses of charge may occur.

The width of the spectrum at half-maximum and also at one-tenth maximum ($\delta_{0.1}$) where the asymmetry is strongest, is taken as a quantitative measure. The behavior of δ and $\delta_{0.1}$ as a function of the average charge losses λ_0 is shown in the inset to Fig. 2 for the case $\Delta\tau/\tau_0=1$. The points give the calculated values, which include three values of L_0 (45, 100, and 200 μm), with the parameter a varied in each case (values of 10, 20, 30, and 45 μm were taken). The inset shows that if the nonuniformity of τ is fixed, both values for the spectral width δ and $\delta_{0.1}$ are uniquely determined by the charge losses. In other words, the specific values of L_0 and a responsible for the losses λ_0 are unimportant for the spectral profile.

An extremely important factor is that the functions $\delta(\lambda_0)$ for various $\Delta\tau/\tau_0$ are linear, with the slope $K=\Delta\delta/\Delta\lambda_0$ which depends on the nonuniformity factor. These observations can be used to obtain the function $K=f(\Delta\tau/\tau_0)$ which is the calibration function to determine the uniformity of the carrier lifetime in the material (Fig. 3). Note that for large $\Delta\tau/\tau_0$ the function K is less gently sloping than that obtained in Ref. 2, also for carrier recombina-

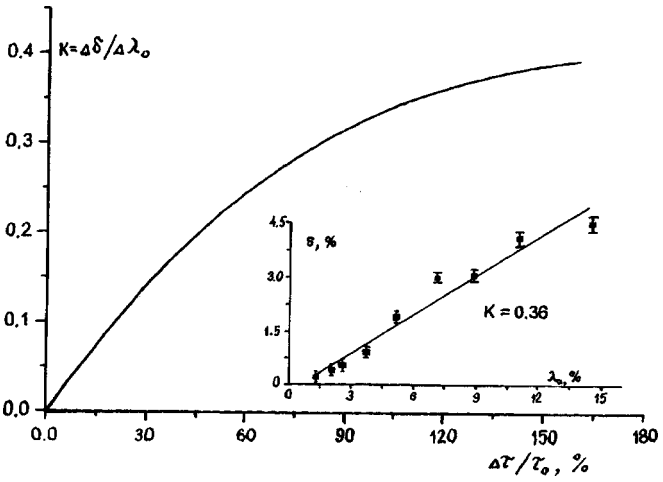

FIG. 3. Calculated function to determine the carrier lifetime nonuniformity. The growth rate of the line width as a function of the relative carrier losses is plotted on the ordinate (see inset to Fig. 2). Inset—dependence of line width on carrier losses observed experimentally for Si surface-barrier structure. Single 8.78 MeV α-particles are detected; the losses are created by a difference in the energy released in the diffusive transport region.

tion. This difference can be attributed to the different dependence $q(\tau)$, which is determined by diffusion rather than by drift transport of carriers, as in Ref. 2.

2. An experiment was carried out using the surface-barrier structure of an Si detector. The apparatus was standard for recording amplitude spectra, and incorporated a preamplifier, an amplifier with a pass band formed by *RC* differentiation–integration circuits, and an amplitude analyzer. A reverse bias was initially applied to the structure so that the space charge region (strong electric field) completely covered the track. Under conditions of ''fast'' carrier drift the signal was taken to be unity. The voltage was then reduced and values at which some of the track extended outside the field region were used. In this case, the average amplitude of the signal decreased as a result of carrier recombination accompanying the relatively slow diffusive transport. At the same time, the profile of the amplitude spectrum became asymmetric in agreement with the calculated data plotted in Fig. 2.

The inset to Fig. 3 shows the behavior of the spectral line width δ as a function of the losses λ_0. As was to be expected, the dependence is linear with the slope (i.e., the value of the function *K*) $\Delta\delta/\Delta\lambda_0 = 0.36$. In accordance with Fig. 3, this value corresponds to substantial nonuniformity $\Delta\tau/\tau_0 = 120\%$.

3. In conclusion we note some practical aspects. We emphasize that this method does not require a p^+-n structure with a high-quality return branch, since the line width is usually appreciable and the return current noise makes a small contribution against this background. For example, a surface barrier is quite sufficient, i.e., the material does not require heat treatment. It is also possible to use particles of different energy, when the charge losses will vary as a result of differences in the ranges. In this modification, a single (and also low) bias voltage may be used.

The resistivity range for this variation in the losses as a result of a reverse bias applied to Si is three orders of magnitude (between a few $\Omega\cdot$cm and a few k$\Omega\cdot$m). In the variant with particles of different energy, the resistivity has no lower limit.

In Ref. 3 it was shown that the carrier lifetime can be determined from the signal deficit. Note that the integrated nature of the method (the charge is measured) means that short, nanosecond, times τ can also be determined. In this connection, the results obtained above combined with the data from Ref. 3 give a complete picture of the recombination properties of a material: the values of τ and also their statistics over the sample area. Another important factor is that the values of τ for dense α-particle tracks correspond to a high level of injection, i.e., are related to the concentration of recombination centers by a simple (inversely proportional) dependence.

[1] L. L. Makovsky, N. B. Strokan, and N. I. Tisnek, IEEE Trans. Nucl. Sci. **5**, 304 (1968)
[2] E. M. Verbitskaya, V. K. Eremin, A. M. Malyarenko, N. B. Strokan, and V. L. Sukhanov, Fiz. Tekh. Poluprovodn. **21**, 1883 (1987) [Sov. Phys. Semicond. **21**, 1140 (1987)].
[3] I. N. Il'yashenko and N. B. Strokan, Fiz. Tekh. Poluprovodn. **30**, 302 (1996) [Semiconductors **30**, 167 (1996)].

Translated by R. M. Durham

Influence of feedback on the complex dynamics of an electron beam with a virtual cathode in a virtode

A. E. Khramov

''Kolledzh'' State Educational-Scientific Center, Saratov State University
(Submitted October 17, 1997)
Pis'ma Zh. Tekh. Fiz. **24**, 51–57 (March 12, 1998)

Results are presented of a numerical simulation of the nonlinear dynamics of a relativistic electron beam with a virtual cathode in a drift relativistic-electron-beam vircator system with and without external feedback. © *1998 American Institute of Physics.* [S1063-7850(98)01003-9]

As a result of the development of efficient sources of high-current relativistic electron beams (REBs) with currents exceeding 10–100 kA and acceleration energies of 0.1–10 MeV, the power of almost all classical microwave devices has increased sharply. However, the success achieved in acceleration technology cannot be fully utilized in these devices because the beam current is limited. As the current approaches a certain level, the efficiency of the interaction between the electrons and the electromagnetic fields deteriorates. Supercritical-current generators, or vircators,[1] do not have this shortcoming. They use the oscillations of a so-called virtual cathode, a region in the interaction space whose potential is close to that of the cathode, for phase selection of the electrons. At present, the use of vircators to generate superpower microwave radiation pulses must be considered its most important application. However, it has been shown that virtual-cathode devices may be controlled by an external microwave signal, allowing them to be used as modules of phased-array antennas.

Here, results are reported of investigations of the nonlinear dynamics of an electron beam with a virtual cathode in a drift REB vircator system with and without external feedback delay.

The system studied is a section of a cylindrical waveguide closed on both sides by conducting walls. A single-velocity electron beam is injected into the system. A characteristic feature of the system is the external feedback, which was achieved by kinematic modulation of the electrons entering the drift space by an electromagnetic signal derived from the interaction space and influencing the flux with a delay τ.

A description of the nonlinear and nonsteady-state processes in this system was constructed using a self-consistent system of Maxwell equations and the Vlasov transport equation, which was solved numerically using a conservative difference scheme.[2,3] The main parameters on which the behavior of this system depends are the ratio of the beam current to the critical vacuum current, denoted by α, and the feedback parameters: the delay time τ and the coordinate of the point from which the feedback signal is taken.

It is well known from both numerical simulations and experiments that an electron beam with a virtual cathode exhibits complex irregular dynamics. In Ref. 4 an electrostatic model was used to show that an electron beam with a virtual cathode in a Pierce diode may demonstrate different types of behavior, including dynamic chaos. In the present study, the investigations were carried out using a vircator model which allows for nonpotential effects which limit the propagation velocity of the electromagnetic waves in the system.[5]

Figures 1a–1c give the power spectra, attractor projections, and time series of the beam current from the region of formation of the virtual cathode for various values of α. Note that the time series was taken after the transition process had damped away.

For low supercriticality α ($\alpha<2$) periodic relaxation oscillations are established in the system (Fig. 1a, $\alpha=1.5$). The power spectrum contains narrow peaks which are multiple harmonics of the fundamental frequency $\omega_0 \approx 2\omega_p$, where $\omega_0=2\pi/T_0$ (T_0 is the characteristic scale of the oscillations which corresponds to the total transit time of the electrons reflected by the virtual cathode) and ω_p is the plasma frequency of the electron beam. The attractor projection corresponds to a single-stage limit cycle. As the parameter α increases ($2<\alpha<5$), the periodic oscillations disappear (Fig. 1b, $\alpha=3.7$). The spectrum contains a noise pedestal on which are superposed a well-defined fundamental-frequency peak and peaks of its harmonics which merge into the noise pedestal as α increases. It can be seen from the phase portrait that a chaotic attractor appears at the base of a single unstable limit cycle which corresponds to an attractive limit set for the periodic motion. In addition to the chaotic behavior of the amplitude, the time series reveals random phase shifts of the oscillations. This behavior suggests that in this range of variation of α, a rotational fporm of chaos is present in the system whose image in phase space is an inhomogeneous attractor. For $\alpha>5$ (Fig. 1c), the spectrum is extremely noisy. No clearly defined peaks can be identified, and the structure of the attractor is fairly complex, consisting of a set of unstable periodic orbits.

All these observations suggest that the system formed by an electron beam with a virtual cathode and an electromagnetic field exhibits complex nonlinear dynamics. To refine the characteristics of the complex behavior of the system, the fractal dimension of the reconstructed attractor is now determined. Figures 2a–2c give the slope of the correlation

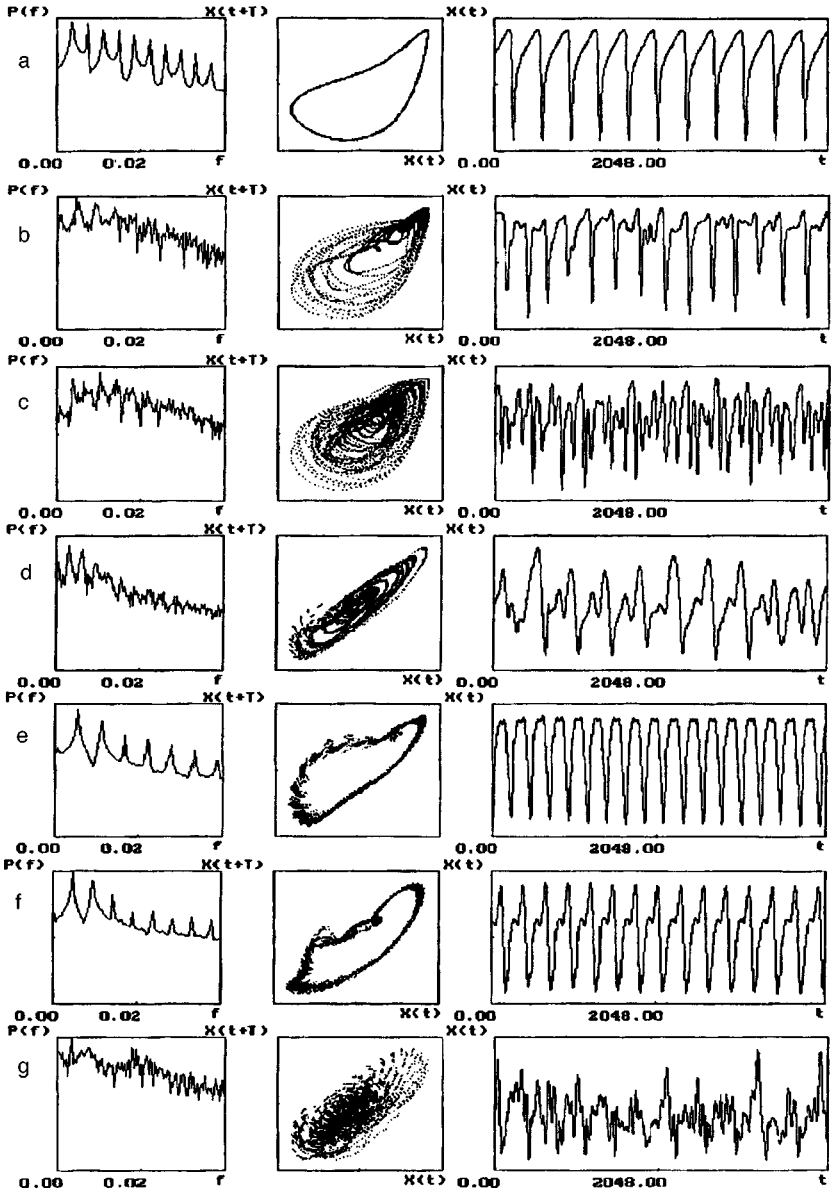

FIG. 1. Phase portraits, power spectra, and time series of current oscillations for various values of the parameters.

integral[6,7] as a function of ϵ in a log–log plot for various values of the embedding space dimension m.

For $\alpha<2$ (Fig. 2a, $\alpha=1.5$), the dimension of the limit set is an integer, which corresponds to a regular manifold. As the supercriticality increases, the dimension becomes a fraction. For $2<\alpha<5$ (Fig. 2b, $\alpha=3.7$) the dimension of the limit set saturates with an embedding space dimension of four. The correlation dimension of the attractor D_e increases monotonically with increasing α. The saturation of the attractor dimension for $m<5$ suggests that the system formed by a virtual-cathode electron beam and an electromagnetic field possesses 1.5–2 degrees of freedom. The nature of the spectrum, and the fact that the fractal dimension is finite and fractional confirm that when the beam current exceeds the critical vacuum current in the range $2<\alpha<5$, dynamic chaos is established in the vircator. For the supercriticality $\alpha>5$ (Fig. 2c, $\alpha=12$), it can be seen that the attractor dimension does not saturate for values of the embedding space dimension $m<9$. The duration of the time series does not allow accurate estimates of the attractor dimension for $m>9$. This behavior of D_e leaves the problem of determining the chaotic regime for $\alpha>5$ unresolved.

The problem of controlling the behavior characteristics of a vircator system has recently become important. Thus, an REB generator with supercritical current and controlled feedback, called a virtode, is of particular interest.[8] It was demonstrated experimentally that the feedback has a strong influence on the characteristics of the device.

An analysis is made of the case when the feedback signal is taken from the virtual cathode region. Figures 1d–1f and 2d–2f show the oscillation characteristics in a system with fixed α for various values of τ: 20 (d), 40 (e), and 60 (f).

The investigations reveal that the dynamics of the system is determined by the relation between the characteristic scale T_0 of the oscillations in the system and the feedback delay time τ. Incorporation of feedback with a short delay time ($\tau<T_0/2$ complicates the system dynamics: a noise pedestal appears in the spectrum and the embedding space dimension is $m>10$ (Figs. 1d and 2d). This is caused by the

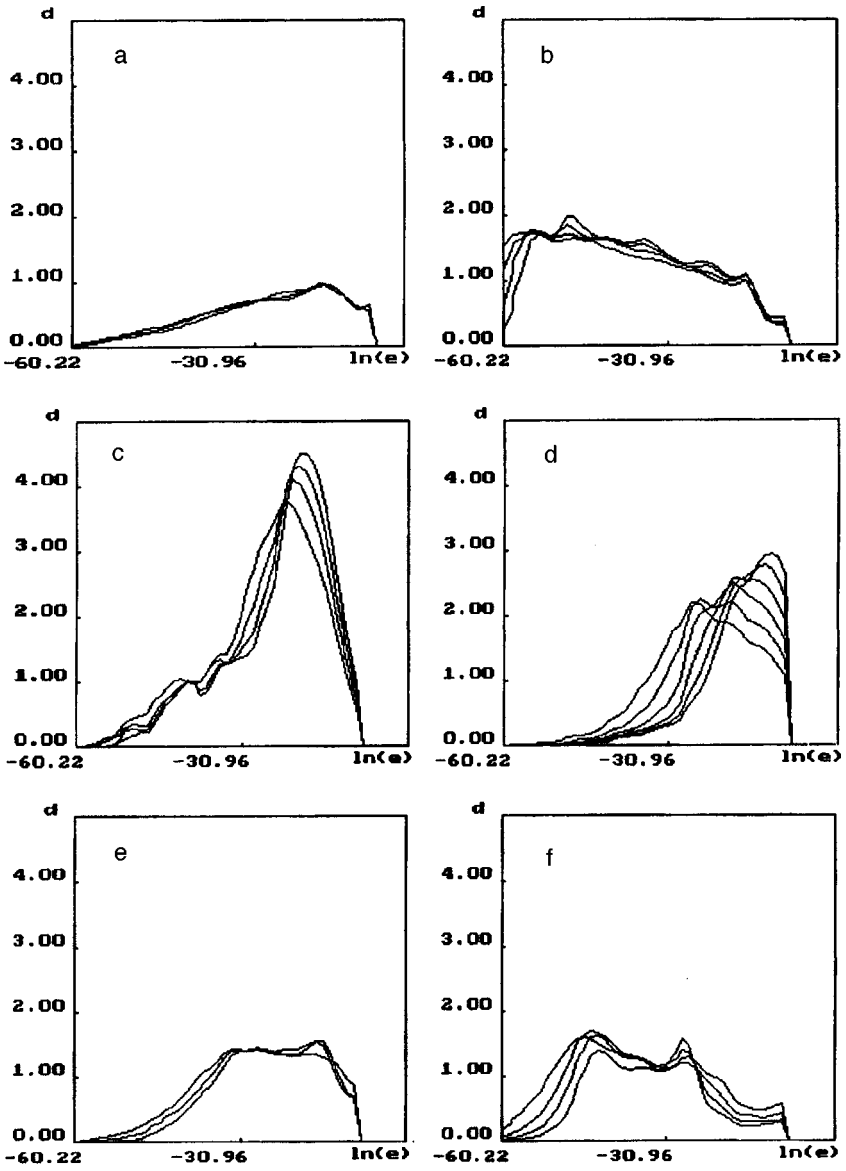

FIG. 2. Slope of the correlation integral of the reconstructed attractor for various embedding space dimensions m in various behavior regimes.

excitation of a many degrees of freedom in the system. For $\tau > T_0/2$ ordering of the oscillations is observed until regular motion is established in the system. The form of the phase portrait, the dimension of the limit set, and the spectral composition of the radiation all vary as a function of τ. In this case, the characteristic oscillation frequency varies in the range $(0.7-1.5)\omega_0$, where ω_0 is the free oscillation frequency of the virtual cathode. Note that variation of the delay time of the feedback signal can also be used to control the amplitude of the virtual cathode oscillations and thus the level of the generated power in the system. There is an optimum delay time τ for which the electron interaction power P_e in the system has a maximum. The ratio $(P_e)_{\max}/(P_e)_{\min} \approx 0.5$ is obtained and the ratio of $(P_e)_{\max}$ to the free oscillation power of the virtual cathode is of the order of 0.65.

Figure 1g shows the oscillation characteristics of the system for the case where feedback is introduced in the collector region. The oscillations are highly irregular, the power spectrum is noiselike, and the attractor has a comparatively uniform structure.

[1] L. E. Thode, in *High Power Microwave Sources*, edited by V. L. Granatstein and I. Alexeff (Artech House, Boston, 1987), Chap. 14, p. 507.
[2] C. K. Birdsall and A. B. Langdon, *Plasma Physics via Computer Simulation*, McGraw–Hill, New York (1985); Energoatomizdat, Moscow (1989), 452 pp.
[3] A. G. Sveshnikov and S. A. Yakunin, Mat. Model. **1**(4), 1 (1989).
[4] V. G. Anfinogentov, in *Proceedings of the Third International Specialist Workshop on Nonlinear Dynamics of Electronic Systems. University College Dublin, 28–29 July, 1995*, pp. 79–82.
[5] M. V. Kuzelov and A. A. Rukhadze, *Electrodynamics of Dense Electron Beams in Plasmas* [in Russian], Nauka, Moscow (1990), 336 pp.
[6] P. Grassberg and J. Procaccia, Phys. Rev. Lett. **50**, 346 (1983).
[7] A. A. Kipchatov, L. V. Krasichkov, and A. V. Andrushkevich, in *Proceedings of the International Seminar on Nonlinear Circuits and Systems*, Moscow, 1992, Vol. 2 [in Russian], pp. 308–317.
[8] N. N. Gadetskiĭ, I. I. Magda, S. I. Naĭsteter *et al.*, Fizika Plazmy **19**, 530 (1993) [Plasma Phys. Rep. **19**, 273 (1993)].

Translated by R. M. Durham

Stable current oscillations accompanying magnetron sputtering of oxide targets

A. Kh. Abduev and A. M. Magomedov

Institute of Physics, Dagestan Scientific Center
(Submitted November 27, 1997)
Pis'ma Zh. Tekh. Fiz. **24**, 58–62 (March 12, 1998)

Undamped total current oscillations were observed for the first time during dc magnetron sputtering of oxide ceramic targets. It was shown that these oscillations were caused by the continuous generation of atomic oxygen as a result of chemisorption–desorption processes at the surface of the target heated by ion bombardment. Oscillations of an attachment nature (similar to Trichel oscillations) were observed at low pressures ($P=4\times10^{-4}$ Torr).
 [S1063-7850(98)01103-3]

Instabilities of discharges in electronegative gases are well-known and have been widely studied.[1–3] In particular, regular current oscillations between planar electrodes, similar to Trichel oscillations, are predicted in Ref. 4 at gas pressures of 1–4 Torr.

Here we report the observation of stable current oscillations caused by the continuous generation of atomic oxygen at the surface of zinc oxide ceramic targets during dc magnetron sputtering of the targets at pressures less than 5×10^{-4} Torr.

A block diagram of the apparatus is shown in Fig. 1. The magnetron sputtering system was supplied by a pulsed rectified voltage at twice the line frequency. The targets were pressed and annealed zinc oxide ceramic plates with a resistivity of around $1\ \Omega\cdot$ cm and overall dimensions of $110\times375\times5$ mm.

The discharge gap was 10 cm and the working gas was argon or an $Ar–O_2$ mixture. Oscilloscope traces of the current and voltage, and also the discharge current–voltage characteristics, were studied as a function of the power supply system, and the gas composition and pressure.

Figure 2 gives the results of measurements made in an $Ar:O_2=3:1$ atmosphere. All the measurements were made at an applied voltage $U=550$ V and discharge current $I=6$ A. When the circuit contains no capacitance C connected in parallel to the discharge gap, the oscilloscope traces of the voltage and current, and the current–voltage characteristics at $P=4\times10^{-4}$ Torr corresponds to those of a normal glow discharge (Fig. 2aI and 2aII).

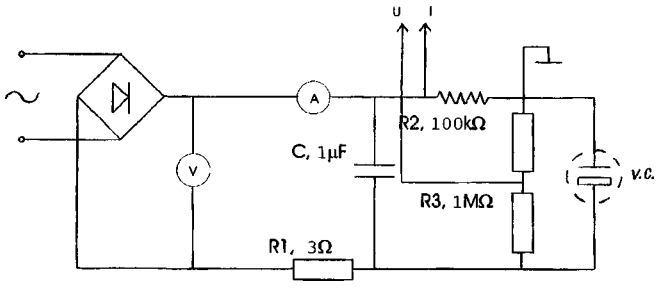

FIG. 1. Power supply to system for magnetron sputtering and measurement of the discharge characteristics. V.C. is the vacuum chamber.

The results of the measurements with a capacitance C incorporated in the circuit at different pressures are plotted in Figs. 2b–2d. At $P>6\times10^{-4}$ Torr the voltage and current traces reveal damped oscillations at the instant of breakdown of the discharge gap (Fig. 2b). The current–voltage characteristic at this stage indicates that the current pulses lag be-

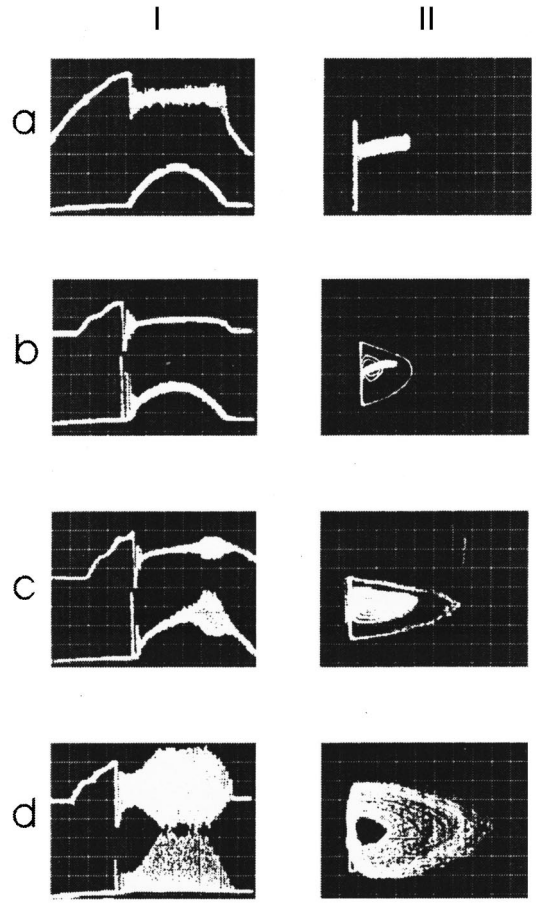

FIG. 2. Oscilloscope traces of voltage (upper traces) and current (lower traces) (I), and current–voltage characteristic (II) of the discharge under various conditions: a—with capacitance C in supply circuit; b, c, d—with capacitance C at pressures of 6×10^{-4} Torr, 5×10^{-4} Torr, and 4×10^{-4} Torr, respectively.

hind the voltage. The characteristic then corresponds to the static characteristic of a normal glow discharge.

A reduction in pressure ($P \approx 5 \times 10^{-4}$ Torr) leads to the generation of current oscillations near the maximum voltage (Fig. 2c). At pressures of $3 \times 10^{-4} < P < 5 \times 10^{-4}$ Torr the discharge becomes completely oscillatory and the constant component of the discharge current is negligible. In this case, the current–voltage characteristic contains no elements of the static characteristic. An increase or decrease in the anode–cathode gap or the capacitance C causes a constant current component to appear until the oscillations disappear. A reduction in the pressure below $P \approx 3 \times 10^{-4}$ Torr leads to quenching of the discharge. We did not observe any appreciable variation of the oscillation frequency as a function of the distance between the electrodes or the ratio of the partial gas pressures calculated in Ref. 4.

We studied the discharge characteristics in a pure Ar atmosphere in order to determine the role of oxygen in the formation of oscillations. Oscillations were also observed in this case but after a few minutes of sputtering they were completely damped and the discharge was then uninfluenced by the capacitance. A discharge in an argon atmosphere blackened the target as a result of oxygen depletion of the surface layer. The oscillating regime was only restored after the target had been sputtered for a few minutes in an $Ar–O_2$ atmosphere, which oxidized the surface layer. This behavior suggests that the discharge current oscillations are caused by desorption of atomic oxygen from the surface of the target and by the formation of negative O^- ions as a result of electron attachment. The undamped nature of the oscillations is caused by the processes taking place at the surface of the target. It is known that ion bombardment of zinc oxide leads to desorption of atomic oxygen.[5,6] It is also known that the temperature of the target surface during magnetron sputtering is close to the melting point (decomposition) of the target. Our previous investigations[7] showed that the processes at the surface of a zinc oxide target take place as follows:

– Desorption of atomic oxygen under ion bombardment. Oxygen atoms are ionized and confined by the field near the surface of the target.

– Sublimation of zinc and its oxidation near the target. The oxygen deficit in the heated surface layer is made up by oxygen supplied to the chamber as part of the working gas. Thus, in magnetron sputtering the molecular oxygen contained in the bulk is continuously converted into atomic oxygen at the surface of the target.

The presence of a capacitance C in the supply circuit changes the external current–voltage characteristic of the source and, combined with the fluctuations caused by the attachment instability, leads to a delay of the feedback with respect to voltage and to the formation of current oscillations.[8] A model was proposed in Ref. 4 to describe the dynamics of the distribution of the positive and negative regions of the space charge and potential in a discharge gap at $P \approx 1-10$ Torr. However, further investigations are required before the oscillation mechanism can be reliably determined.

This pulsed magnetron sputtering regime in a dc system revealed various advantages for applications. These include a multiplication of the maximum sputtering rate and increased scope for controlling processes in the gas phase in reactive magnetron sputtering. We propose to report the results of further studies in our next publication.

[1] Yu. P. Raĭzer, *Gas Discharge Physics* (Springer, New York, 1991; Nauka, Moscow, 1992).
[2] W. L. Nighan and W. J. Wiegand, Phys. Rev. A **10**, 922 (1974).
[3] R. Morrow, Phys. Rev. A **32**, 1799 (1985).
[4] I. Peres and L. C. Pitchford, J. Appl. Phys. **78**, 774 (1995).
[5] S. R. Morrison, *The Chemical Physics of Surfaces* [Plenum Press, New York (1977); Mir, Moscow (1980), 488 pp.].
[6] A. A. Lisachenko, I. F. Moiseenko, and A. A. Glebovskiĭ, Izv. Akad. Nauk SSSR, Ser. Fiz. **46**, 2274 (1982).
[7] A. Kh. Abduev, A. M. Magomedov, and Sh. O. Shakhshaev, Neorg. Mater. **33**(1), 1 (1997).
[8] V. N. Melekhin and N. Yu. Naumov, Zh. Tekh. Fiz. **54**, 1521 (1984) [Sov. Phys. Tech. Phys. **29**, 888 (1984)].

Translated by R. M. Durham

Condition for a time-constant current in a high-current planar diode

S. Ya. Belomyttsev, S. D. Korovin, and I. V. Pegel'

Institute of High-Current Electronics, Siberian Branch of the Russian Academy of Sciences, Tomsk
(Submitted January 5, 1997)
Pis'ma Zh. Tekh. Fiz. **24**, 63–69 (March 12, 1998)

The conditions required to achieve a constant current from an explosive cathode during the pulse in a high-current planar diode are calculated. © *1998 American Institute of Physics.*
[S1063-7850(98)01203-8]

High-current electron beams with large cross sections (hundreds of square centimeters) and pulse lengths between a few and tens of nanoseconds are used in various radiation technologies. These beams are formed in planar diodes with cathodes based on explosive electron emission.[1] The use of direct-action accelerators based on coaxial shaping lines[2] as pulsed voltage sources allows beams to be generated with pulse repetition frequencies of hundreds of hertz.[3]

One problem encountered in the development of cathodes for planar diodes is to ensure that the diode impedance remains constant during the pulse. Unless special measures are taken, the impedance of a planar explosive-emission diode may decrease by a factor of 2–3 within approximately 20 ns (Ref. 3), which causes an increase in current and mismatch between the diode and the oscillator. This last factor reduces the electron energy during the pulse, which is undesirable for technological applications.

It is well-known[4] that if the cathode plasma in a high-current diode expands during the pulse over a distance comparable with the diode gap, this reduces the impedance of the diode. In the present study, however, we consider the case where the expansion of the cathode plasma during the pulse is negligible compared with the diode gap.

We examine the conditions required to achieve a constant impedance for a planar diode with an explosive-emission cathode.

If the diode is planar (Fig. 1), we assume that the electrons propagate along the normal to the electrodes. The electrostatic potential φ satisfies the Poisson equation

$$\Delta\varphi = -4\pi\rho, \tag{1}$$

where ρ is the space charge density in the diode. Since $\rho = j/V$, where j is the current density in the diode and V is the electron velocity, we obtain

$$d^2\varphi/dx^2 = -4\pi j/V. \tag{2}$$

Introducing the notation $j_0 = -j$ and assuming that

$$\gamma = 1 + \frac{e\varphi}{mc^2} = (1 - V^2/c^2)^{-1/2}, \tag{3}$$

where m is the electron mass, e is the modulus of the electron charge, and γ is a relativistic factor, we have

$$\frac{mc^2}{e}\frac{d^2\gamma}{dx^2} = \frac{4\pi j_0}{c}(1-\gamma^{-2})^{-1/2}. \tag{4}$$

Multiplying Eq. (4) by $d\gamma/dx$ and integrating, we obtain

$$\frac{mc^2}{2e}\left(\frac{d\gamma}{dx}\right)^2 = \frac{4\pi j_0}{c}\sqrt{\gamma^2-1} + C_1, \tag{5}$$

where C_1 is the integration constant. Assuming that $d\gamma/dx = -eE/mc^2$, we rewrite Eq. (5) in the form

$$-\frac{E^2}{8\pi} + \frac{j_0}{e}mc\sqrt{\gamma^2-1} = \text{const}. \tag{6}$$

At the surfaces of the electrodes, the left-hand side of expression (6) has the meaning of the total pressure, which is made up of the electric field and electron pressures. Thus, the values of the total pressure at the cathode and the anode are the same. The field pressure creates a force at the electrodes directed into the diode, while the beam pressure creates a force acting in the opposite direction. The force acting on the diode as a whole is zero as a result of the constant momentum in a steady-state system (it is assumed that the electron flux is absorbed at the anode and does not leave the limits of the diode).

If the electrons leave the cathode at zero (in a known approximation) velocities, the pressure on the cathode is

$$p_k = E_k^2/8\pi, \tag{7}$$

where E_k is the electric field strength at the cathode. If the cathode has an unlimited emission capacity, then $E_k = 0$ and the total pressure on the cathode is $p_k = 0$. The pressure on the anode is

$$p_A = -\frac{E_A^2}{8\pi} + \frac{j_0}{e}mc\sqrt{\gamma^2-1}, \tag{8}$$

where E_A is the electric field strength at the anode. If $p_k = 0$ and thus $p_A = 0$, the field pressure at the anode is balanced by the electron pressure.

Let us now assume that the cathode is an inhomogeneous but periodic structure. Neglecting the magnetic field, we will clearly have periodicity in the electric field and the particle flux. It is easy to see that in this case, the field- and particle-related fluxes of the x component of the momentum across the lateral (parallel to the x axis) surfaces of a prism-shaped periodic cell isolated in the diode are zero. Thus, the x components of the forces acting on the anode and cathode ends of the cell are of equal magnitude but of opposite sign. This holds on average in the diode.

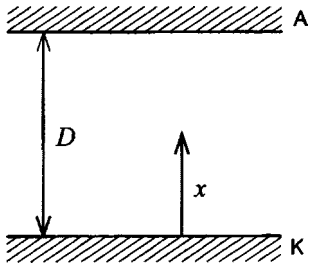

FIG. 1.

In a diode with a planar cathode having a continuous emitting surface, the current is constant with respect to time. However, it is difficult to ensure that the entire surface of the cathode is covered with plasma for a few nanoseconds. The cathode is generally constructed as some periodic structure to ensure that the explosive emission plasma appears rapidly. Let us assume that the linear dimensions of the periodicity are much smaller than the diode gap D. Neglecting the self-induced magnetic field, we can assume that the electron velocity (except for the region near the emitting surface) is perpendicular to the electrodes.

The number of explosive emission centers at the cathode increases rapidly only in the first few nanoseconds of the pulse. However, the emitting surface continues to grow subsequently as a result of expansion of the plasma, until neighboring plasmas merge. In this case, the current in the diode can increase even at constant voltage.

We shall assume that

$$D \gg V_{\mathrm{pl}} T, \tag{9}$$

where V_{pl} is the average plasma expansion velocity and T is the pulse duration. The variation of the diode gap during the pulse can then be neglected.

It is generally assumed that an increase in current in a diode is caused by an increased emitting surface at the cathode. The mechanism for this effect should be refined taking into account the previous reasoning on the balance of forces in the diode. In this case, the current increases when an increase of the emitting surface leads to a reduction in the x component of the field force at the cathode. On the other hand, it is known that in a coaxial diode with a longitudinal guiding magnetic field, the current is constant if the entire edge of a thin annular cathode is exploded (Fig. 2). In spite of the plasma expansion, the axial pressure on the cathode is zero and this explains the constant current.[5,6] Thus, in order

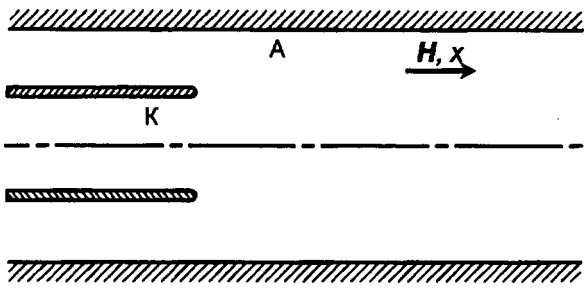

FIG. 2.

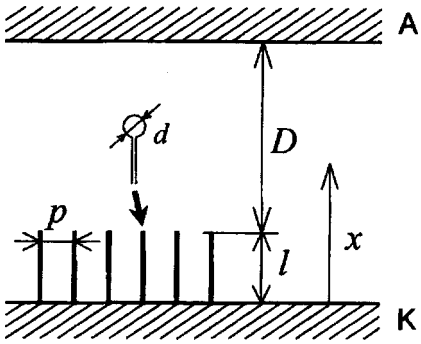

FIG. 3.

to ensure a constant current in a planar diode, the field pressure on the cathode must remain constant during expansion of the plasma. In principle, this can be achieved.

Let us take a cathode in the form of a plane surface on which thin parallel knife edges are mounted (Fig. 3). The distance between the knife edges is $p \ll l$ and $p \ll D$. If their edges are covered with plasma, the pressure on the cathode in the x direction is close to zero and is almost independent of the plasma expansion. This can be attributed to the weak electric field at the planar base of the cathode since $p \ll l$.

We now assume that l/p is such that any change in the field pressure on the cathode can be neglected. Nevertheless, there is still a factor causing the current to vary with time. This is because the pressure on the anode is the sum of the field and electron pressures and these pressures are self-consistent. During expansion of the plasma, the beam geometry may vary and as a result, the ratio between the field and particle pressures also varies, even though the total pressure on the anode remains the same. However, when the pulse length is short, the plasma leading edge covers a distance much smaller than the characteristic linear dimensions in the diode, and so we predict that the time variation of the current will be negligible.

Numerical calculations made using the SuperSAM code (Institute of Nuclear Physics, Siberian Branch of the Russian Academy of Sciences) showed that in a periodic system (Fig. 3) with $p = 1$ cm, $U = 500$ kV, $D = 3$ cm, and $l = 1$ cm, the current I_1 per unit length of a single knife edge depends weakly on the diameter d of a cylindrical emitter positioned at its edge (curve *1* in Fig. 4). Curve *2* plotted for comparison corresponds to a diode with a 3 cm gap and emitters in the form of semicylinders of diameter d located directly on the cathode plane. In this case, a strong dependence $I_1(d)$ is found.

We note in passing that when the conditions $p \ll l$ and $p \ll D$ are satisfied, the current in the diode shown in Fig. 3 is similar to that in a homogeneous planar diode with the gap D. The numerical calculations showed that for the parameters given above, the difference is less than 5%.

Although the goal to be strived for when fabricating the cathode is quite clear, some difficulties may be encountered in attaining this goal. Simple thin metal knife edges are difficult to explode rapidly over the entire length of the edge, particularly at high pulse repetition frequencies. In addition, at high average pulse powers the knife edges undergo ther-

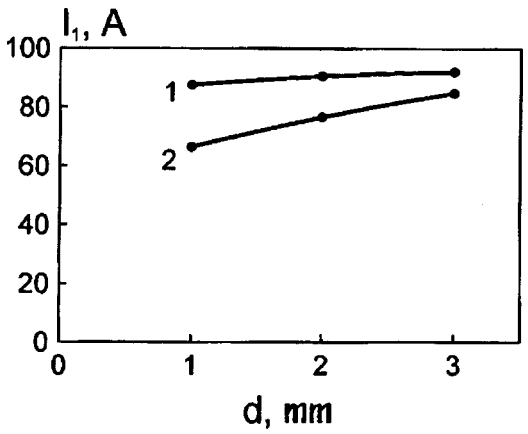

FIG. 4.

mal deformation. Fabrication of the knife edge in the form of a metal-dielectric contact[7] may well improve the uniformity of the emission along the edge both by reducing the electric field threshold of the explosive emission (and therefore reducing the size of the screening zone around each center[8]) and also because of the faster propagation of the plasma along the dielectric surface and the merging of neighboring plasmas.

[1] S. P. Bugaev, E. A. Litvinov, G. A. Mesyats, and D. I. Proskurovskiĭ, Usp. Fiz. Nauk **115**, 101 (1975) [Sov. Phys. Usp. **18**, 51 (1975)].
[2] A. S. El'chaninov, F. Ya. Zagulov, S. D. Korovin *et al.*, *Relativistic Rf Electronics Problems of Increasing Radiation Power and Frequency* [in Russian], Institute of Applied Physics, Academy of Sciences of the USSR, Gorkiĭ (1981), pp. 5–21.
[3] N. M. Bykov, V. P. Gubanov, A. V. Gunin *et al.*, Abstracts of papers presented at 10th International Pulse Power Conference, Albuquerque, 1995, paper 2–4.
[4] G. A. Mesiats and D. I. Proskurovsky, *Pulsed Electric Discharge in Vacuum* [Springer, New York (1989); Nauka, Novosibirsk (1984), 256 pp.].
[5] A. I. Fedosov, E. A. Litvinov, S. Ya. Belomyttsev, and S. P. Bugaev, Izv. Vyssh. Uchebn. Zaved. Fiz. **10**, 134 (1977).
[6] E. A. Litvinov, G. A. Mesyats, and A. I. Fedosov, Fiz. Plazmy **7**, 86 (1981) [Sov. J. Plasma Phys. **7**, 48 (1981)].
[7] G. A. Mesyats, IEEE Trans. Dielectr. Electr. Insul. **2**(2), 272 (1995).
[8] S. Ya. Belomyttsev, S. D. Korovin, G. A. Mesyats, Pis'ma Zh. Tekh. Fiz. **6**, 1089 (1980) [Sov. Tech. Phys. Lett. **6**, 460 (1980)].

Translated by R. M. Durham

One-dimensional diffuser for a three-dimensional imaging system

E. B. Bruĭ and V. V. Orlov

''S. I. Vavilov State Optical Institute'' All-Russian Scientific Center, St. Petersburg
(Submitted November 25, 1997)
Pis'ma Zh. Tekh. Fiz. **24**, 70–75 (March 12, 1998)

An analysis is made of a method of using a photographic plate to obtain a diffuser whose scattering indicatrix in one direction is more than two orders of magnitude wider than that in the perpendicular direction. This method involves recording a particular speckle pattern on a photographic plate. A description is given of the photochemical treatment of the plate used to ensure that the diffuser does not possess a zeroth diffraction order. An analysis is made of the difference between the theoretical and experimentally measured scattering indicatrix of the diffuser. This difference is attributable to the nonlinearity of the diffuser fabrication process. © *1998 American Institute of Physics.* [S1063-7850(98)01303-2]

A new method of producing three-dimensional images based on forming a matrix of focused aspects of a scene was proposed in Ref. 1. In the experimental section of Ref. 2, the efficiency of the method was checked for the particular case when a three-dimensional display reproduces only the horizontal parallax. In this case, a one-dimensional diffuser is used, which only scatters the radiation in the vertical direction and thereby broadens the window of observation in this direction. In order to ensure that the observed image possesses uniform brightness, the diffuser should not exhibit a zeroth diffraction order. Here we consider a method of obtaining such a diffuser.

The one-dimensional diffuser was a photograph of a speckle pattern formed by a vertical line of light. (Here and subsequently the horizontal direction was taken as the direction in which the parallax should be reproduced, i.e., the direction of the axis linking the pupils of the observer's eyes). The line of light was formed by a coherent cylindrical light wave ($\lambda = 632.8$) focused onto mat glass. The intensity distribution of the diffuse beam was recorded using a 123 $\times$ 102 mm PFG-03C photographic plate positioned 300 mm from the mat glass and oriented so that the longest side of the plate was perpendicular to the luminous line on the mat glass. The continuity of the diffuse beam intensity on the surface of the photographic plate was characterized by the following quantities: the maximum intensity was at the center of the plate, and was taken as 100%, the intensity at the upper and lower edges was 73% and at the right and left edges, 53%. The exposure at the center of the plate was 0.8 mJ/cm^2.

The photochemical treatment of the exposed photographic plate included the following operations:

1) Development in PRG developer
2) Washing in water
3) Intensification in a solution containing $AgNO_3$
4) Washing in water
5) Fixing in F8 fixer
6) Washing in water
7) Bleaching in modified R10 bleaching agent
8) Washing in water
9) Dehydration in 50% and 100% solutions of isopropyl alcohol
10) Drying

High-contrast, nonhardening developing was used to obtain the highest possible image density uniformly over the entire thickness of the layer. The intensification step was introduced to enhance the relief on the surface of the layer. The nonlinear nature of the intensifying treatment appreciably increased the optical density in the exposed sections of the photolayer, which combined with the hardening bleaching treatment, enhanced the surface relief.[3] During the hardening bleaching treatment, gelatin molecules hardened around developed silver grains. The composition of the bleaching tank was selected to create the optimum bleaching conditions for the layer. During the subsequent dehydration treatment in alcohol solutions, an image formed in the layer as a result of modulation of the refractive index of the hardened and nonhardened gelatin, similar to the processes taking place in layers of bichromated gelatin. As a result of this photochemical treatment, the image of the speckle pattern in the photographic layer consisted of three components: bleached silver grains, hardened gelatin, and surface relief. All three components combined to produce sufficient modulation of the optical thickness of the diffuser to completely eliminate the zeroth diffraction order. An extremely weak zeroth diffraction order was observed at the edges of the diffuser where it was caused by the lower intensity of the diffused beam during exposure of the plate.

We measured the scattering indicatrix of this one-dimensional diffuser in the vertical and horizontal directions at wavelength 632.8 nm. The vertical scattering indicatrix is shown in Fig. 1. The half-width of the indicatrix, i.e., the full width at half-maximum, in the vertical direction is 18°. Figure 2 shows the scattering indicatrix in the horizontal direction, which has a half-width of 6.6 arc min.

We now discuss these results. The scattering indicatrix of the diffuser is determined by the spectrum of spatial frequencies of its amplitude transmission. If the diffuser fabrication process is linear, i.e., the amplitude transmission of the photoplate depends linearly on the exposure, the spec-

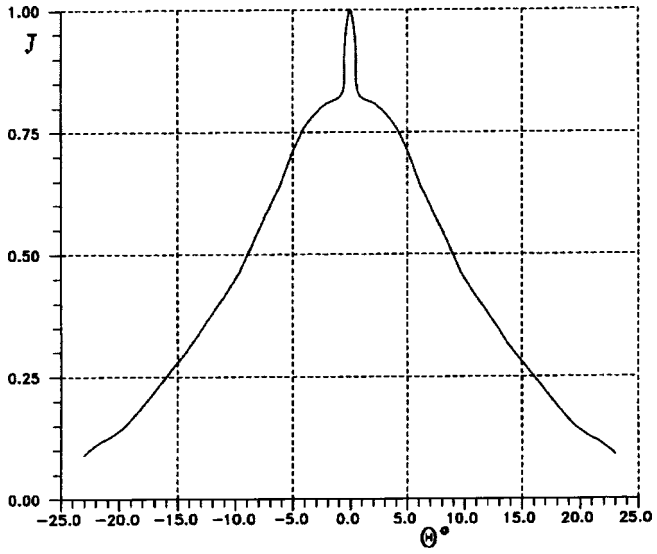

FIG. 1.

trum of spatial frequencies of the amplitude transmission is proportional to the spectrum of spatial frequencies of the intensity distribution of the diffuse beam in the plane of the photographic plate. It is easy to show that in this case, the diffuser should scatter the radiation in such a way that the half-width of the scattering indicatrix in the vertical and horizontal directions is equal to the corresponding angular dimensions of the line of light on the mat glass when this is observed from the center of the photographic plate. The width of the scattering indicatrix in the vertical and horizontal directions should be twice the angular dimension of the line of light in the given direction.[4]

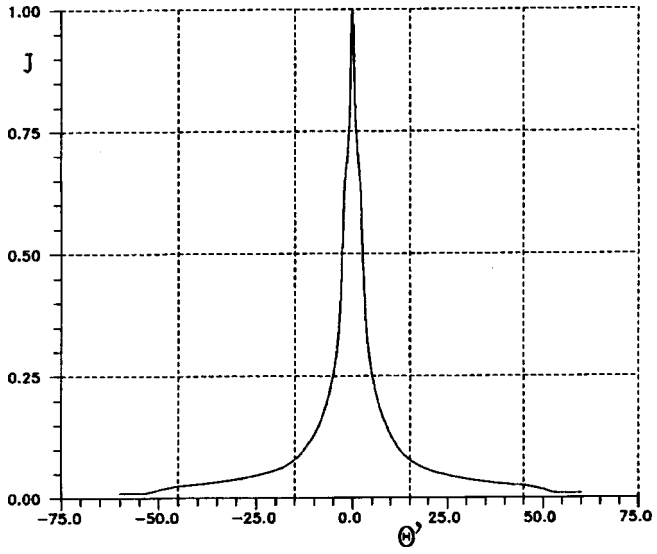

FIG. 2.

The diffuser fabrication process used here is nonlinear since the amplitude transmission of the diffuser is a pure phase process. As a result of this nonlinearity, the spectrum of spatial frequencies of the diffuser changed substantially and was enriched in higher spatial frequencies. It can be seen from Fig. 1 that the half-width of the scattering indicatrix in the vertical direction is 18°, which is 2.25 times greater than the 8° angular dimension of the line of light on the mat glass in this direction. In order to estimate the influence of the nonlinearity of the fabrication process on the scattering indicatrix in the horizontal direction, we measured the intensity distribution of the line of light in this direction. This intensity distribution comprised a high narrow peak 23 μm wide, located on a plateau 345 μm wide. This nonuniform intensity distribution in the line of light was caused by the aberrations of the cylindrical lens used to form it. The angular dimensions of the peak and the plateau of the intensity distribution relative to the center of the photographic plate were 0.25′ and 3.8′, respectively. Comparing these values with the half-width of the scattering indicatrix in the horizontal direction 5.2′ and its width 110′ (Fig. 2), we find that as a result of the nonlinearity, the half-width of the scattering indicatrix, which depends on the peak width, was increased 21 times and the width of the indicatrix, which depends on the plateau width, was increased 14 times.

Bearing in mind that the half-width of the scattering indicatrix in the vertical direction was only increased 2.25 times, we see that the nonlinearity of the fabrication process of the one-dimensional diffuser has a stronger influence on the low spatial frequencies of the amplitude transmission of the diffuser, responsible for scattering in the horizontal direction, compared with the high spatial frequencies responsible for scattering in the vertical direction. This one-dimensional diffuser was used to reconstruct an image which only reproduces one horizontal parallax using a system similar to that described in Ref. 2. The experiment showed that the presence of the horizontal component of the scattering indicatrix reduces the contrast of the image. For the horizontal component not to influence the quality of the observed image, its width should not exceed the 1′ angular resolution of the eye. In order to obtain such a narrow scattering indicatrix, a narrower, diffraction-limited line of light must be formed on the surface of the mat glass.

The authors would like to thank Yu. N. Denisyuk for useful discussions of this work.

This work was supported by the Russian Fund for Fundamental Research, Grant No. 97-02-18285, and also by the CRDE International Fund, Grant No. RE2-162.

[1] Yu. N. Denisyuk, Pis'ma Zh. Tekh. Fiz. **22**(9), 92 (1996) [Tech. Phys. Lett. **22**, 385 (1996)].
[2] Yu. N. Denisyuk, V. B. Markov, and N. M. Ganzherli, Opt. Spektrosk. **84**, No. 1 (1998) [Opt. Spectrosc. **84**, 94 (1998)].
[3] E. B. Brui and I. V. Galashkina, Proc. SPIE **2108**, 196 (1993).
[4] J. W. Goodman, *Introduction to Fourier Optics* [McGraw-Hill, New York (1968); Mir, Moscow (1970), 364 pp.].

Translated by R. M. Durham

Instability of plane Couette flow of two-phase liquids

V. Ya. Rudyak, E. B. Isakov, and E. G. Bord

Novosibirsk State Academy of Civil Engineering
(Submitted June 12, 1997)
Pis'ma Zh. Tekh. Fiz. **24**, 76–80 (March 12, 1998)

The stability of plane Couette flow of a disperse liquid (gaseous or liquid suspension) is investigated. It is shown that in contrast to the flow of a pure liquid (gas), above a certain threshold particle mass density, this flow begins to become unstable to infinitesimal perturbations.
 [S1063-7850(98)01403-7]

It is well known that plane Couette flow of a single-phase liquid is stable relative to infinitely small perturbations.[1] In our studies[2–5] we systematically investigated the stability of flows of disperse liquids. We established that the presence of solid particles in the stream radically alters the evolution of perturbations in bounded and free flows. In particular, when the particle distribution is nonuniform, a new necessary condition is obtained for instability of the flow of two-phase liquids in the inviscid approximation:[2] $(\rho U')'=0$, where $\rho(y)$ is the mass density profile of the medium, $U(y)$ is the steady-state profile of the flow velocity. Here and subsequently the prime indicates differentiation with respect to y.

In accordance with this condition, Couette flow with any nonmonotonic density distribution $\rho(y)$ should be unstable. This important conclusion is unexpected and requires verification. Here we study the stability of plane Couette flow relative to small perturbations.

We consider the flow of a disperse medium consisting of a mixture of an incompressible carrier liquid (gas) and solid spherical particles of radius a. The bulk density of the disperse phase is assumed to be low so that particle interaction can be neglected. The dynamics of this system is described by the equations of two-fluid hydrodynamics.[2–5]

It was shown in Ref. 2 that the Squire theorem is satisfied for an arbitrary distribution of the disperse phase, so that the analysis can be confined to studying the evolution of two-dimensional perturbations. In this case, the problem is reduced to solving the equation[2,5]

$$(W-c)\Delta\psi - W''\psi + (\psi J f')' = \frac{1}{i\alpha\ \mathrm{Re}}\Delta^2\psi,$$

$$W(y)=U+fJ, \quad J=\frac{U-c}{1+i\alpha \mathrm{S}\ \mathrm{Re}(U-c)}, \quad \Delta=\frac{d^2}{dy^2}-\alpha^2 \tag{1}$$

for the stream function of small perturbations of the carrier liquid

$$\varphi(x,y,t)=\psi(y)\exp[i(\alpha x-\omega t)] \quad (u_x=\varphi', \quad u_y=-i\alpha\varphi)$$

with the wave number α, frequency ω, and phase velocity $c=\omega/\alpha$. Here $U=U(y)$ is the velocity profile of the unperturbed flow, $f=f(y)$ is the mass density profile of disperse-phase particles in the unperturbed flow, and $\mathrm{Re}=U_0 L\rho_f/\mu$ is the Reynolds number. The parameter $\mathrm{S}=\rho_p\mu/\rho_f KL^2$ is described as the relaxation time of the medium and characterizes the physical properties of a two-phase liquid, where L is the characteristic linear scale of the flow (for plane Couette flow this is the half-width of the channel), U_0 is the characteristic flow velocity, ρ_f is the density of the carrier liquid, ρ_p is the density of the particle continuum, μ is the coefficient of viscosity of the carrier liquid, and K is the hydrodynamic drag coefficient of the dispersed particles.

Here we consider plane Couette flow with the dimensionless velocity profile $U=y$ and boundaries at $y=\pm 1$. The usual conditions of nonslipping and nonpenetrating flow are set at the boundaries for the stream function. Equation (1) was solved numerically using tridiagonal inversion and the τ method. The distribution profile of the disperse phase was taken as a Gaussian function with the maximum of the density f_0 on the flow axis and characteristic width σ: $f(y)=f_0\exp(-y^2/\sigma^2)$. In the present work this width is always $\sigma=0.3$, which corresponds to the condition when almost all the particles are in the inner region of the flow; the relaxation time of the medium is $\mathrm{S}=10^{-7}$. The particle density f_0 was varied.

In single-phase Couette flow we can identify four perturbation modes having the lowest damping rates (curves *1–4* in Fig. 1). Three of these modes (curves *1–3*) are wall modes and thus react weakly to the presence of particles in the axial zone so that the damping rate of these perturbation either remains the same or even increases slightly with increasing particle density. The fourth mode (curve *4*) is an axial mode, and its behavior changes substantially in two-phase flow (curves *5* and *6*). The damping rate of this mode decreases as the particle mass density increases and after a certain threshold density $f_0\geqslant 0.2275$ has ben reached, the perturbations of this mode begin to grow. The Couette flow becomes unstable with respect to infinitely small perturbations. The phase velocity of the axial perturbations is zero and the frequency is also zero, $\omega_r=\alpha c_r=0$, so that for $\omega_i>0$ the unstable perturbation is a monotonically growing deformation of the velocity profile.

In the (α, Re) plane we can identify the region of instability of the disperse Couette flow bounded by a neutral curve, as shown in Fig. 2. Curve *1* corresponds to flow with the particle density $f_0=0.2275$, which is close to the thresh-

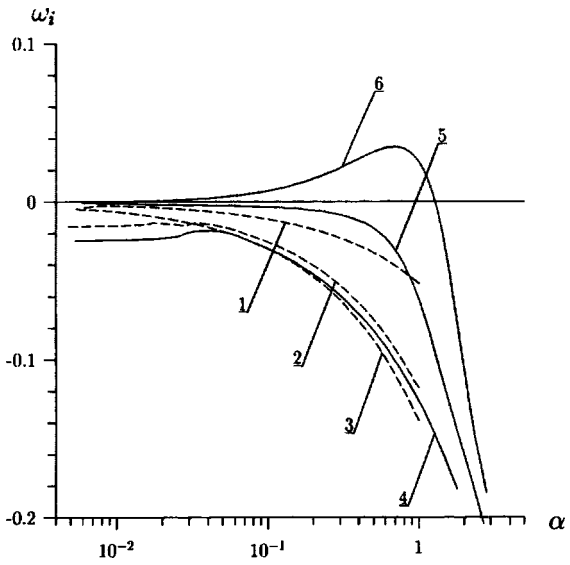

FIG. 1.

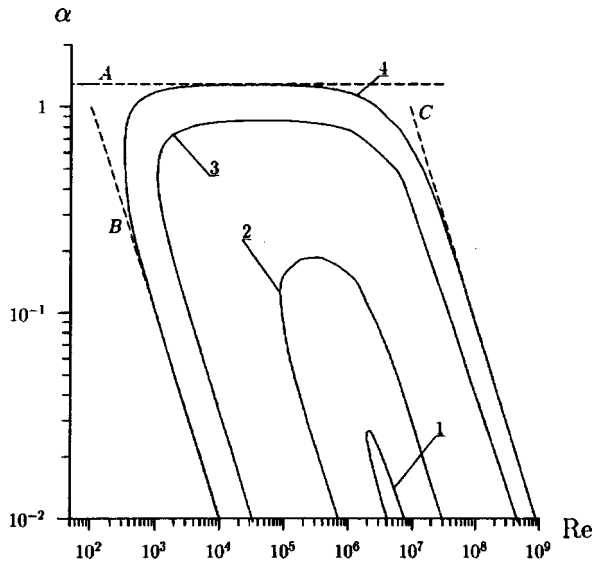

FIG. 2.

old value. For these particle densities the flow is only unstable to long-wavelength perturbations ($\alpha<0.03$) and is characterized by high Reynolds numbers $\mathrm{Re}>10^6$. As the density of the disperse phase increases, the region of instability grows rapidly (curves *2, 3,* and *4* correspond to mass densities $f_0=0.23$, 0.3, and 0.4, respectively) and develops a characteristic profile which clearly reveals three asymptotic branches (curves *A*, *B*, and *C* in Fig. 2). It can be shown that the asymptotic branch *A* corresponds to the inviscid limit $\mathrm{Re}\to\infty$ and at the same time, to the small particle limit $\mathrm{SRe}\to 0$, while branches *B* and *C* correspond to the small wave number limit.

To sum up, it can be confirmed that for fairly high particle mass densities, plane Couette flow becomes unstable against infinitesimal perturbations. As the particle relaxation time increases, the forces of interphase interaction decrease, which reduces the destabilizing influence of the disperse phase.

[1] A. S. Monin and A. M. Yaglom, *Statistical Fluid Mechanics*, Vol. 1 (MIT Press, Cambridge Mass) [Russ. original, Part 1, Nauka, Moscow (1967), 639 pp.].
[2] E. B. Isakov and V. Ya. Rudyak, Izv. Ross. Akad. Nauk Ser. Mekh. Zhidk. Gaza No. 5, 79 (1995).
[3] V. Ya. Rudyak and E. B. Isakov, Prikl. Mekh. Tekh. Fiz. **37**(1), 95 (1996).
[4] V. Ya. Rudyak, E. B. Isakov and E. G. Bord, Thermophys. Aeromech. **3**(1), 51 (1996)
[5] V. Ya. Rudyak, E. B. Isakov, and E. G. Bord, J. Aerosol Sci. **28**(1), 53 (1997).

Translated by R. M. Durham

Allowance for the contribution of self-adsorption in estimates of the interphase energy in a solid-metal–own-melt system

V. M. Yakovlev and A. I. Krestelev

Samara State Technical University
(Submitted July 3, 1997)
Pis'ma Zh. Tekh. Fiz. **24**, 81–83 (March 12, 1998)

An expression is verified to allow for the contribution of self-adsorption in the Young equation for the interface between a polycrystalline metal and its own melt using only two properties, the heat of fusion and the gram–atomic volume. The adequacy of this relation is established for precious and nontransition polyvalent metals.
[S1063-7850(98)01503-1]

It is known that the equilibrium values of the interphase free energies σ_{sl} at a crystal–liquid interface, calculated using the Young equation neglecting the contribution $\Delta\sigma_{\text{sa}}$ of self-adsorption (Γ_a), are usually much higher than the experimental data, even for single-component metal systems.[1–3] However, no formula to determine $\Delta\sigma_{\text{sa}}$ as a function of the properties of initial simple substances has been described in the literature.

Here we consider a possible method of obtaining a simple estimate of $\Delta\sigma_{\text{sa}}$ using the molar heats of fusion Ω_f of the metals.

To determine $\Delta\sigma_{\text{sa}}$, we use the familiar representations[4,5] of the interface as an individual phase, and the Gibbs adsorption equation

$$\Delta\sigma_{\text{sa}} = -\Gamma_a \Delta\mu_{sa}, \tag{1}$$

where $\Delta\mu_{\text{sa}}$ is the excess chemical potential of the adatoms relative to the substrate microparticles.

The suitability of this approach arises from the dominant role of the boundary monolayer in the accumulation of the free enthalpy.[6] In the limits of these representations, self-adsorption may be treated as the implementation of two stages: sublimation of an atom to the gas phase accompanied by expenditure of energy μ_s and its subsequent condensation into the adsorption layer with the release of energy μ_{sa}. We then have $\Delta\mu_{\text{sa}} = \mu_s - \mu_{\text{sa}}$. Assuming that the adlayer is semidisordered,[5] we take $\mu_{\text{sa}} \simeq 0.5(\mu_s + \mu_l)$, where μ_l is the energy of vaporization of a particle from the liquid phase. In this approximation we have $\Delta\mu_{\text{sa}} \simeq 0.5(\mu_s - \mu_l)$ so that Eq. (1) can be expressed in the final form

$$\Delta\sigma_{\text{sa}} \approx -0.5 N_A^{-1/3} V_A^{-2/3} \Omega_f. \tag{2}$$

Here it is assumed that Ω_f is the difference between the heats of sublimation and vaporization, V_A is the gram–atomic volume, $V_A = A\rho_s^{-1}$, A is the atomic mass, ρ_s is the density of the solid metal at the melting point, and N_A is Avogadro's number.

We used expression (2) to estimate $\Delta\sigma_{\text{sa}}$ for precious and nontransition polyvalent metals. Along with the parameters ρ_s and Ω_f and the equilibrium contact wetting angles θ of polycrystalline metals by their own melts,[3] the values of σ_l, σ_s, and σ_{sl} are also comparatively well-known for these metals (see Table I). This allows us to use the Young equation to find $\Delta\sigma_{\text{sa}}$

$$-\Delta\sigma_{\text{sa}} = \sigma_s - \sigma_l \cos\theta - \sigma_{sl}. \tag{3}$$

In addition to the values of $\Delta\sigma_{\text{sa}}$, Table I also gives the deviations δ of the estimates made using formula (2) from the results of the calculations using expression (3). It can be seen from the calculations that for these ten metals the average deviation δ is approximately 2.5%.

TABLE I. Interphase free energies and contributions of self-adsorption calculated by two methods (mJ/m^2).

Metal	σ_l (Refs. 7 and 8)	σ_s	σ_{sl}	$-\Delta\sigma_{\text{sa}}$ Formula(2)	$-\Delta\sigma_{\text{sa}}$ Formula (3)	δ, %
Cu	1330	1658 (Refs. 4 and 9)	217 (Ref. 12)	203.1	197.4	2.9
Ag	925	1148 (Refs. 10–12)	147 (Ref. 12)	133.7	137.0	2.4
Au	1145	1400 (Refs. 4 and 12)	161 (Refs. 4 and 14)	151.1	146.7	3.0
Al	871	1100 (Refs. 10 and 11)	141 (Ref. 14)	131.8	128.9	2.2
Ga	711	767 (Ref. 10)	56 (Ref. 14)	63.9	58.3	9.6
In	556	631 (Refs. 10 and 13)	62 (Ref. 14)	30.9	30.8	0.3
TI	465	555 (Ref. 10)	67 (Ref. 15)	54.1	55.1	1.8
Sn	562	683 (Refs. 9 and 13)	84 (Ref. 15)	64.0	65.1	1.5
Pb	464	556 (Ref. 10)	76 (Ref. 15)	40.1	39.7	1.0
Bi	382	499 (Refs. 10 and 11)	83 (Refs. 14 and 15)	86.6	87.1	0.6

We know that relation (2) was used earlier for an approximation of the interphase energy (see Refs. 1 and 5). However, the data given in Table I indicate that this correlation is only satisfied to within 18.7%.

It is therefore clear that expression (2) can be used to allow for the contribution of self-adsorption in the Young equation.

[1] V. V. Pavlov, *Adhesion of Metals and Alloys* [in Russian], Naukova Dumka, Kiev (1977), pp 62–66.
[2] B. B. Alchagirov and Kh. B. Khokonov, Teplofiz. Vys. Temp. **32**, 590 (1994).
[3] M. P. Dokhov, Metally No. 2, 16 (1994).
[4] V. Missol, *Surface Energy of Phase Separation in Metals* [in Russian], Metallurgiya, Moscow (1978), 176 pp.
[5] T. Utigard, Z. Metallkd. **84**, 792 (1993).
[6] L. Z. Mezey and J. Giber, Surf. Sci. **127**, L98 (1983).
[7] B. B. Alchagirov, *Author's Abstract of Thesis for Doctorate of Physico-mathematical Science* [in Russian], Kabardino–Balkarskaya State University, Nal'chik (1992), 39 pp.
[8] B. J. Keene, Int. Mater. Rev. **38**(4), 157 (1993).
[9] Kh. B. Khokonov, Yu. A. Orkvasov, and B. B. Alchagirov, Izv. Vyssh. Uchebn. Zaved. Fiz. **28**(10), 59 (1985).
[10] Kh. B. Khokonov, *Surface Effects in Melts and Their Product Solid Phases* [in Russian] Shtiintsa, Kishinev (1974). pp. 190–261.
[11] B. N. Oshcherin and G. G. Vavra, *Physics of Interphase Effects* [in Russian], Kabardino–Balkarskaya State University Press, Nal'chik (1979), pp. 53–57.
[12] R. M. Digilov, S. N. Zadumkin, V. K. Kumykov *et al.*, Fiz. Met. Metalloved. **41**, 979 (1976).
[13] I. G. Shebzukhova and Kh. B. Khokonov, *Adhesion of Melts and Soldering of Materials* [in Russian], Naukova Dumka, Kiev (1988) pp. 11–13.
[14] A. R. Miedema and F. J. A. den Broeder, Z. Metallkd. **70**, No. 1, 14 (1979).
[15] L. F. Mondolfo, N. L. Parisi, and G. J. Kardys, Mater. Sci. Eng. **68**, 249 (1984–1985).

Translated by R. M. Durham

Calculating the electromagnetic wave generated by the interaction between an ultrashort laser pulse and matter

I. A. Litvinenko and V. A. Lykov

Russian Federal Nuclear Center—All-Russian Scientific-Research Institute of Technical Physics
(Submitted July 7, 1997)
Pis'ma Zh. Tekh. Fiz. **24**, 84–88 (March 12, 1998)

A self-consistent solution is obtained for the problem of electron flux generation by interaction between an ultrashort laser pulse and a metal target. [S1063-7850(98)01603-6]

INTRODUCTION

The interaction between high-intensity ultrashort laser pulses and matter results in the generation of fast electrons with effective temperatures $T_f \approx 10$ keV and $T_f \approx 100$ keV for laser power densities on the target $q_l \approx 10^{16}$ W/cm^2 and $q_l \approx 10^{17}$–10^{18} W/cm^2, respectively.[1–3] The laser radiation is converted to fast electrons with an efficiency A_f of order tens of percent.[1]

On leaving the target, the fast electrons create electromagnetic fields which act so as to return them back to the generation zone. The motion of the electrons in the self-consistent electromagnetic fields beyond the target may lead to the dipole emission of an ultrashort, high-power electromagnetic wave. Since the emission region is small, the wave may subsequently be focused by the usual means for fundamental and applied research purposes. It is of interest to estimate the possible efficiency for conversion of the fast electron energy into an outgoing electromagnetc wave.

Here we present results of calculations made using the PM2D code to model the motion of the fast electrons and electromagnetic fields generated by the interaction of a picosecond laser pulse and a planar target at intensity $q_l \approx 10^{16}$ W/cm^2.

FORMULATION OF THE PROBLEM AND METHOD OF SOLUTION

Laser radiation focused in a beam of radius r_0 is incident normally on the surface of a metal plate. The time dependence of the supplied laser power $P(t)$ is described by an isosceles triangle with a base duration of 10^{-12} s and peak $P_{\max}=10^{10}$ W. Near the spot a surface source of fast electrons is defined with an isotropic angular distribution and a Maxwellian energy spectrum with the temperature

$$T_e(t)=100\times\left(\frac{P(t)}{\pi r_0^2 q_0}\right)^{1/3}. \tag{1}$$

Here T_e is in keV, the laser radiation power $P(t)$ is in watts, and $q_0=10^{18}$ W/cm^2.

The fast electron flux leaving the plate is given by

$$F(t)=6.3\times 10^{29}\times\left(\frac{P_{\max}}{\pi r_0^2 q_0}\right)\times A_f\times\left(\frac{P(t)}{\pi r_0^2 q_0}\right)^{2/3}, \tag{2}$$

where $F(t)$ is measured in particles/(cm^2/s) LB. and A_f is the efficiency of conversion of the laser radiation energy into fast electron energy.

The motion of the fast electrons is described by

$$\frac{d\mathbf{p}}{dt}=e\left[\mathbf{E}+\frac{1}{c}(\mathbf{v}\times\mathbf{H})\right],\quad \frac{d\mathbf{r}}{dt}=\mathbf{v},\quad \mathbf{v}=\frac{c\mathbf{p}}{\sqrt{p^2+m^2c^2}}, \tag{3}$$

where m is the electron rest mass.

The Maxwell equations in a cylindrical coordinate system are used to determine the fields. The initial conditions are taken as zero. The boundary $z=0$ (surface of the plate) is assumed to be conducting ($E_r=0$). The other boundaries $z=z_{\max}$ and $r=r_{\max}$ are also conducting, but they are some distance away and do not influence the field distribution inside the spot.

The calculation algorithm of our PM2D method is based on splitting into physical processes, which implies systematic modeling at each time step:

– the injection of fast electrons;
– motion of the electrons in electric and magnetic fields;
– the electron current distribution in the region;
– the electric and magnetic fields.

Making the time step small compared with the characteristic time of variation of the electric and magnetic fields ensures that the calculations of the electron motion and the fields are self-consistent.

The particle method is used to model the space–time distribution of the electrons. An explicit ''cross-shaped'' difference scheme is used to find the numerical solution of the Maxwell equations.

RESULTS AND ANALYSIS

Calculations made for the parameters $A_f=10^{-1}$–10^{-3} and $r_0=20$–5 μm show that most of the electrons are trapped by the electric field in a region of characteristic size ~ 1 μm near their surface of generation. The highest-energy electrons escape from this region and then move back toward the surface of the target with a helical motion. Some of them reach this surface where they are absorbed.

As a result of the nonuniform (mainly along z) electron motion, an electromagnetic wave is generated. All the prerequisites of dipole radiation are present in our case, and the

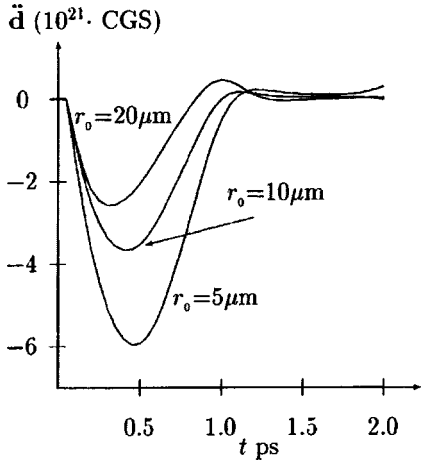

FIG. 1. Time dependence of the second derivative of the dipole moment for various radii of the laser radiation spot for $A_f=0.01$.

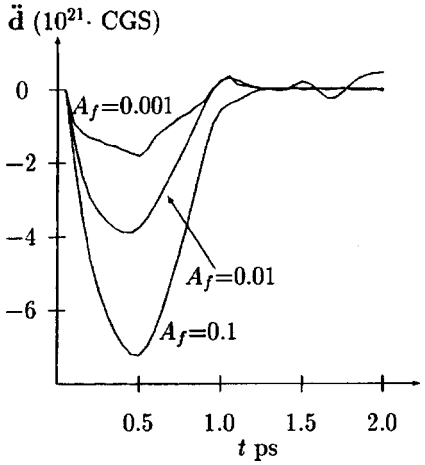

FIG. 2. Second derivative of the dipole moment assuming various laser energy conversion efficiencies for $r_0=10$ μm.

parameters of the outgoing electromagnetic wave can be determined by calculating the time dependence of the second derivative of the dipole moment with respect to time $\ddot{\mathbf{d}}$. The dipole radiation power is given by

$$I=\frac{2}{3c^3}\,\ddot{\mathbf{d}}^2, \quad \ddot{\mathbf{d}}^2\left(\frac{d}{dt}\int j_z dV\right)^2. \tag{4}$$

The fields **E** and **H** at the observation point at distance R are related to the dipole moment by the well-known relations[4]

$$\mathbf{H}=\frac{1}{c^2R}\,\ddot{\mathbf{d}}\times\mathbf{n}, \quad \mathbf{E}=\frac{1}{c^2R}[(\ddot{\mathbf{d}}\times\mathbf{n})\times\mathbf{n}]. \tag{5}$$

Here **n** is the unit vector directed from the center of the target to the observation point.

Figures 1 and 2 display the second derivative of the dipole moment of the fast electrons as a function of time for various values of the parameters r_0 and A_f. The calculations made using the PM2D program show that the efficiency of conversion of the laser radiation into an electromagnetic wave may reach $K_{\max}=I_{\max}/P_{\max}\approx 10^{-5}$ for $r_0=10$ μm and $A_f=0.1$, and also for $r_0=5$ μm and $A_f=0.01$, which corresponds to conversion of fast electron energy into electromagnetic pulse energy with efficiencies $\eta=K/A_f\approx 10^{-4}$–$10^{-3}$.

CONCLUSIONS

Calculations made using the PM2D program have shown that fast electron energy may be converted into subpicosecond electromagnetic pulses with an efficiency of 10^{-3}–10^{-4} when the intensity of the ultrashort laser radiation on the target is 10^{16}–10^{17} W/cm^2.

The authors are grateful to the MNTTs for financing this work under ISTC Project No. 107-94.

[1] A. Rousse, J. P. Geindre, P. Audebert *et al.*, Phys. Rev. E **50**, 2200 (1994).
[2] J. Dunn, B. K. F. Young, A. K. Hankla *et al.*, *Laser Interaction and Related Plasma Phenomena*, edited by Sadao Nakai and George H. Miley, in *AIP Conference Proceedings*, Vol. 369 (AIP Press, New York, 1996), pp. 652–659.
[3] A. L. Zapysov, V. G. Borodin, V. A. Lykov *et al.*, Book of Abstracts of 13th International Conference on Laser Interaction and Related Plasma Phenomena, Monterey, CA, 1997.
[4] L. D. Landau and E. M. Lifshitz, *The Classical Theory of Fields*, 2nd. ed. (Pergamon Press, Oxford, 1971) [Russ. original, Fizmatgiz, Moscow (1960), 213 pp.].

Translated by R. M. Durham

Excitation of the 6^3P_1 atomic level of mercury by pumping a mixture of mercury vapor and argon with a pulse-periodic nanosecond discharge

L. M. Vasilyak, A. V. Krasnochub, M. E. Kuz'menko, and S. V. Kostyuchenko

Moscow Physicotechnical Institute
(Submitted July 21, 1997)
Pis'ma Zh. Tekh. Fiz. **24**, 89–92 (March 12, 1998)

An experimental investigation was made of a pulse-periodic nanosecond discharge in a mixture of mercury vapor and argon. It is shown that the concentration of mercury atoms in the 6^3P_1 state is around 50% of the total concentration.
[S1063-7850(98)01703-0]

A low-pressure arc discharge in mercury–argon mixtures is an efficient source for conversion of energy into radiation on resonant lines of the mercury atom at 185 nm ($6^1P_1-6^1S_0$) and 254 nm ($6^3P_1-6^1S_0$). The transition to a dynamic microsecond-pulse discharge in these mixtures can enhance the output efficiency of the ultraviolet radiation.[1–3] We investigated a nanosecond pulse discharge in the form of a high-speed ionization wave in a mixture of mercury vapor and argon.[4]

The discharge was ignited in a cylindrical quartz tube with an inner diameter of 13.5 mm and an interelectrode gap of 77 cm. The argon pressure under normal conditions was 3 Torr. The mercury pressure was equal to the saturated vapor pressure at the temperature of a cold point in the discharge tube which was created by a cooling system. The discharge tube was surrounded by a grounded metal screen with an inner diameter of 40 mm. The impedance of the discharge circuit, taking the plasma conductivity to be the same as that of a metal, was 60.5 Ω. The discharge cell was connected into a gap in a coaxial line with a wave impedance of 50 Ω.

A pulse-periodic discharge was excited by variable-polarity pulses having amplitude 15.9 kV, rise time 28 ns, and half-width 82 ns in positive polarity, and 18.5 kV, 12 ns, and 61 ns, respectively, in negative polarity. The measurements were made at a pulse repetition frequency of 330 Hz. After passing through the discharge cell, the pulses were absorbed by the 50 Ω load. As a result of the inerradicable mismatch between the cell and the line, some of the incident pulse is reflected back into the line. Because of the design characteristics, this part of the pulse is reflected from the pulse generator and arrives at the discharge cell 640 ns after the initial pulse. The energy absorbed in the discharge is determined using oscilloscope traces from return-current shunts by a method described in Ref. 5, with allowance for the incident and retroreflected pulse. The average discharge electrical power is 30 ± 6 W.

An MUM-1 monochromator, a FÉU-100 photomultiplier, and a Tektronix TDS-640A (500 Hz) oscilloscope were used to study the temporal dynamics of the intensity of the 254 nm line with 3 ns time resolution. The linearity of the FÉU-100 photomultiplier under pulsed loading was checked separately.[6]

The average radiation power in the range 210–280 nm was measured with an F29 photocell. The radiation power on the 254 nm line was determined with allowance for the measured relative intensity of the spectral lines and the spectral sensitivity of the F29 photocell.

The peak radiation power reconstructed from the oscilloscope traces was ≈800 W. Figure 1 shows typical traces from the return-current shunt and the photomultiplier at a cold-point temperature of 40 °C (mercury vapor pressure 6 mTorr).

For the instantaneous radiation power we can write $P(t)=A_{\text{eff}}\times N_a\times\hbar\omega$ (Ref. 7), where A_{eff} is the effective probability of emission of radiation from the plasma, N_a is the number of atoms in the 6^3P_1 state, and $\hbar\omega$ is the photon energy. The effective probability for emission of radiation is $A_{\text{eff}}\leqslant A_{\text{rad}}$, where $A_{\text{rad}}=1/\tau_{\text{rad}}=8.3\times10^6\ \text{s}^{-1}$ (Ref. 8) is the probability of emission of a photon by an isolated atom. As a result of filling of the 6^3P_1 by electron impact from the ground state, and also from the $6^3P_{0.2}$ levels, and radiative transitions from higher levels, we find $1/A_{\text{eff}}\leqslant\tau$, where τ is the decay time for the 254 nm radiation intensity determined from the oscilloscope traces using the approximation $I=I_0\exp(-(t-t_0)/\tau)$. We can then write $1/\tau_{\text{rad}}>A_{\text{eff}}\geqslant1/\tau$.

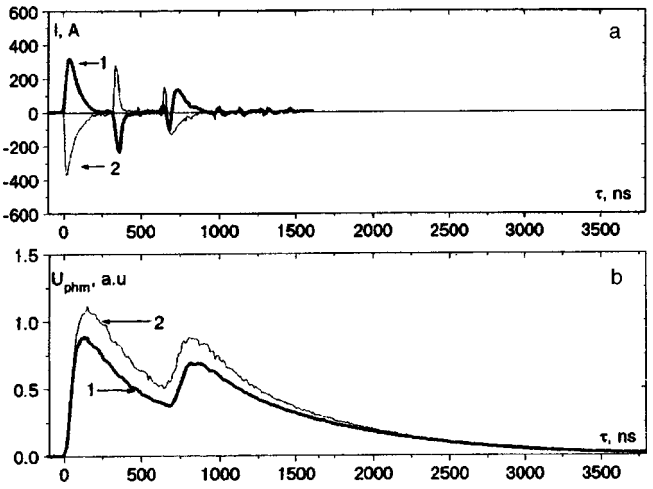

FIG. 1. Oscilloscope traces: a—from return-current shunt; b—photomultiplier signals. *1*—positive pulses and *2*—negative pulses.

This gives $P(t)/(A_{\text{rad}}\hbar\omega V) < n_a \leqslant (P(t)\tau)/(\hbar\omega V)$, where n_a is the concentration of atoms in the 6^3P_1 state averaged over the discharge cross section and V is the volume of the discharge tube.

It was found in Ref. 6 that in a cw discharge at a mercury vapor pressure of 7 mTorr, the concentration of atoms in the 6^3P_1 state averaged over the cross section of the discharge tube was 2.1×10^{11} cm^{-3}, which is approximately 0.1% of the total number of mercury atoms in the discharge. The diameter of the discharge tube was 36 mm, the argon pressure was 4 Torr, and the discharge current was 0.45 A. In our case, at a mercury pressure of 6 mTorr, n_a is between 3×10^{12} and 7×10^{12} cm^{-3}, which is 2–5% of the total number of mercury atoms in the discharge. As the mercury vapor pressure decreases, the peak radiation power on the 254 nm line increases in a pulse-periodic discharge. At 1.4 mTorr, n_a is between 5×10^{12} and 2×10^{13} cm^{-3}, i.e., 10–50% of the total number of mercury atoms in the discharge.

To sum up, by using a pulsed rather than a cw discharge at the same mercury vapor pressure, we succeeded in increasing the population of the resonant state of the mercury atom by more than a factor of 10. It was shown that pulse-periodic discharge conditions exist for which the fraction of the population of the 6^3P_1 mercury atomic state accounts for tens of percent of the total number of mercury atoms in the discharge. In this case, the ultraviolet pulse power is 1 kW and the average electrical discharge power is 30 ± 6 W.

[1] V. M. Milenin and N. A. Timofeev, Zh. Tekh. Fiz. **48**, 2060 (1978) [Sov. Phys. Tech. Phys. **23**, 1175 (1978)].
[2] V. M. Milenin and N. A. Timofeev, Svetotekhnika **4**, 6 (1981).
[3] V. M. Milenin, G. Yu. Panasyuk, and N. A. Timofeev, Fiz. Plazmy **12**, 447 (1986) [Sov. J. Plasma Phys. **12**, 258 (1986)].
[4] L. M. Vasilyak, S. V. Kostyuchenko, N. N. Kudryavtsev, and I. V. Filyugin, Usp. Fiz. Nauk **164**, 263 (1994).
[5] É. I. Asinovskiĭ, L. M. Vasilyak, and A. V. Kirillin, Teplofiz. Vys. Temp. **13**(1), 40 (1975).
[6] V. V. Balabanov, L. M. Vasilyak, and A. V. Krasnochub, Prib. Tekh. Eksp. **3**, 127 (1997).
[7] F. A. Uvarov and V. A. Fabrikant, Opt. Spektrosk. **18**, 562 (1965) [Opt. Spectrosc. **18**, 323 (1965)].
[8] V. S. Egorov, V. A. Tolmachev, and A. N. Klyucharev, in *Handbook of Constants of Elementary Processes Involving Atoms, Ions, Electrons, and Photons*, edited by G. A. Zhiglinskov, [in Russian], St. Petersburg University Press, St. Petersburg (1994), 336 pp.

Translated by R. M. Durham

Direct bonding of silicon wafers with a diffusion layer

V. B. Voronkov, E. G. Guk, V. A. Kozlov, and V. B. Shuman

A. F. Ioffe Physicotechnical Institute, Russian Academy of Sciences, St. Petersburg
(Submitted October 10, 1997)
Pis'ma Zh. Tekh. Fiz. **24**, 1–5 (March 26, 1998)

The possibility of solid-phase direct bonding of silicon wafers having p^+- or n^+-type diffusion layers with a high surface dopant concentration has been demonstrated for the first time.
 [S1063-7850(98)01803-5]

Solid-phase direct bonding of semiconductor wafers (known in the English-language literature as direct wafer bonding—DWB) was proposed comparatively recently[1,2] but is already widely used in microelectronics, optoelectronics, and power engineering alongside conventional methods.[3] The most important requirement for this method is that the surface of the wafers should have a low mean-square level of microroughness so that the bonded wafers can be brought into ''optical' contact.[3,4] At present, direct bonding is used to join pure polished silicon wafers with different resistivities or different types of conductivity to form p^+-n, n^+-n, and p^+-p junctions, and also to join ion-implanted wafers. However, although ion implantation conserves the surface quality of the wafers, it is frequently unacceptable because of the complex equipment required and because in many cases, adequate layer thicknesses cannot be achieved with a high degree of doping. The range of application of direct wafer bonding could be extended if it were possible to bond wafers having diffusion layers with a high level of shallow impurity doping. For instance, direct bonding could be used to fabricate a solar cell structure with vertical $p-n$ junctions,[5] where separate p^*nn^* or n^*pp^* must be joined consecutively. In this case, a high dopant concentration in required in the n^+ and p^+ layers to ensure Ohmic contact with the low intermediate resistance. However, since the surface of the silicon wafers after diffusion is not of sufficiently high quality, this aspect requires special investigations. In Ref. 6, for instance, the silicon wafers used for bonding had a p^+-n junction with a doping depth of 100 μm after diffusion of Ga (in an inert atmosphere) or after codiffusion of B and Al (in air). After diffusion, these wafers were mechanically polished because of the surface erosion. As a result, only the Ga-diffused wafers could be successfully bonded. The surface polishing (which has the obvious disadvantage that it removes the layer with the highest dopant concentration) after diffusion of boron and aluminum created microroughness which prevented the wafers from bonding. This microroughness was possibly caused by the presence of vacancy complexes. Thus, this was not the solution to the problem.

The present study aimed to investigate direct bonding of wafers having a diffusion p^+- or n^+-layer with a high surface dopant concentration, formed in an oxidizing medium. To improve the quality of the wafer surfaces prior to bonding, it was suggested that after diffusion, the wafers should be oxidized, followed by removal of the oxide.

Industrial polished $\langle 100\rangle$-oriented $p-$Si wafers of good surface quality, having a diameter of 600 mm and thickness 350 ± 10 μm, were used for bonding. Both sides of the wafers with the resistivity $\rho = 1\ \Omega\cdot$cm were exposed to diffusion in air from a polymer source deposited on the surface[7] having a high boron or phosphorus content, which gave a surface dopant concentration of $\sim 10^{20}$ cm^{-3}. Boron diffusion took place at 1200 °C for 40 min (sample No. 1) or at 1050 °C for 90 min (samples Nos. 2 and 3). Diffusion of phosphorus took place at 850 °C for 40 min (samples Nos. 4 and 5). The depths of the diffusion layers were: $x_1 \sim 3.7$ μm, $x_{2,3}\sim 1.4$ μm, and $x_{4,5}\sim 0.4$ μm. Then, after removing the silicate glass in hydrofluoric acid, samples Nos. 1, 2, and 4 were oxidized in water vapor at 900 °C for 40 min.

The wafers were bonded in pairs: each silicon wafer which had undergone diffusion was bonded with a pure p-type silicon wafer with resistivity $\rho = 0.005\ \Omega\cdot$cm. Directly before bonding, all the wafers were etched in hydrofluoric acid, and this was followed by a standard acid-peroxide washing cycle. At the final stage, the wafers were treated in dilute 2% HF, the surface was then hydrophilized in a NH_4OH:H_2O_2:H_2O (0.05:1:5) solution, and finally rinsed in deionized water with a resistivity ~ 18 M$\Omega\cdot$cm. The wafers were joined and bonded by a technique described in Ref. 8.

The joined wafers were subjected to high-temperature heat treatment in air at 1200 °C for 2h with no external pressure applied.

The continuity of the bond and the presence of ''bubbles'' at the interface was monitored by infrared photometry using a PTU-44 television system. The coordinate resolution over the area was ~ 300 μm and bubbles could be detected when the optical gap between the wafers was $\geqslant 0.25$ μm. After the infrared photometry, the bonded wafers were cut into two halves. On one half, an oblique polished section was prepared at a small angle and after alkaline etching, the quality of the surface was examined under a microscope. On the other half, contacts were deposited by chemical nickel-plating and 4×4 mm squares (assemblies) were cut and the current-voltage characteristic measured. Monitoring the continuity of the bonding for the wafers having a diffusion p^+-layer revealed almost no bubbles for sample No. 1, i.e., total bonding was confirmed, whereas in sample No. 2 bubbles occupied $\sim 10\%$ of the area. For the

control sample which had not been oxidized after the boron diffusion (sample No. 3), bubbles accounted for ~50% of the area. A different result was obtained for the bonding of wafers with a diffusion n^+-layer—for both sample No. 4 which had been oxidized after the diffusion of phosphorus, and the control sample No. 5, bubbles accounted for ~5% of the area.

The current-voltage characteristics of the assemblies were linear. A comparison between the measured resistivities of the assemblies and the calculated value (allowing for the bulk resistivity of the wafers; the resistivity of the contacts was assumed to be low) suggested that an extra resistivity is present at the interface. The fraction of assemblies having the calculated resistivity was 91% for sample No. 1, 85% for sample No. 2, and 40% for the control sample No. 3, which correlates with the estimate made using infrared photometry. For the bonding of wafers with a diffusion n^+-layer, we confined ourselves to infrared photometry, which yielded good results. It should be noted that the correspondence between the resistivity of an assembly and the calculated value does not indicate that no small bubbles are present at the interface since the flow resistance over the diffusion layer is low. However, it should be borne in mind that for many applications, the quality of the interface between highly doped layers is not so important, as for example, for the bonding of uniformly doped wafers with different types of conductivity, since in the first case the $p-n$ junction is located at a distance from the interface equal to the thickness of the diffusion layer, and thus the interface is outside the space charge region.

We note three factors which have helped to achieve a positive result: 1) the diffusion time in the oxidizing atmosphere was much shorter than that in Ref. 6; 2) polishing was not carried out after diffusion as in Ref 6; 3) after diffusion the wafers were oxidized in water vapor followed by removal of the oxide.

To sum up, we have shown for the first time that solid-phase direct bonding of silicon wafers having n^+- or p^+ diffusion layers with a high surface dopant concentration can be implemented without additional polishing of the surface after diffusion.

This work was supported financially by the Russian Fund for Fundamental Research, Grant No. 96-02-17902.

[1] J. B. Lasky, Appl. Phys. Lett. **48**, 78 (1986).
[2] M. Shimbo, K. Furukawa, K. Fukuda, and K. Tanzava, J. Appl. Phys. **50**, 2987 (1986).
[3] S. Bengtsson, J. Electron. Mater. **21**, 841 (1992).
[4] T. Abe, E. F. Steigmeier, W. Hagleiter, and A. J. Allan, Jpn. J. Appl. Phys. **31**, 721 (1992).
[5] E. G. Guk, N. S. Zimogorova, M. Z. Shvarts, and V. B. Shuman, Zh. Tekh. Fiz. **67**(2), 129 (1997) [Tech. Phys. **42**, 238 (1977)].
[6] V. A. Kozlov, V. K. Eremin, I. L. Shulpina, V. B. Voronkov, A. M. Ivanov, V. V. Eliseyev, and V. V. Chibirkin, in *High Purity Silicon IV*, edited by C. L. Claeys, P. Rai-Choudhury, P. Stallhofer, and J. M. Maurits (Electrochemical Society Ser., Pennington, 1996) PV 96–13, pp. 369–378.
[7] E. G. Guk, A. V. El'tsov, V. B. Shuman, and T. A. Yurre, Photoresists—Diffusants in Semiconductor Technology [in Russian], Nauka, Leningrad (1984).
[8] I. V. Grekhov, V. A. Kozlov, V. A. Volle, and V. B. Voronkov, *Best of Soviet Semiconductor Physics and Technology 1989–1990*, edited by M. Levinstein and M. Shur (World Scientific, Singapore 1995), pp. 597–599.

Translated by R. M. Durham

Identification of self-organizing structures by the numerical simulation of laminar three-dimensional flow around a crater on a plane by a flow of viscous incompressible fluid

S. A. Isaev, A. I. Leont'ev, D. P. Frolov, and V. B. Kharchenko

Academy of Civil Aviation, St. Petersburg; N. É. Bauman State Technical University, Moscow
(Submitted October 8, 1997)
Pis'ma Zh. Tekh. Fiz. **24**, 6–12 (March 26, 1998)

Three-dimensional steady-state vortex structures which undergo self-organization during flow around a deep spherical crater on a plane are analyzed by using a factorized finite-volume method to solve the Navier–Stokes equations in a simplified approach based on an analytic definition of metric coefficients. © *1998 American Institute of Physics.*
[S1063-7850(98)01903-X]

The problem of vorticity intensification of heat and mass exchange processes caused by the generation of self-organizing vortex structures when a low-velocity flux flows around ordered curvilinear reliefs, especially spherical craters, mainly originates from ten years of experimental research (G. I. Kiknadze, M. I. Rabinovich, M. A. Gotovskiĭ, V. I. Terekhov, A. P. Kozlov *et al.*). The spout-like vortices observed in Refs. 1 and 2 near surfaces covered with spherical craters or containing a hemispherical crater on one of the channel walls, were analyzed systematically in Refs. 3 and 4 by making a detailed analysis the nonsteady-state mechanism of vortex formation in a isolated crater under conditions of advanced turbulent flow. It was emphasized in Ref. 5 that the organization of large-scale vortex structures in the boundary layer of turbulent flow near a surface covered with spherical craters can not only intensify the heat and mass exchange processes, but can also reduce the losses caused by the fluid motion, especially by reducing the frictional resistance. However, doubts were cast on this statement in Ref. 6 because of inadequate experimental confirmation. In addition, this method of vorticity intensification of heat and mass exchange processes is also associated with an artificial transition of the boundary-layer flow to turbulent. On the whole, the experimental approaches to solving this problem revealed various difficulties in estimating the complex vortex flow pattern and yielded ambiguous conclusions as to the effectiveness of this type of vorticity intensification. This indicates that there is a need for a more detailed controlling mechanism for the generation of vortices induced by crater topologies, based on using numerical simulation methods as tools for a detailed diagnosis of the flow field, identifying its most important features.

The last five years have seen the systematic development of numerical simulations of large-scale vortex structures formed in the boundary layer of laminar and turbulent flows of an incompressible viscous fluid near a spherical crater on a plane.[7–12] The investigations whose results are published in Refs. 7 and 8 were carried out using a simplified formulation assuming symmetric detached flow relative to the geometric plane of symmetry passing through the center of a shallow crater. In Ref. 9 a similar approach was used to analyze the vortex structure of detached flow in a deep crater. Results of computer visualization of vortex flow near a crater, including nonsteady-state evolution of the process and also blocking of the flow in a thin layer adjacent to the wall, were analyzed in Refs. 10–12.

The present numerical simulation focuses on a detailed analysis of the controlling mechanism of vortex generation in the boundary layer of an incompressible viscous fluid near an isolated spherical concavity on a smooth wall and identifying the three-dimensional vortex structures by computer visualization of the flow based on observing the tracks of labeled fluid particles. The concept of comparing the numerical results with the experimental data[2] is implemented systematically, with conditions close to those of a physical experiment reproduced in the calculations. An analysis is made of deep spherical craters with rounded edges for which stable laminar flow is achieved with the formation of a developed detached zone.

Unlike previous approaches[7–12] to the numerical simulation of flow around a crater on a plane, which used nonorthogonal meshes matched with the curvilinear surface with mesh points positioned in planes perpendicular and parallel to the direction of the incoming flux and accumulations near the walls and the shear layer zone, here we use a cylindrical mesh matched with the washed surface (Fig. 1a). This allows the cell density within the detached zone to be increased substantially (by a factor of five or more). In addition, in order to avoid the problems associated with the interpolation of metric coefficients, we use a simplified approach based on defining an analytic metric. In all other details, the methodology used in the present analysis is the same as that described in Ref. 8. A system of Navier–Stokes equations written in natural variables for the Cartesian velocity components is solved using an implicit finite-volume method using the concept of splitting into physical processes. A velocity profile corresponding to a Polhausen profile for a boundary layer of thickness equal to the depth of the crater is set at the entry boundary of the calculation region. Soft boundary conditions (conditions for continuation of the so-

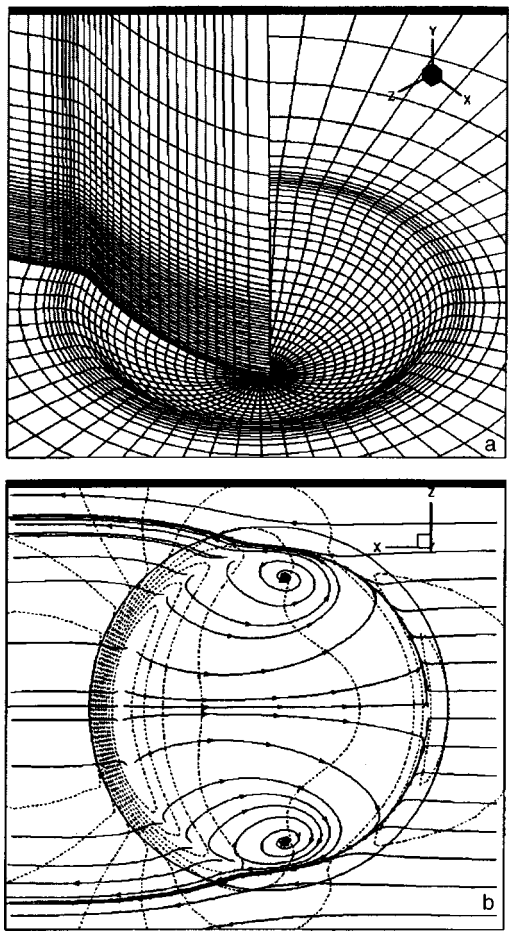

FIG. 1. a—Portion of mesh used to calculate flow around a crater of depth 0.22 and radius of curvature 0.09. The Reynolds number of the incoming flow is 2500; b–liquid flow pattern over the surface of the crater (projected on the $x-z$ plane) with isobars with a spacing of 0.002 shown by the dashed lines (range of variation in pressure relative to twice the velocity head between -0.004 and -0.018.

lution from the inner points to the boundary of the region) are set at the exit boundaries. Attachment conditions are satisfied at the wall. The velocity of the incoming flux outside the boundary layer and the crater diameter are used to convert to dimensionless parameters. Calculations of the steady-state flow around a crater on a plane are made using a mesh containing $42\times50\times61$ cells. The depth of the crater is taken as 0.22 and the radius of curvature of the sharp edge as 0.9. The Reynolds number corresponds to the experimental conditions in Ref. 2 and is taken as 2500.

Figures 1 and 2 show some of the numerical results obtained using the TECPLOT program for computer visualization of three-dimensional fields.

On analyzing the liquid flow pattern (Fig. 1b) in the layer near the surface of the crater, we can identify a general trend (for the numerical and physical experiments) in the flow behavior in the detached zone whereby two large-scale vortex cells are formed within the crater. A characteristic feature of the cells is that there are two foci in the peripheral part of the crater—centers of fluid runoff zones. However, the hypothesis put forward in Ref. 2 that all the fluid is trapped in the crater and rolled into a three-dimensional twisted jet is not completely accurate. Quite clearly, only that part of the liquid in the small zone near the focus initiates the jet. On the whole, the flow over the surface of the crater resembles the detached flow around a two-dimensional trench although the vortex flow in the crater has a well-defined three-dimensional nature.

The trajectory patterns of liquid particles introduced near the foci and at the points in the crater space observed in the calculations ($x=0$, $y=0.1$, $z=\pm0.1$), shown in Fig. 2, revealed the existence of stable structural elements. They confirmed the almost obvious assumption[2] that there is a horseshoe-shaped vortex line connecting the foci about

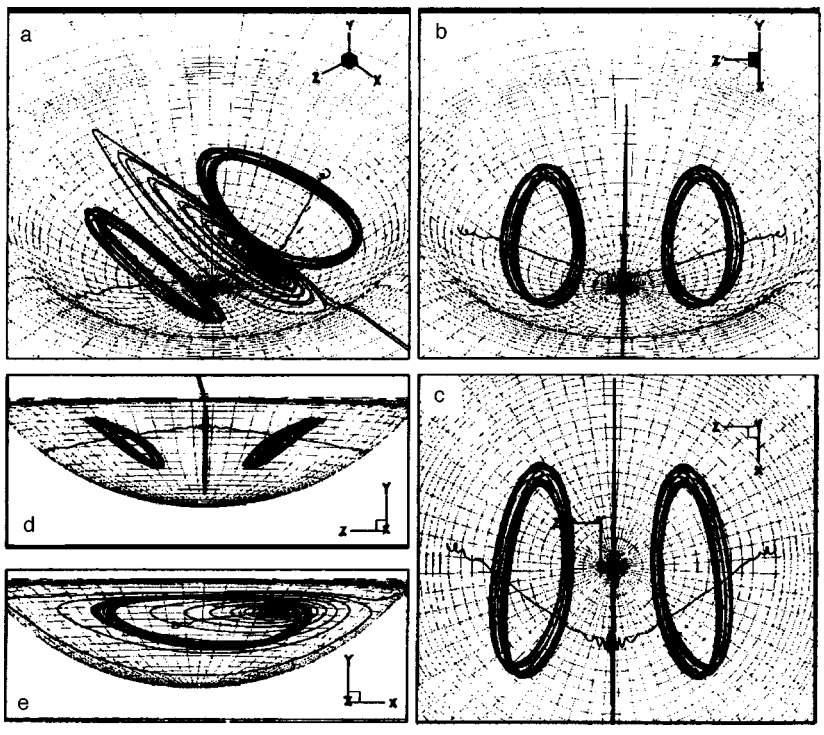

FIG. 2. Axonometric (a, b) and planar (c, d, e) projections of the three-dimensional patterns of vortex structures illustrated by the trajectories of liquid particles ejected near the foci and the points determined in the numerical simulation ($x=0$, $y=0.1$, $z=\pm0.1$).

which untwisting spiral lines of flow develop. It was noted in Ref. 12 that a twisted jet stream is established in a crater and is responsible for mass transfer from the peripheral part of the crater to the geometric plane of symmetry (relative to the direction of the incoming flux). The mass transfer clearly leads to the existence of a source in the plane of symmetry, and forms a jet which flows out of the crater in this region.

The most interesting result of the numerical calculations is the two vortex toroidal rings observed in the crater. These comprise a set of trajectories of only two particles ejected symmetrically relative to the center of the crater and shown in the time interval 0...1000 (dimensionless units). These symmetric stable rings whose axes are oriented along the normal to the surface of the crater are without doubt the unknown elements which in many respects determine the mechanism for vorticity intensification of heat and mass exchange.

This work was financed by the Russian Fund for Fundamental Research, Project No. 96-02-16356.

[1] G. I. Kiknadze and Yu. K. Krasnov, Dokl. Akad. Nauk SSSR **290**, 1315 (1986) [Sov. Phys. Dokl. **31**, 799 (1986)].
[2] P. R. Gromov, A. B. Zobnin, M. I. Rabinovich *et al.*, Pis'ma Zh. Tekh. Fiz. **12**, 1323 (1986) [Sov. Phys. Tech. Phys. **12**, 547 (1986)].
[3] V. S. Kesarev and A. P. Kozlov, Vestn. Mosk. Gos. Tekh. Univ. Ser. Mashinostr. No. 1, 106 (1993).
[4] V. I. Terekhov, S. V. Kalinina, and Yu. M. Mshvidobadze, Russ. J. Eng. Thermophys. **5**, 11 (1995).
[5] V. N. Afanas'ev, V. Yu. Veselkin, A. I. Leont'ev *et al.*, Preprint No. 2–91 Part 1 [in Russian], N. É. Bauman State Technical University, Moscow.
[6] G. A. Dreĭtser, in *Proceedings of the Third Minsk International Forum on Heat and Mass Exchange, MMF–96*, Minsk, 1996, Vol. 10, *Intensification of Heat and Mass Exchange*, Part 1, [in Russian], pp. 26–39.
[7] V. N. Afanasiev, Ya. P. Chudnovsky, S. A. Isaev *et al.*, in *Proceedings of the Fifth International Symposium on Refined Flow Modelling and Turbulent Measurement*, Paris, 1993. pp. 391–398.
[8] S. A. Isaev, V. B. Kharchenko, and Ya. P. Chudnovskiĭ, Inzh.-Fiz. Zh. **67**, 373 (1994).
[9] S. A. Isaev and Ya. P. Chudnovskiĭ, Abstracts of Papers presented at the First National Conference on Heat Exchange, MÉI, Moscow, 1994, Vol. 8, *Intensification of Heat Exchange* [in Russian], pp. 80–85.
[10] S. A. Isaev, in *Proceedings of the International Symposium on Heat Transfer Enhancement in Power Machinery*, Moscow, 1995, Part 2, pp. 153–156.
[11] S. A. Isaev, A. I. Leont'ev, and A. E. Usachev, in *Proceedings of the Third Minsk International Forum on Heat and Mass Exchange, MMF–96*, Minsk, 1996, Vol. 1, Convective Heat and Mass Exchange, Part 1, [in Russian], pp. 33–36.
[12] S. A. Isaev, A. I. Leont'ev, and A. E. Usachev, Izv. Ross. Akad. Nauk Ser. Énerg. No. 4, 140 (1996).

Translated by R. M. Durham

Investigation of the laws governing the propagation of pyrolysis and combustion waves along a laser beam in propane

G. I. Kozlov

Institute of Problems in Mechanics, Russian Academy of Sciences, Moscow
(Submitted October 21, 1997)
Pis'ma Zh. Tekh. Fiz. **24**, 13–17 (March 26, 1998)

It was demonstrated experimentally that the preliminary conversion of a fuel mixture may appreciably accelerate the combustion reaction. © *1998 American Institute of Physics.*
[S1063-7850(98)02003-5]

The tendency toward higher combustion rates coupled with the relatively low reactivity of natural hydrocarbon fuels (methane, propane, and so on) generally has the result that in modern combustion chambers, the combustion process does not go to completion. In consequence, numerous incomplete combustion products—harmful impurities, including carbon monoxide—are ejected into the atmosphere.

A promising solution to this problem involves changing over to new principles for the ignition of hydrocarbon fuels, based on preliminary conversion of the fuel mixture in order to enhance its reactivity. As the first stage of the research, it is important to demonstrate that this approach to solving the problem is possible in principle. Thus, the present paper reports results of preliminary experiments to study the propagation velocities of pyrolysis and combustion waves in a laser beam and attempts to show that for the case of propane, preliminary conversion of a fuel mixture may appreciably accelerate the combustion reactions.

The experiments were carried out using a system based on a 5 kW cw gas-discharge CO_2 laser with diffusion cooling.[1] A laser beam with a divergence of 3×10^{-3} rad was focused by a potassium chloride lens having a focal length of 110 cm and was passed through a salt entry window into a 51 cm long horizontal quartz reaction tube with an inner diameter of 7.1 cm, so that the laser beam propagated along the axis of the tube. The beam diameter at the entry window was 3.4 cm and the diameter of the focusing spot did not exceed 0.6 cm. The focusing region could be moved along the axis of the tube by using the lens, but in these experiments the distance between the focus and the window was kept constant at 32.0 cm. The other end of the chamber was closed by a flange which had pumping and gas admission apertures.

After the reaction tube had been filled with the mixture to a given pressure, the laser shutter was opened by switching on a magnet and the laser beam initiated an optical deflagration flash, followed by propagation of the optical deflagration wavefront along the beam. The process was recorded by a video camera so that the laws governing the propagation of the front could be determined for various pressures and compositions of the gas mixture.

The first stage involved studying the initiation of a pyrolysis wave and its propagation in propane. Figure 1 shows photographs at various times of a pyrolysis wave propagating along the laser beam at a propane pressure of 25 Torr. An analysis of the photographs reveals that the process is initiated at the focus, i.e., a pyrolysis wave forms in which the propane undergoes an endothermic dissociation reaction. After ''ignition,'' pyrolysis waves propagate along the beam in both directions from the focus, which indicates that propane and its pyrolysis products are partially transparent to the 10.6 μm laser radiation. Of particular interest was the velocity of the wavefront propagating in the direction opposite to the beam. By analyzing the video frames, it was possible to plot

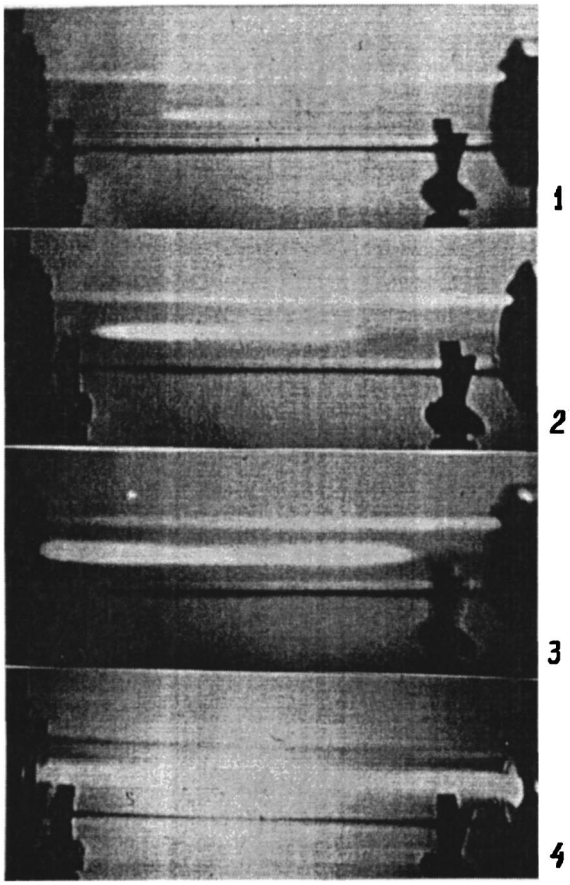

FIG. 1. ideo frame photographs of the propagation of an optical deflagration wavefront along a laser beam in propane at various times: *1*—0.08, *2*—0.24, *3*—0.64, and *4*—0.80 s.

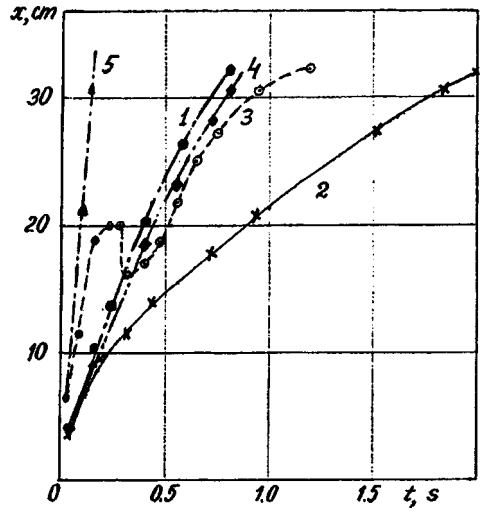

FIG. 2. Position of the pyrolysis wavefront at various times: *1*—propane (25 Torr), *2*—propane (25 Torr)+helium (100 Torr), *3*—propane (100 Torr), *4*—propane (25 Torr)+air (125 Torr), and *5*—propane (25 Torr)+air (125 Torr) with preliminary pyrolysis of the propane.

graphs showing the position of the front at various times. The results of these measurements are plotted in Fig. 2 which indicates that at this propane pressure the velocity of the pyrolysis wavefront depends weakly on the laser radiation intensity, which decreased almost by a factor of 30 between the focus and the entry window although the velocity of the front was only approximately halved.

When 100 Torr of helium was added to the propane, the velocity of the front decreased appreciably, as can be seen from Fig. 2. This drop in velocity is undoubtedly caused by the fact that helium is a buffer gas and thus substantially slows the rate of propane heating in the laser beam and the rate of dissociation of the propane molecules. It should also be noted that in this case, the velocity of the front depends more strongly on the intensity. Whereas in the focusing region where the intensity was 1.8×10^4 W/cm^2, the velocity was 46 cm/s, near the exit window, where the intensity was only 5×10^2 W/cm^2, the velocity did not exceed 10 cm/s.

Conversely, when the propane pressure was increased from 25 to 100 Torr and above, the propagation velocity of the front increased appreciably to 1.3 m/s near the focusing region. However, the front then exhibited unusual behavior, where it propagated more slowly, stopped, and even withdrew slightly back to the focus. After a few frames, the process appeared to recover and the pyrolysis wavefront continued to propagate along the beam. This characteristic behavior of the front propagation (see Fig. 2), which showed good reproducibility, may be caused by partial shielding of the process by intermediate products of the propane pyrolysis which either formed along the beam path ahead of the wavefront or reached the entry window much earlier than the pyrolysis wave as a result of convective fluxes. A convective flux generated by heating of the gas in the laser beam could be clearly seen on the video cameras as a result of the carbon particles. This flux rose from the beam zone, reached the walls of the tube, and then spread in all directions. The carbon particles contained in the convective flux were deposited on the cold walls of the chamber.

At the second stage of the investigations, 125 Torr of air was added to 25 Torr of propane. In this case, it was hoped to record accelerated propagation of the front along the laser beam caused by an additional release of energy as a result of the propane oxidation reaction in the front. However, the experiment revealed no appreciable changes in the velocity and laws governing the propagation of the front in this case of a thermal-oxidizing pyrolysis wave (see Fig. 2, curve *4*). The accelerating effect of the additional energy release was most likely compensated by the buffering effect of the nitrogen in the air.

The third stage of the investigations involved combining the processes. Consistent with this idea, propane in the reaction tube at a pressure of 25 Torr was preliminarily converted to a pyrolysis wave propagating along the laser beam, and then as in the previous case, 125 Torr of air was added to the pyrolysis products. This produced a fantastic result! As can be seen from Fig. 2, curve *5*, the average velocity of propagation of the combustion wavefront along the laser beam increased by a factor of 6–8! Video photography showed that a deflagration wave was generated in one frame and in the next frame or the one after, its front reached the entry window. The wavefront then propagated not only within the beam, as in the previous cases, but also over the entire cross section of the tube.

To conclude, preliminary pyrolysis of the propane appreciably increases the reactivity of the fuel. This yields the fundamental conclusion that further intensification of combustion processes is best achieved by adopting new principles for the ignition of hydrocarbons based on preliminary conversion of the fuel. More detailed results and a theoretical interpretation will be presented in later publications.

Finally, the author would like to thank V. A. Lakutin for assistance with this work.

[1] G. I. Kozlov, V. A. Kuznetsov, and A. D. Sokurenko, Pis'ma Zh. Tekh. Fiz. **17**(11), 25 (1991) [Sov. Tech. Phys. Lett. **17**, 794 (1991)].

Translated by R. M. Durham

Infrared spectroscopy of a silicon surface bombarded by nitrogen ions

V. I. Bachurin, P. A. Lepshin, V. K. Smirnov, and A. B. Churilov

Institute of Microelectronics, Russian Academy of Sciences, Yaroslavl
(Submitted September 23, 1997)
Pis'ma Zh. Tekh. Fiz. **24**, 18–23 (March 26, 1998)

Transmission Fourier-transform infrared spectroscopy was used to study the formation of a ripple topology on a silicon surface bombarded by nitrogen ions, together with the formation of silicon nitride, the evolution of its composition and structure. For the first time, an attempt is made to study the evolution of the formation of a ripple topology on the surface of silicon by analyzing the main spectral characteristics (amplitude, position, and profile) of the infrared absorption bands. It is shown that the change in the profile of the characteristic absorption band and the position of its peak correlate with the characteristics of formation of the ripples on the silicon surface. It is demonstrated that infrared transmission spectroscopy can be used to study surface structuring processes for semiconductors bombarded by ions of chemically active elements. © *1998 American Institute of Physics.* [S1063-7850(98)02103-X]

It is known that when ions are obliquely incident on the surface of various materials, a periodic ripple topology may be formed. This process has been observed in the interaction between rare-gas, oxygen, nitrogen, and cesium ions with surfaces of semiconductors, metals, and amorphous materials.[1–5] In particular, a periodic structure is formed on the surface of silicon bombarded by obliquely incident oxygen and nitrogen ions at an angle from the normal to the surface of $\theta = 20-60°$ (Refs. 5–7). Although a ripple microtopology has been studied for quite some time, its nature is still unclear and the fundamental physical effects responsible for its formation have not been investigated.

Here transmission Fourier-transform infrared spectroscopy was used to study the modification of the surface, including the formation of a ripple microtopology on a silicon surface bombarded by obliquely incident nitrogen ions.

The samples were prepared in ultrahigh vacuum (10^{-9} Torr) using a Perkin–Elmer PH1 660 scanning electron Auger spectrometer with the angle of incidence $\theta = 30°$, N_2^+ ion energy 8 keV, and current density 3×10^{15} ion/cm^2. The infrared transmission spectra were measured for several series of 15 samples bombarded with doses between 8×10^{16} and 5×10^{18} ion/cm^2. The ripple formation process was monitored in situ using the silicon and nitrogen Auger signal. Figure 1 shows typical dependences of the Si Auger electron current (I_{Si}) as a function of the radiation dose (ϕ) which indicates that steady-state sputtering is established above $\phi \cong 1.5 \times 10^{17}$ ion/cm^2. The Si Auger electron current remains constant up to $\phi \cong 6 \times 10^{17}$ ion/cm^2. In this case, the silicon and nitrogen concentrations in the surface layer were 57 and 43 at. %, respectively. When the dose is increased from 6×10^{17} to 9×10^{17} ion/cm^2, the current I_{Si} increases by $\sim 10\%$ and then remains almost constant with a further increase in dose. The behavior of $I_{Si}(\phi)$ is determined by the formation of the ripple microtopology[7] and is related to the experimental geometry (Fig. 1). Measurements made with an atomic force microscope were used to determine the linear and angular dimensions of the structure. The local angles of incidence for the ripples were $\sim 50°$ and 10° for the slopes facing the energy analyzer and the primary beam, respectively.

Estimates made using the results of Ref. 7 for the dependence of the concentration ratio on the angle of incidence of the ion beam indicate that the surface layer of the first slope contains 20 at. % nitrogen and 80 at. % silicon. The Si and N content at the surface of the second slope corresponds to silicon nitride Si_3N_4 (Fig. 1).

Measurements of the infrared spectra at room temperature were made using a Bruker IFS-113v Fourier spectrometer in the wave number range 4000–400 cm^{-1} with 4 cm^{-1} resolution.

Figure 2a shows typical infrared transmission spectra obtained for a series of samples. The 1107 cm^{-1} line is attributed to interstitial oxygen in the initial silicon wafers. The infrared transmission spectrum of the silicon substrates was used for comparison to calculate the transmission of the modified surface layer. Sputtering reduced the concentration of interstitial oxygen in the bombarded samples and caused ''bleaching'' of the surface layer near 1107 cm^{-1}. The maximum of the fundamental absorption band attributable to the Si–N bonds lies in the range $\sim 820-850$ cm^{-1}.

An analysis of the infrared transmission spectra reveals that as the radiation dose increases, the profile of the fundamental absorption band changes. In particular, for $\phi \leqslant 5 \times 10^{17}$ ion/cm^2 the fundamental absorption band has a complex structure in which at least another two bands with frequencies near 1000 and 700 cm^{-1} can be identified. In the dose range corresponding to ripple formation, the intensity of these bands decreases appreciably and for $\phi \geqslant 10^{18}$ ion/cm^2, the profile of the fundamental band changes negligibly.

The ripple formation process is accompanied by a change in the position of the fundamental absorption band peak in Fig. 2b. It should be noted that the change in the profile of the spectral absorption band and especially the position of the peak correlates with typical changes in the Si

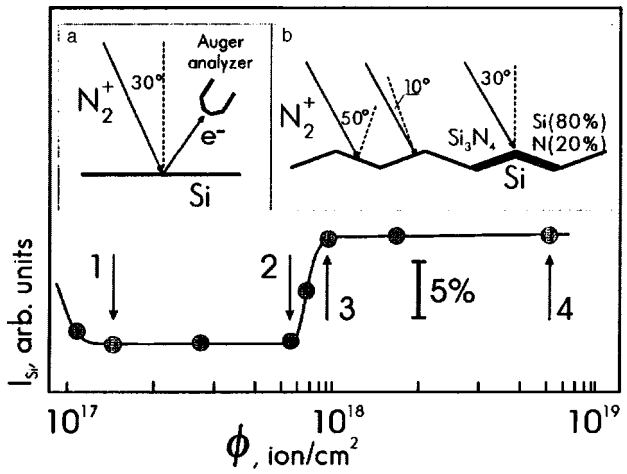

FIG. 1. Auger electron current of silicon versus radiation dose for bombardment of the surface by an 8 keV N_2^+ ion beam. The insets show the experimental geometry at the initial stages of sputtering (a) and after the formation of a microtopology (b). Points *1–4* correspond to the transmission spectra plotted in Fig. 2.

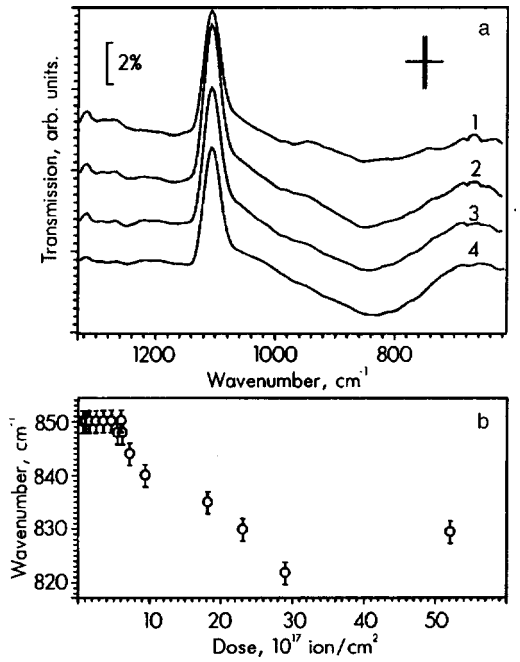

FIG. 2. a—Infrared transmission spectra of a modified surface layer of Si bombarded by 8 keV nitrogen ions at an angle of 30° relative to the normal to the surface at doses: *1*—$\phi=1.6\times10^{17}$ ion/cm^2, *2*—$\phi=5.4\times10^{17}$ ion/cm^2, *3*—$\phi=9.4\times10^{17}$ ion/cm^2, and *4*—$\phi=5.2\times10^{18}$ ion/cm^2; b—spectral position of the fundamental absorption band peak of silicon nitride.

Auger electron current, i.e., with the formation of the microtopology (Fig. 1).

Structural investigations of crystalline silicon nitride (Si_3N_4) and $(SiH_3)_3N$ molecules show that the nitrogen atom is locally bound to three silicon atoms lying in the same plane.[8] A study of amorphous Si_3N_4 by Raman spectroscopy suggested that this planar local neighborhood geometry is also found in the amorphous phase. Four different types of local vibrations of the Si_3N group[9] may be observed in the infrared transmission and Raman spectra. The strongest infrared absorption line is the result of asymmetric, doubly degenerate stretching vibrations in the plane of this Si_3N group with typical frequencies of 800–950 cm^{-1}.

One of the first studies to investigate the infrared absorption spectra of different modifications of Si_3N_4 was reported in Ref. 10. Assuming the fine structure observed in the absorption spectra by these authors,[10] nineteen absorption bands can be assigned to $\alpha-Si_3N_4$ and nine to $\beta-Si_3N_4$ in the range 300–1100 cm^{-1}. As a result of amorphization, local groups of nitrogen and silicon atoms are arbitrarily distorted and their relative positions are altered, which leads to substantial broadening and suppression of absorption bands corresponding to infrared active vibrations. The spectra shown in Fig. 2a correspond to the amorphous phase of silicon nitride formed in the surface layer.[10]

Weak absorption ($\sim$0.5%) near 800 cm^{-1} can be recorded at the initial stages of ion bombardment at doses of 10^{15} ion/cm^2. This implies that the nitrogen ions implanted in the silicon form Si_3N groups. As the dose is increased to levels corresponding to the establishment of steady-state sputtering, the intensity of the absorption bands characteristic of silicon nitride increases, providing evidence of an increased concentration in the surface layer.

The behavior of the absorption band suggests that after steady-state sputtering has been established, regions containing Si_3N_4 in the amorphous and crystalline phases are established in the surface layer. In this case, the terms ''amorphous'' and ''crystalline'' refer to the Si_3 groups and indicate alteration or conservation of the short-range order, respectively. When the local angle of incidence varies, i.e., a ripple topology is formed, conditions are established where amorphous Si_3N_4 forms mainly on one slope of the ripple (angle of incidence close to normal) while the nitrogen concentration on the other slope decreases appreciably (from 43 to 20 at. %). As a result, the contribution of the Si_3N_4 crystalline phase to the total absorption decreases, which leads to a change in the profile and a low-frequency shift of the absorption band from 850 to 830 cm^{-1}.

To sum up, it has been demonstrated that infrared transmission spectroscopy can be used to study the composition and its interrelation with the stages of surface modification by chemically active ion beams. It has been established that when the radiation dose is increased to levels corresponding to the establishment of steady-state sputtering, the intensity of the absorption bands of silicon nitride increases, indicating an increased concentration in the surface layer.

The formation of a ripple topology on the surface of silicon nitride bombarded by nitrogen ions at an angle of 30° from the normal is accompanied by changes in the profile and position of the fundamental absorption line of silicon nitride, which may be caused by an increase in the relative fraction of its amorphous phase.

This work was supported by the Russian Fund for Fundamental Research (Grant No. 96-02-18541).

[1] K. Elst and W. Vandervorst, J. Vac. Sci. Technol. A **12**, 3205 (1994).
[2] A. Karen, Y. Nakagawa, M. Hatada *et al.*, Surf. Interface Anal. **23**, 506 (1995).

[3] J. J. Vajo, R. E. Doty, and E.-H. Cirlin, J. Vac. Sci. Technol. A **14**, 2709 (1996).
[4] D. W. Moon and K. J. Kim, J. Vac. Sci. Technol. A **14**, 2744 (1996).
[5] K. Wittmaak, J. Vac. Sci. Technol. A **8**, 2246 (1990).
[6] V. K. Smirnov, D. A. Kurbatov, E. V. Potapov, and A. V. Zhokhov, Poverkhnost' No. 10, 65 (1993).
[7] V. K. Smirnov, S. A. Krivelevich, P. A. Lepshin, and D. S. Kibalov, Neorg. Mater. (1998), in press.
[8] F. A. Cotton and G. Wilkinson, *Advanced Inorganic Chemistry*, 2nd ed. [Wiley, New York (1966); Mir, Moscow (1969), 592 pp.].
[9] G. Luckovsky, J. Yang, S. S. Chao *et al.*, Phys. Rev. B **28**, 3234 (1983).
[10] Yu. N. Volgin and Yu. I. Ukhanov, Opt. Spektrosk. **38**, 727 (1975) [Opt. Spectrosc. **38**, 412 (1975)].

Translated by R. M. Durham

Energy barriers and trapping centers in silicon metal-insulator-semiconductor structures with samarium and ytterbium oxide insulators

V. A. Rozhkov, A. Yu. Trusova, and I. G. Berezhnoĭ

Samara State University

(Submitted September 12, 1997)
Pis'ma Zh. Tekh. Fiz. **24**, 24–29 (March 26, 1998)

The method of internal photoemission of carriers into the insulator has been used to determine the energy barriers for the electrons at Al–Sm_2O_3 (2.89–2.91 eV), Ni–Sm_2O_3 (3.29–3.33 eV), Si–Sm_2O_3 (2.70–2.72 eV), Al–Yb_2O_3 (2.90–2.92 eV), Ni–Yb_2O_3 (3.30–3.32 eV), and Si–Yb_2O_3 (3.18–3.21 eV) interfaces in silicon metal-insulator-semiconductor (MIS) structures with samarium and ytterbium oxide insulators. The parameters of deep electron traps in samarium and ytterbium oxide were investigated. The energy position of the electron trapping centers, the magnitude and ''centroid'' of the trapped charge, and the ratio of the charge trapped in the insulator to that transmitted by the structure were determined. It is shown that the centroid of the trapped charge is positioned almost at the center of the insulating layer for both structures studied. It was established that in these MIS structures the rare-earth oxide–Si interface is abrupt and contains no extended damaged layer. © *1998 American Institute of Physics.* [S1063-7850(98)02203-4]

Promising insulating materials for discrete devices in semiconductor electronics and integrated-circuit elements include oxides of rare-earth elements. These compounds have been used to develop silicon metal-insulator-semiconductor (MIS) varicaps with high capacitance overlap coefficients and steeply sloping capacitance-voltage characteristics,[1] electrical switching elements with memory,[2] and efficient anti-reflection and passivating coatings for silicon photoelectric devices.[3] As yet however, no information is available on the energy potential barriers at the interfaces of the oxide film and the parameters of the carrier trapping centers in MIS systems with oxides of rare-earth elements as insulators. These parameters can be used to determine the main characteristics of MIS devices and to identify the mechanisms responsible for the electronic processes taking place therein.

Thus, we investigated the photoelectrical properties of silicon MIS structures with samarium and ytterbium oxide insulators and determined the energy barriers at the interphase boundaries and the parameters of the electron trapping centers in the insulator.

Metal–insulator–semiconductor structures of the type Me–Sm_2O_3–Si and Me–Yb_2O_3–Si (where Me=Al or Ni) were fabricated by a technique described in Ref. 2. The thickness of the rare-earth oxide film was in the range $d=0.23-0.28\ \mu$m. The energy barriers at the metal–rare-earth-oxide and silicon–rare-earth-oxide interfaces were determined by the method of internal photoemission of electrons into the insulator[4,5] using the spectral and voltaic dependences of the photocurrent. The photoemission currents were measured with an ÉD-05M electrometer when the samples were illuminated by monochromatic light obtained using a DKsÉl 1000-5 xenon lamp and a large-aperture MDR-2 monochromator.

Figure 1 gives typical dependences of the photocurrent I_f, normalized to a single photon, on the photon energy $h\nu$ of an Al–Sm_2O_3–Si structure plotted using the coordinates

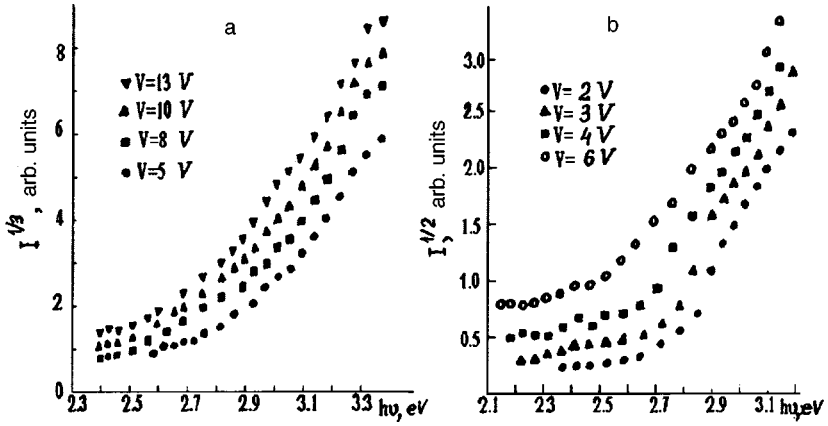

FIG. 1. Reduced photocurrent of Al–Sm_2O_3–Si structure versus incident photon energy for various positive (a) and negative (b) voltages.

TABLE I. Energy barriers at interphase boundaries in metal-insulator-semiconductor structures.

Phase adjacent to rare-earth oxide	Al	Ni	n-Si	p-Si
E_{b0} in Me–Sm_2O_3–Si structure, eV	2.89–2.91	3.29–3.33	2.69–2.72	2.70–2.72
E_{b0} in Me–Yb_2O_3–Si structure, eV	2.90–2.92	3.30–3.32	3.19–3.21	3.18–3.21

$I_f^{1/n}$ versus $h\nu$ for various values of the positive ($n=3$) and negative ($n=2$) voltage V. The characteristics when the electrode is positively biased with respect to the rare-earth oxide (Fig. 1a) correspond to the photoemission of electrons from silicon. In this case, the hole emission from the metal is negligible since for this bias polarity, the threshold photon energy does not depend on the material of the metallic electrode relative to the insulator, and the capacitance-voltage characteristics show that when photocurrent flows through the insulator, trapping of negative charge is observed at deep traps in the Sm_2O_3. The threshold photon energy corresponds to the energy of the potential barrier at the Si–Sm_2O_3 interface for a given positive bias.

The characteristics for $V<0$ (Fig. 1b) correspond to the emission of electrons from the metal. In this case, the threshold photon energy does not depend on the material of the metallic electrode and negative charge builds up in the insulating layer. The threshold photon energy for these photocurrent curves is equal to the potential barrier energy at the Me–Sm_2O_3 interface for the given bias. The investigations showed that the potential barrier E_b has a straight-line dependence on $V^{1/2}$. Extrapolating the curves for E_b versus $V^{1/2}$ until they intersect the E_b axis can give the energy barriers at the interface of the rare-earth oxide in the absence of a bias E_{b0}. Similar qualitative behavior was also observed for the ytterbium oxide structure. The energy barriers at the insulator interfaces in MIS structures are given in Table I. The values of E_{b0} at the Si interface are the same for MIS systems with n- and p-Si. The energy barrier for the Ni–rare-earth oxide interface is 0.4 eV higher than that for the Al–rare-earth oxide interface, which is equal to the difference between the electron work functions of the metals. Similar values of the energy barriers at the interphase boundaries of the rare-earth oxide film were obtained from voltaic dependences of the photoinjection current using a technique described in Ref. 6.

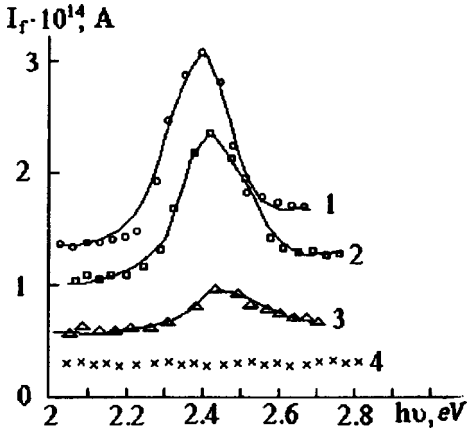

FIG. 2. Spectral dependences of the photodepolarization current: *1*—after photopolarization, *2*—second measurement, *3*—third measurement, and *4*—fourth measurement and initial characteristic.

After the constant-biased structure was exposed to monochromatic light with $h\nu>E_{b0}$, the capacitance-voltage characteristic shifts in the positive direction of the voltage axis, which indicates that negative charge is trapped by deep traps in the insulator.

A method of photostimulated depolarization was used to determine the energy depth of the electron traps in the rare-earth oxide. The spectral dependences of the depolarization photocurrent of an Al–Sm_2O_3–Si structure, measured immediately after photopolarization at incident photon energies of 5.2 eV for 75 min and after repeated measurements, are plotted in Fig. 2. These curves show that after photopolarization, a photocurrent peak appears whose amplitude decreases in repeated measurements, which was not observed before charging the insulator. This photocurrent was caused by trapped electrons being photoexcited from traps into the conduction band of the insulator and drifting in the insulator. In repeated measurements of these dependences, the degree of filling of the electron traps decreases and the photocurrent peak becomes smaller. After complete depletion of the electron traps, the peak disappears and the photocurrent (curve 4 in Fig. 2) and the capacitance-voltage characteristic regain their initial value and position, respectively. This experiment shows extremely good reproducibility. The results plotted in Fig. 2 can be used to estimate the energy depth of the electron traps in Sm_2O_3. It can be seen that the electron trapping centers are positioned almost at the center of the Sm_2O_3 band gap 2.25–2.6 eV from the bottom of the conduction band.

The magnitude and centroid of the trapped charge in the insulator were determined from the displacement of the voltaic dependence of the photocurrent after irradiation.[7] Table II gives the values obtained for the centroid X_c determined from the Si surface, the charge Q_t trapped in the insulator, and the ratio of the trapped to the transmitted charge Q_g. It can be seen that for both structures the charge centroid is positioned almost at the center of the insulator layer. This result shows that in these structures the rare-earth-oxide–Si interface is abrupt and contains no extended damaged transition layer. This is clearly attributable to the comparatively

TABLE II. Parameters of electron trapping centers in insulator.

Structure	X_c, μm	Q_t, C/cm^2	Q_t/Q_g
Al–Sm_2O_3–pSi	0.10	1.2×10^{-10}	0.13
Al–Sm_2O_3–nSi	0.11	3.7×10^{-10}	0.11
Al–Yb_2O_3–pSi	0.13	1.6×10^{-10}	0.16
Al–Yb_2O_3–nSi	0.13	4.5×10^{-10}	0.21

low temperatures used to fabricate the insulating films, which do not create any appreciable mechanical stresses.

[1] O. S. Vdovin, Z. I. Kir'yashkina, and V. N. Kotelkov *et al.*, *Films of Rare-Earth Oxides in MIM and MIS Structures* [in Russian], Saratov State University Press, Saratov (1983) p. 160.
[2] V. A. Rozhkov and A. I. Petrov, Pis'ma Zh. Tekh. Fiz. **11**, 49 (1985) [Sov. Phys. Tech. Phys. **11**, 21 (1985)].
[3] Yu. A. Anoshin, A. I. Petrov, V. A. Rozhkov *et al.*, Zh. Tekh. Fiz. **64**(10), 118 (1994) [*sic*].
[4] B. E. Deal, E. H. Snow, and S. A. Mead, J. Phys. Chem. Solids **27**, 1873 (1966).
[5] R. J. Powell, J. Appl. Phys. **41**, 2424 (1970).
[6] C. N. Berglund and R. J. Powell, J. Appl. Phys. **42**, 573 (1971).
[7] D. J. Di Maria, J. Appl. Phys. **47**, 4073 (1976).

Translated by R. M. Durham

Characteristics of the excitation of ultrasonic waves by thin wafers of manganese zinc ferrite single crystals

V. M. Sarnatskiĭ

Scientific-Research Institute of Physics, St. Petersburg State University
(Submitted August 15, 1997)
Pis'ma Zh. Tekh. Fiz. **24**, 30–34 (March 26, 1998)

It is suggested that thin wafers of a magnetostrictive material may be used as emitters of rf ultrasound. Single crystals of manganese zinc ferrite, which have high magnetostriction constants and low Foucault current losses, were used to investigate the orientational field dependences of the efficiency of excitation of acoustic waves having different polarizations. Some distinguishing features of the excitation of sound by single-crystal wafers compared with polycrystalline samples were observed, and the direction of propagation and polarization of the sound wave and its polarization relative to the crystallographic axes of manganese zinc ferrite with the highest conversion efficiency was identified. © *1998 American Institute of Physics.* [S1063-7850(98)02303-9]

Ultrasonic transducers using magnetostrictive materials are widely used in various fields of science and technology. However, their operating frequency range is limited to hundreds of kilohertz because of the appreciable eddy current losses at higher frequencies and because of the design characteristics.[1] In Ref. 2 we described a method of exciting and recording rf ultrasound (between a few and hundreds of megahertz) using ferrite powders placed in superposed variable and static magnetic fields. It was observed that when the fields were parallel, a longitudinal wave is efficiently excited, whereas when the fields are perpendicular, a shear wave is excited whose polarization vector coincides with the direction of the static magnetic field.

Here results are reported of investigations of the efficiency of excitation of rf ultrasonic waves (5–50 MHz) by transducers fabricated using manganese zinc ferrite (MZF) single crystals which possess high dynamic magnetostrictive characteristics and very low eddy current losses.[3] The transducer consisted of a cylindrical acoustic line with a thin MZF single-crystal wafer attached to the end by means of acoustic cement. The thickness of the wafer is 50–500 μm which corresponds to the establishment of mechanical resonance in a specific vibration mode. The variable magnetic field pulse was excited along the axis of the acoustic line and the direction of the applied static magnetic field was determined by the particular vibration mode. The operating efficiency of the transducer was estimated from the amplitude of the first acoustic pulse transmitted by the acoustic line which was recorded at the opposite end of the line using a suitably cut quartz transducer.

Here particular attention was paid to studying the efficiency of excitation of shear waves. Thus, the variable and static magnetic fields were perpendicular and by acoustic cementing using uncured epoxy resin, the MZF wafer could be rotated at the end of the line so that its sides formed any angle with the direction of the static magnetic field. The MZF wafers were square with 9×9 mm sides oriented in the [100] and [110], and in the [110] and [211] crystallographic directions, and the planes of the wafers were perpendicular to the [110] and [111] directions, respectively, for samples N1 and N2. The magnetoelastic properties of the MZF crystals, which belong to the cubic system, are characterized by two independent magnetostrictive saturation constants L100 and L111 (Ref. 1). The absolute values of L100 and L111 are determined by the chemical composition of the MZF, the impurity content, and the content of divalent iron, and for $Mn_{0.61}Zn_{0.35}Fe_{2.04}O_4$ they are -14.3×10^{-6} and $+3.5\times10^{-6}$, respectively.

Figure 1 gives the shear-wave excitation efficiency A as a function of the magnetizing field in sample N1 for various orientations of the MZF wafers relative to the static magnetic field. In this case, the excited ultrasonic wave propagates in the [110] direction. It can be seen from Fig. 1 that the efficiency of excitation of ultrasound for the case $H_0\|[100]$ is almost an order of magnitude higher than that for the orientation $H_0\|[110]$, which is consistent with the given values of L100 and L111. In addition, for $H_0\|[100]$ the dependence of the ultrasound excitation efficiency on the magnetizing field is monotonic, reaching saturation in a field of 540 Oe and then decreasing slightly as a result of conversion to the single-domain state. For $H_0\|[110]$ on the other hand, this dependence is quasisinusoidal, reaching maxima and minima in fields of 140, 230, 260, 370, and 1000 Oe, respectively, which indicates that the internal field possesses a complex structure. A distinguishing feature of the excitation of sound by single-crystal wafers, unlike polycrystalline powders, is that a longitudinal ultrasonic wave can be excited at the same time as a shear wave when the variable and static magnetic fields are mutually perpendicular, as is illustrated by curve *3* in Fig. 1 for the case $H_0\|[100]$. The efficiency of the excited longitudinal sound has a quasiresonant dependence on the magnetizing field which may be attributed to the appreciable influence of the anisotropy field which for this MZF composition at room temperature is directed along [110] (Ref. 4).

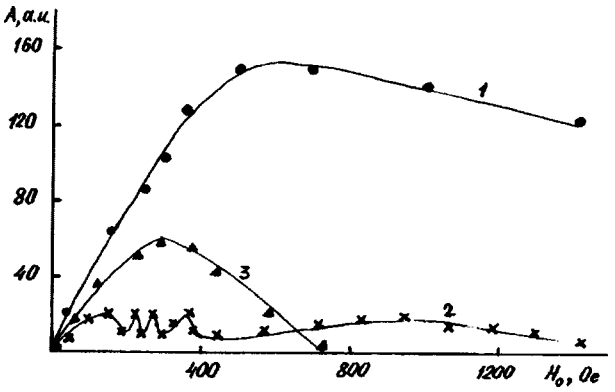

FIG. 1. Efficiency of excitation of shear ultrasonic waves versus static magnetic field H_0 in MZF sample N1: *1*—$H_0 \| [100]$, *2*—$H_0 \| [110]$; *3*—refers to a longitudinal ultrasonic waves; in all cases the direction of wave propagation coincides with the [110] crystallographic direction.

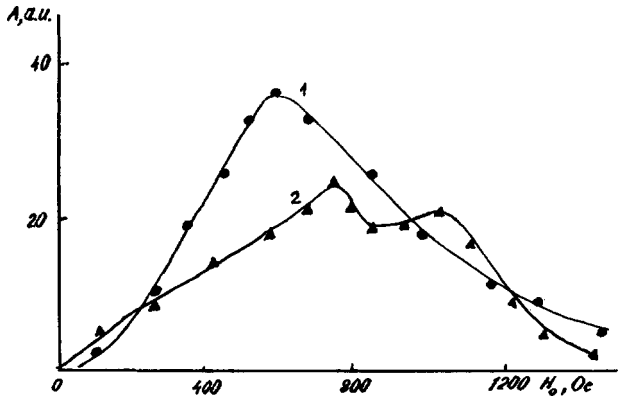

FIG. 2. Efficiency of excitation of a shear ultrasonic wave versus static magnetic field H_0 in MZF sample N2: *1*—$H_0 \| [110]$, *2*—$H_0 \| [211]$; in both cases the wave propagates in the [111] direction.

As a result, the internal field differs from the external field in both magnitude and direction.

The efficiency of excitation of shear ultrasonic waves propagating in the [111] direction in sample N2 as a function of the magnetic field is illustrated by curves *1* and *2* in Fig. 2 for two cases: a) wave polarized in the [110] direction and b) wave polarized in the [211] direction. The difference in the efficiency of excitation of ultrasound polarized in different crystallographic directions is caused by differences in the effective dynamic constants of magnetostriction which, with allowance for the direction cosines of the angles between the selected direction and the direction of the main crystallographic axes, are a combination of L100 and L111, and also depend to a considerable extent on the internal magnetic field. The internal field is determined by the magnitude and relative position of the external magnetic field and the crystallographic axes, by the anisotropy field, the demagnetizing factor, the shape and size of the wafer, and also by the influence of domains of closure.

To sum up, these investigations have revealed an optimum direction for the excitation of a shear ultrasonic wave of maximum intensity by a MZF wafer (wave vector in the [110] direction, polarization vector in the wave in the [100] direction). They have also shown that longitudinal and transverse ultrasound may be excited simultaneously and that the acoustic method may prove useful for studying the magnetic characteristics of single-crystal ferromagnetic materials.

The authors are deeply grateful to I. V. Saenko for supplying samples of MZF single crystals, and also to E. V Charna and S. G. Abarenkova for discussions of the results.

[1] K. P. Belov, *Magnetostrictive Effects and Their Technical Applications* [in Russian], Nauka, Moscow (1987), 155 pp.
[2] V. M. Sarnatskiĭ, A. A. Kuleshov and A. A. Shono, Pis'ma Zh. Tekh. Fiz. **18**(7), 37 (1992) [Sov. Phys. Tech. Phys. **18**, 220 (1992)].
[3] S. G. Abarenkova, I. N. Andreeva, and S. A. Shevchenko, in *Proceedings of Scientific-Technical Conference on Oxide Magnetic Properties*, St. Petersburg, 1992 [in Russian], pp. 26–27.
[4] V. M. Sarnatskiĭ, L. N. Kotov, and V. A. Shutilov, Fiz. Tverd. Tela (Leningrad) **28**, 1783 (1986) [Sov. Phys. Solid State **28**, 988 (1986)].

Translated by R. M. Durham

Polarization properties of a four-layer dielectric waveguide

M. M. Vekshin, V. A. Nikitin, and N. A. Yakovlenko

Kuban State University
(Submitted September 11, 1997)
Pis'ma Zh. Tekh. Fiz. **24**, 35–39 (March 26, 1998)

A new integrated-optics polarizer system is analyzed. Calculations are made and experiments carried out to demonstrate the performance of this system. © *1998 American Institute of Physics.* [S1063-7850(98)02403-3]

Integrated-optics systems for data distribution and processing incorporate optical radiation polarizers which are used to select one of the orthogonally polarized waveguide modes, for example, to suppress undesirable depolarization in order to achieve a high amplitude contrast in interference elements. Similar functions are performed by a polarizer as part of an integrated-optics system incorporated in a fiber-optic gyroscope.

Existing polarizers utilize the following effects for polarization selection:

1) The different level of absorption of TE and TM modes in multilayer waveguides with a metal or semiconducting upper layer;[1–4]

2) Anisotropy of the waveguide layers (for example, in the form of a specially selected crystal clamped to the surface of the waveguide) to separate the fields of TE and TM modes because of the significant birefringence of the entire waveguiding structure;[5,6]

3) A resonant mode coupling effect in directional couplers, which is established for one of the polarization components.[7,8]

Disadvantages of the first type of polarizer include the fundamental difficulty of selecting TM modes with low losses. The second type of polarizer obviously has a cumbersome structure, while the selection principle in the third type of device requires asymmetric directional couplers with high-precision fabrication technology. The development of a simple, efficient, universal TE/TM polarizer is thus a topical problem.

We propose an integrated-optics polarizer based on a four-layer dielectric waveguide which can select either the TE_0 or the TM_0 mode, depending on the design. The polarization selection principle is based on the mode birefringence of a dielectric waveguide, with specially selected parameters which lead to substantial spatial separation of the fields of orthogonally polarized modes.

We consider a four-layer waveguide with a large difference between the refractive indices of the internal layers (Fig. 1a). In practice, this type of structure may be achieved by using an ion-exchange waveguide in glass, on which an upper layer of arsenic sulfide (As_2S_3) of given thickness is deposited. For a mode analysis, we need to determine the propagation constants β corresponding to conditions of transverse phase resonance and then construct the distributions of the mode fields in the waveguide cross section. Such an analysis for this structure indicates that there are two propagation regimes. The guided modes can either propagate in the upper layer, decaying exponentially in the other regions or they can propagate simultaneously in both layers, decaying in the surrounding half-spaces. From the geometric-optics point of view, this means that in the first case, the light wave propagates along a zigzag path in the upper layer, undergoing total internal reflection at its boundaries. In the second case, total internal reflection takes place at the external boundaries of the internal layers of the waveguide.

Figure 1b gives calculated dependences of the effective refractive index N on the thickness of the upper layer D_2 ($N=\beta/k_0$, $k_0=2\pi/\lambda$) near the cutoff. For $n_3<N<n_2$ the graph is the same as that for a three-layer waveguide consisting of an As_2S_3 film on a glass substrate. The condition $N=n_3$ indicates the boundary of the two propagation regimes. For values of the thickness D_2 near the cutoff conditions there is a fairly large difference between the effective refractive indices of the highest-order TE and TM modes (~ 0.002). Having calculated the propagation constants β, we can construct the fields of the TE and TM modes (Fig. 2) for this particular waveguide for optimum values of the film thickness D_2 and also for $D_2=0$.

The entire structure corresponds to a composite waveguide consisting of a weakly guiding waveguide in glass with a highly refracting film deposited locally on its surface. The fields of the TE_0 and TM_0 modes of the base ion-exchange waveguide are almost identical. For specially selected values of the film thickness D_2 in the four-layer waveguide, the distributions of the different mode fields differ substantially so that a simple and efficient polarization device can be fabricated to select either the TE_0 or the TM_0 modes. It should be noted that as the film thickness increases, a similar difference in the field distribution appears selectively for the higher-order modes. In addition, the level of localization of the field in the upper layer for modes near the cutoff increases negligibly with increasing mode index, so that polarizers with low insertion losses can be produced by using different intervals of film thicknesses.

We carried out an experiment which confirmed the efficiency of the proposed method of polarization selection. Ten single-mode channel waveguides were fabricated by K^+ ion exchange in an optical glass substrate. An A_2S_3 film was deposited on the surface of the substrate as a wedge across

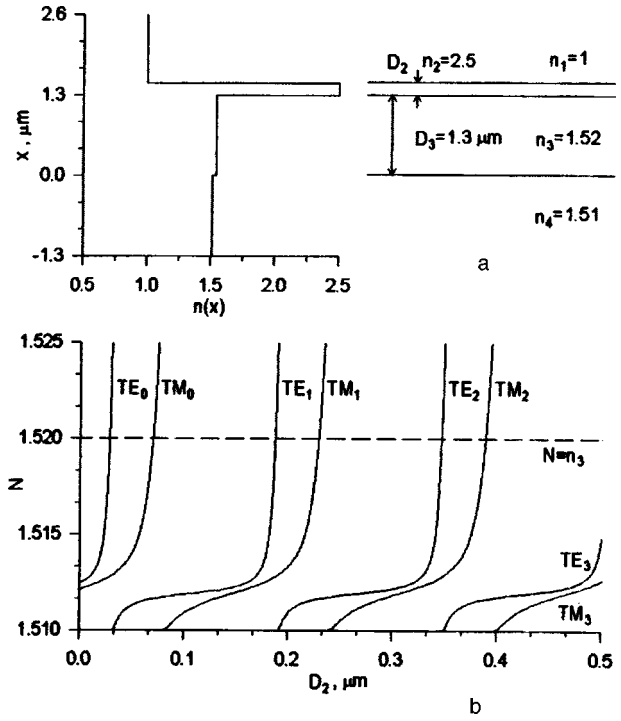

FIG. 1. a) Four-layer waveguide structure and its refractive index distribution; n_i $(i=1,\ldots,4)$ are the refractive indices of the layers at the wavelength $\lambda=0.63$ μm, D_2 and D_3 are the thicknesses of the internal layers. b) Effective refractive index N versus thickness of upper layer D_2.

the waveguides such that only the film thickness varied, other conditions being approximately equal. An experimental investigation of the polarization characteristics revealed that as the film thickness increases, individual waveguides exhibit TM- and TE-selective properties, these waveguides being separated by ones which possess no polarization sensitivity. A series of similar measurements was made with different wedge slopes and the behavior was repeated. Some waveguides had a coefficient of decoupling between the modes (determined from the intensity ratio of the orthogonally polarized signals) higher than 30 dB with losses less

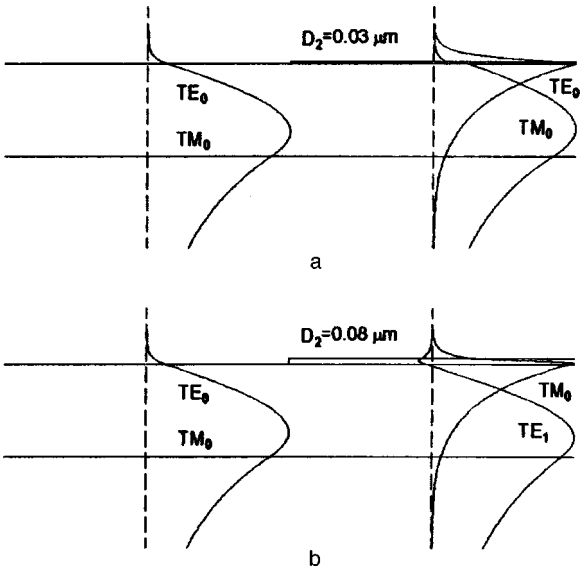

FIG. 2. Integrated-optics TM-polarizer (a) and TE-polarizer (b).

than 1 dB for the selected polarization. By depositing a homogeneous film of a particular thickness, we obtained arrays of TE and TM polarizers.

To conclude, we have proposed a method for polarization filtering of radiation which uses the mode birefringence near cutoff in a four-layer dielectric waveguide with a specially selected refractive index profile. Efficient integrated-optics TM and TE polarizers have been fabricated and investigated.

[1] I. P. Kaminow, W. L. Mammel, and H. P. Weber, Appl. Opt. **13**, 396 (1974).
[2] M. A. Sletten and R. S. Seshadri, J. Appl. Phys. **70**, 574 (1990).
[3] R. F. Carson and T. E. Batchman, Appl. Opt. **29**, 2769 (1990).
[4] D. Veasey and D. Larson, J. Lightwave Technol. **13**, 2244 (1995).
[5] T. Findakly, B. U. Chen, and D. Booher, Opt. Lett. **8**, 641 (1983).
[6] U. Hempelmann *et al.*, J. Lightwave Technol. **13**, 1750 (1995).
[7] K. Thyagarajan *et al.*, J. Lightwave Technol. **9**, 315 (1991).
[8] R. Vallee and G. He, J. Lightwave Technol. **11**, 1196 (1993).

Translated by R. M. Durham

Investigation of nanocrystals in thin layers of paraffin lubricant on the surface of metals by infrared spectroscopy

V. I. Vettergren' and A. I. Tupitsyna

A. F. Ioffe Physicotechnical Institute, Russian Academy of Sciences, St. Petersburg; Institute of Problems in Mechanical Engineering, Russian Academy of Sciences, St. Petersburg
(Submitted March 14, 1998)
Pis'ma Zh. Tekh. Fiz. **24**, 40–44 (March 26, 1998)

It has been shown that when the thickness of a layer of paraffin lubricant on a metal substrate decreases, the crystallites become damaged and the alkane solid solutions become partially separated. [S1063-7850(98)02503-8]

Studies of the interaction between a lubricant and a solid substrate are of topical interest, being of applied and fundamental importance.

Here infrared spectroscopy is used to study changes in the crystal structure in samples of paraffin lubricants on a metal surface as the thickness of the lubricant layer is reduced from ~ 15 to ~ 1 μm. For the investigations we used samples of OKB-122–7–5 engineering lubricant based on ceresine and Vaseline, which consists of mixtures of alkane molecules having different branching ratios, containing several tens of carbon atoms. Layers of different thickness were applied to Al and Cu plates with a brush. The thickness of the lubricant layer was determined by weighing and from the optical density D(1240) and D(1378) of the 1240 and 1378 cm^{-1} reference bands.

A transmission-reflection technique was used to obtain spectra of the samples on an infrared-opaque metal substrate. The angle of incidence of the light beam on the sample was 20°. The spectra were recorded using a Specord-75 IR spectrophotometer.

Measurements were made of the intensities and frequencies of the rocking, scissoring, and stretching vibration bands of the methylene groups in the infrared spectra of samples of different thickness.

The spectra of the lubricant revealed doublets of rocking ($720-730$ cm^{-1}) and scissoring ($1465-1475$ cm^{-1}) vibrations caused by frequency splitting as a result of the interaction of vibrations in orthorhombic crystal cells.[1] Thus, some of the molecules in these samples form orthorhombic crystals.

Figure 1 gives the ratio of the optical densities of the 730 cm^{-1} and 1378 cm^{-1} bands, D(730)/D(1378) as a function of thickness, expressed in units of the optical density of the 1378 cm^{-1} band, for samples of Vaseline on an aluminum substrate. The value of D(730)/D(1378) is proportional to the concentration of alkane molecular segments four monomer units long in the orthorhombic crystal cells.[1] It can be seen that this ratio decreases as the sample thickness decreases. The same result was obtained for samples of OKB-122–7–5 lubricant.

Figure 2 gives the infrared spectra of Vaseline on an aluminum substrate at frequencies corresponding to the CH_2 scissoring and CH_3 bending vibrations.[2] A sample ~ 15 μm thick reveals overlapping 1472.5, 1476, and 1464 cm^{-1} bands. The first and last band are assigned to CH_2 scissoring vibrations of molecular segments appreciably longer than four monomer units in the orthorhombic crystal lattice, while the ~ 1467 cm^{-1} band is assigned to bending vibrations of methyl groups.

It can be seen that as the sample thickness decreases from ~ 15 to ~ 1 μm, the intensity of the 1472.5 cm^{-1} band decreases while that of the 1474 cm^{-1} band increases. Ultimately, the effect is reduced to an increase in the degree of splitting between the components of the ''crystalline'' doublet by ~ 1.5 cm^{-1}. It is known[3] that the spacing between the components of a particular doublet increases as the effective length of the molecules forming the crystallite increases.

Thus, in thin layers of the lubricant samples the average effective length of the molecules in the crystallites increases.

It was also observed that for the 1 μm thick sample the ratios of the peak intensities of the 1474 and 1474 cm^{-1} bands to the intensity of the 1378 cm^{-1} reference band are approximately twice the intensity ratios of the components in the spectrum of the 15 μm thick sample. This effect is attributed to an increase in the concentration of ''long'' molecular sections in the crystallites.

It was also observed that as the thickness of the sample layer decreases, the maxima of the CH stretching vibration bands are shifted by $1-3$ cm^{-1} toward lower frequencies.

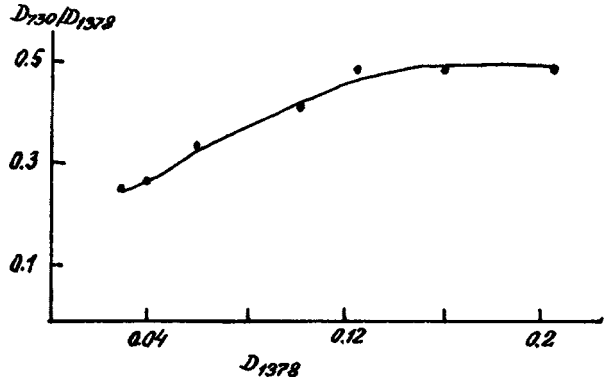

FIG. 1. Graph of D(730)/D(1378) versus D(1378) cm^{-1} for samples of Vaseline on an aluminum substrate. For explanations see text.

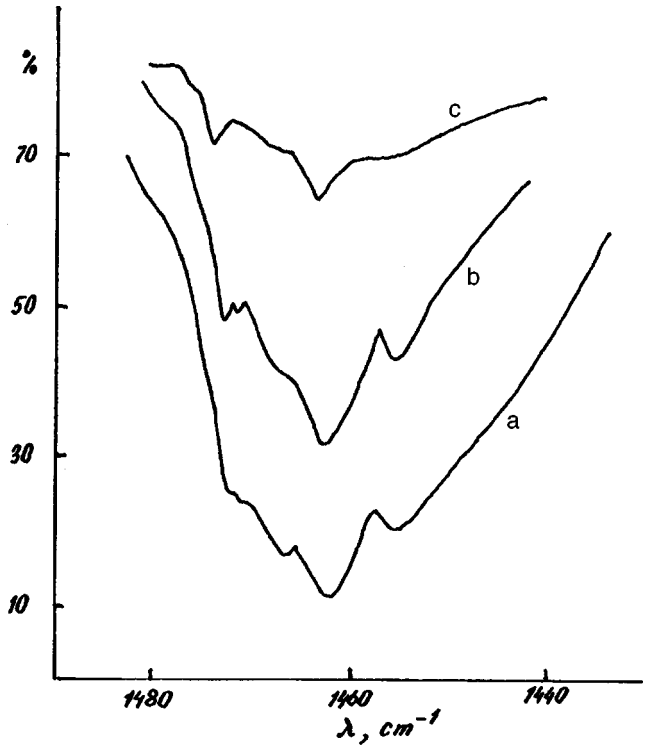

FIG. 2. Infrared transmission spectra of Vaseline samples of different thickness in the range 1480–1440 cm^{-1}: a—layer thickness ~15 μm, b—layer thickness ~8 μm, and c—layer thickness ~1 μm. Substrate—aluminum.

This effect is caused by an increase in the concentration of trans conformers in the alkane molecules.[4,5]

The changes observed in the infrared spectra of thin layers of paraffin lubricant can be explained as follows.

Since these samples are mixtures of alkanes of different length, the crystalline regions are solid solutions. It was shown in Refs. 6 and 7 that molecules forming solid solutions contain gauche conformers localized predominantly near the ends of longer molecules. The concentration of gauche conformers increases as the difference between the lengths of the molecular chains forming the crystal increases. When the solid solution separates into components having a more uniform molecular composition, the concentration of gauche conformers decreases and the average effective length of the molecules in the crystal increases.

When a larger crystallite separates into smaller ones, the total free surface area of the crystalline phase obviously increases. The molecules forming the surface layer do not make any contribution to the ''crystal'' bands and this is why the relative optical density of the 730 cm^{-1} band decreases. This effect may be observed if the transverse dimensions of the crystallites do not exceed a few tens of chains (nanometers).

In order to confirm that the observed effects are not caused by the mechanical action of the brush on the lubricant during preparation of the layers, samples of different thickness were heated to a temperature exceeding the melting point of the crystallites and were then cooled to room temperature. The observed effects are reproduced in the spectra of the cooled samples of different thickness.

In our opinion, these effects are caused by the compressive pressure produced by the adhesive interaction between the lubricant and the metal.

[1] R. G. Snyder, J. Chem. Phys. **47**, 1326 (1967).
[2] R. G. Snyder, J. Chem. Phys. **71**, 3229 (1979).
[3] D. G. Cameron, E. F. Gudgin, and H. H. Mantsch, Biochemistry **20**, 4496 (1981).
[4] H. L. Casal, D. G. Cameron, and H. H. Mantsch, Can. J. Chem. **61**, 1736 (1981).
[5] R. G. Snyder, H. L. Strauss, and C. A. Elliger, J. Phys. Chem. **86**, 5145 (1982).
[6] M. Maroncelli, H. L. Strauss, and R. G. Snyder, J. Phys. Chem. **89**, 5260 (1985).
[7] R. G. Snyder, G. Conti, H. L. Strauss, and D. L. Dorset, J. Phys. Chem. **97**, 7342 (1993).

Translated by R. M. Durham

Influence of short-term annealing on the conductivity of porous silicon and the transition resistivity of an aluminum-porous silicon contact

S. P. Zimin and E. P. Komarov

P. G. Demidov State University, Yaroslavl
(Submitted July 22, 1997)
Pis'ma Zh. Tekh. Fiz. **24**, 45–51 (March 26, 1998)

Measurements were made of the transition resistivities of an aluminum-porous silicon contact and the resistivity of the surface region of the porous material after short-term annealing in an inert medium at temperatures between 300 and 550 °C. It was shown that the parameters of the contacts are determined by the pore morphology, the annealing temperature, and the plasma-chemical etching process. For porous silicon formed on p-Si, annealing reduces the transition resistivities by several orders of magnitude. In this case, the resistivity of the surface region of porous silicon decreases sharply. The results are analyzed from the point of view of the passivating effect of hydrogen in the porous silicon. © *1998 American Institute of Physics.* [S1063-7850(98)02603-2]

The fabrication of semiconductor structures with porous silicon (PS) active layers involves forming Ohmic and rectifying contacts with the porous layer. At present, the literature contains contradictory information on the properties of a metal-porous silicon contact and almost no information on the influence of heat treatment on the electrical parameters of such a contact. In addition, at high annealing temperatures the properties of the porous material itself may well change. Here we study the effect of short-term annealing (300–550 °C) in an inert medium on the conductivity of porous silicon and the transition resistivity of Al–PS contacts for various structural characteristics of the porous layer.

The investigations were carried out using test structures whose geometry was as described in Ref. 1. The initial silicon substrates doped with boron (0.03 $\Omega\cdot$cm) and phosphorus (4.5 $\Omega\cdot$cm) were oriented in the (111) and (100) directions, respectively. The porous layer was formed by anodic electrochemical treatment in a hydrofluoric-acid-based electrolyte with an anodizing current density of 1 mA/cm^2 for 10–60 min. The porous silicon layers were 17–90 μm thick and the porosity by weight was 16–40% for the p-type silicon and 5–10% for the phosphorus-doped silicon. The pore morphology differed for the n- and p-type silicon. The phosphorus-doped silicon had large cylindrical pores, 1–2 μm in diameter, oriented parallel to the [100] axis and separated by 3–10 μm (Ref. 2). The boron-doped silicon exhibited a highly branching network of small nanometer-size pores. For the reference samples the surface of the porous silicon was subjected to additional plasma-chemical treatment to remove the amorphized surface film. Aluminum contact areas having the same area, distributed equidistantly in a line, were deposited on the surface of the porous layer by vacuum deposition. The Al–PS contacts were initially brazed in nitrogen at $T_0 = 300$ °C for 10 min. The electrical parameters of the contacts were determined using a method described in Ref. 3. A characteristic feature of these structures was the presence of two layers of different resistivity, where the conductivity of the substrate appreciably exceeds that of the porous layer. Thus, in order to eliminate the shunting effect of the substrate, the measurements using the method described in Ref. 3 were only made for small currents not exceeding 15 μA. It was assumed that applying low voltages to the contact areas induces carrier drift only in the surface region of the porous silicon. A current-limited four-probe method was used to estimate the resistivity in the surface region of the porous material.

Measurements of the current-voltage characteristics of these Al–PS–Al structures showed that at low current densities across the contact not exceeding 1 mA/cm^2, the dependences are linear. At higher currents, some deviation from linearity was observed, possibly caused by the shunting effect of the substrate and by the non-Ohmic nature of the contact. Since it is fairly difficult to separate these two effects experimentally, it should be noted that in general, the observed linear section at low currents cannot be identified with the Ohmic character of the contact over a wide range of bias. This behavior of the current-voltage characteristic may be caused by the linearity of the Schottky barrier near the zero point. However, the experimental results suggest that, at least at low current densities across the contact (less than 1 mA/cm^2), the Al–PS contact does not exhibit nonlinear properties and thus this nonlinearity can be eliminated when analyzing carrier transport effects in porous silicon structures.

The linear behavior of the current-voltage characteristics of the Al–PS contact at low currents allowed us to use the method described in Ref. 3 to determine the transition resistivities of the contact R_c which had a wide range of values depending on the pore morphology and the plasma-chemical etching process. For porous silicon formed on n-type silicon the transition resistivities were 0.6–18 $\Omega\cdot$cm^2 whereas for porous silicon formed on p–Si, they varied between 0.6 and 1.3 k$\Omega\cdot$cm^2. Plasma-chemical etching of the porous silicon surface prior to deposition of the metal resulted in changes in

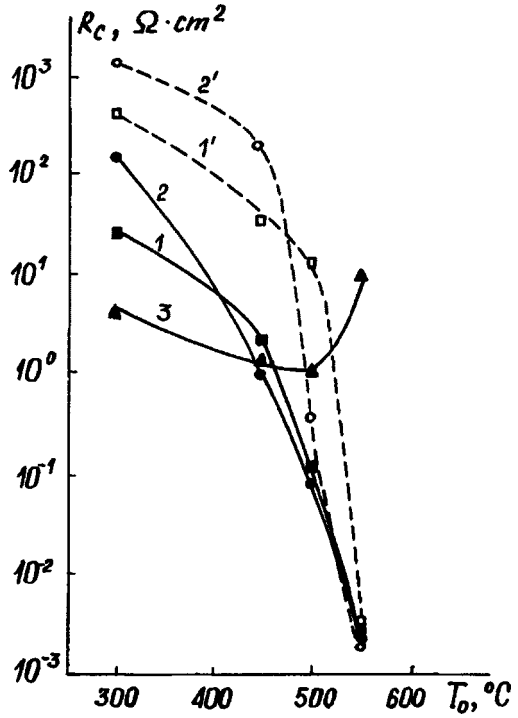

FIG. 1. Transition resistivity of Al–PS contact versus annealing temperature for porous silicon on p–Si (*1*, *1′*, *2*, *2′*) and n–Si (*3*). Anodizing time: *1* and *1′*—20 min, *2* and *2′*—40 min, *3*—60 min. Samples *1′* and *2′* did not undergo plasma-chemical etching.

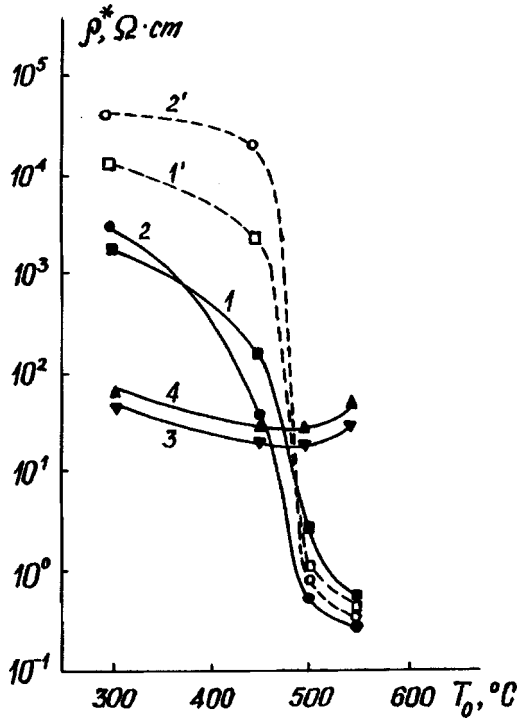

FIG. 2. Influence of annealing temperature on the resistivity of the surface region of porous silicon. The notation *1*, *1′*, *2*, *2′* is the same as in Fig. 1. Porous silicon samples *3* and *4* were prepared on an n-Si substrate with anodizing times of 40 min (*3*) and 60 min (*4*) and were subjected to plasma-chemical etching.

R_c. In particular, removal of the amorphized film from the surface of porous silicon on n–Si reduced the transition resistivities by a factor of 3–10. Figure 1 shows the transition resistivity of Al–PS contacts after gradual short-term annealing (5–7 min) in an inert N_2 atmosphere at temperatures T_0=450–550 °C. It can be seen that for porous silicon on p–Si, R_c decreases continuously during annealing to $(1-3)\times 10^{-3}\Omega\cdot\mathrm{cm}^2$. In this case, the difference between the electrical properties of the contacts with and without the amorphized film disappears. For porous silicon formed on n–Si the changes in the transition resistivities of the contact caused by annealing were less well-defined (curve *3*).

Since the parameters of metal-silicon contacts are in many respects determined by the carrier concentration (conductivity) in the semiconductor,[4] it was interesting to compare these results with measurements of the resistivity ρ^* of the surface region of the porous silicon. Figure 2 shows the variation of ρ during gradual annealing. It can be seen that initially for porous silicon on p–Si the resistivity of the surface region for samples with an amorphized film exceeds ρ^* for samples with the film removed. Heat treatment causes a sharp drop (by several orders of magnitude) in the resistivity. For large-pore porous silicon obtained on phosphorus-doped silicon, the resistivity decreased by a factor of 1.5–3 during annealing at 450 and 500 °C whereas annealing at 550 °C caused a slight increase in ρ^*. Thus, there is a correlation between the changes in the transition resistivities of the contacts and the resistivity of the surface region of porous silicon for both n–Si and p–Si.

These results may be explained using a model based on the passivating effect of hydrogen atoms. It has been established that the hydrogen in silicon can electrically neutralize dopant atoms and reduce the carrier concentration.[5,6] The electrical activity of the dopant atoms can be restored by short-term high-temperature annealing.[7] Since during anodic treatment the hydrogen atoms are in contact with the silicon matrix, it is possible for hydrogen atoms to diffuse into the single-crystal matrix of the porous material.[8] Estimates made using known values of the coefficient of hydrogen diffusion showed that at room temperature the depth of hydrogen penetration during anodization may be a few tenths of a micrometer. Thus, each pore has a depleted region around it and for porous silicon with a developed network of small pores, the depleted regions may occupy the entire volume of the single-crystal matrix of the porous silicon. For porous silicon with fairly well-spaced large pores, the depleted regions will only extend to part of the matrix bulk.[2] If annealing is accompanied by the effusion of hydrogen and restoration of the electrical activity of the dopants, this explains why such a large difference is observed between the properties of porous silicon on p–Si and n–Si. In large-pore porous silicon, the decrease in the resistivity caused by annealing is less well-defined because the carrier concentration only increases in part of the bulk of the porous silicon matrix. It is also known that hydrogen has a weaker passivating effect in n–Si compared with p–Si (Ref. 7).

To conclude, these results suggest that short-term annealing in an inert atmosphere can be used to vary the electrical parameters of a metal-porous silicon contact and the change in the conductivity of the porous material is an important factor. It has been shown that the morphology of the

porous layer plays a significant role in these processes. The variation in the conductivity of porous silicon when exposed to high temperatures must be taken into account when fabricating multilayer structures by high-temperature methods, such as epitaxial growth on porous silicon. Laser or radiation methods of treatment may also be promising for locally changing the electrical properties of a porous material and creating enriched zones.

This work was supported financially by grants from the State Committee for Higher Education of the Russian Federation for fundamental research in electronics and chemical technologies.

The authors are deeply grateful to A. A. Lebedev (A. F. Ioffe Physicotechnical Institute, St. Petersburg) for useful discussions on the passivation of dopant atoms in porous silicon. Thanks are also due to V. A. Rekshinskiĭ and M. I. Makoviĭchuk for annealing the samples.

[1] S. P. Zimin, V. S. Kuznetsov, and A. V. Prokaznikov, Appl. Surf. Sci. **91**, 355 (1995).
[2] S. P. Zimin, Pis'ma Zh. Tekh. Fiz. **21**(24), 46 (1995) [Tech. Phys. Lett. **21**, 1015 (1995)].
[3] K. A. Valiev, V. N. Dyagilev, V. I. Lebedev, and A. V. Lubashevskiĭ, *Micropower Integrated Circuits* [in Russian], Sovet-skoe Radio, Moscow (1975), 256 pp.
[4] S. M. Sze, *Physics of Semiconductor Devices* [Wiley, New York (1969); Énergiya, Moscow (1973), Vol. 1, 456 pp.].
[5] S. J. Pearton, J. W. Corrbett, and T. S. Shi, Appl. Phys. A. **43**, 153 (1987).
[6] B. N. Mukashev, M. F. Tamendarov, and S. Zh. Tokmoldin, Fiz. Tekh. Poluprovodn. **26**(6), 1124 (1992) [Sov. Phys. Semicond. **26**, 628 (1992)].
[7] I. A. Kurova, N. V. Meleshko, E. V. Larina *et al.*, Fiz. Tekh. Poluprovodn. **30**, 12 (1996) [Semiconductors **30**, 6 (1996)].
[8] P. Allongue, C. Henry de Villeneuve, L. Pinsard, and M. C. Bernard, Appl. Phys. Lett. **67**, 941 (1995).

Translated by R. M. Durham

Local polarization reversal of $LiNbO_3$ by scanning the surface perpendicular to the axis of spontaneous polarization with a needle-shaped electrode

S. O. Fregatov and A. B. Sherman

A. F. Ioffe Physicotechnical Institute, Russian Academy of Sciences, St. Petersburg
(Submitted October 14, 1997)
Pis'ma Zh. Tekh. Fiz. **24**, 52–57 (March 26, 1998)

The principle of local polarization reversal of ferroelectrics using a moving needle-shaped electrode[1] was used to make a comparative study of the characteristics of polarization reversal of $LiNbO_3$ from the $Z(001)$ and $Y(010)$ surfaces. In addition to chemical etching, an optical polarization method was used to visualize the domain structure. It was noted that the different dependences of the domain length on the polarizing voltage observed for the different crystal surfaces may be caused by the conducting and polarization properties of the regions in which the domain growth occurs. It is shown that the depth of penetration of the created domains in the sample may be set. © *1998 American Institute of Physics.* [S1063-7850(98)02703-7]

In Ref. 1 we proposed a new principle for the creation of a domain structure in ferroelectrics using a moving needle-shaped electrode (similar to the tip of a scanning tunneling microscope). At comparatively low voltages (more than an order of magnitude lower than the usual values[2]), the electric field near this electrode is sufficient to reverse the polarization even in the hardest ferroelectrics. Polarization reversal takes place in the surface region of the crystal only near the point of contact of the electrode. By moving the needle over the surface of the sample, it is possible to form domain structures with a particular surface configuration.

Experiments using lithium niobate have shown that local polarization reversal takes place when the electrode is in contact with the crystal surfaces parallel and perpendicular to the axis of spontaneous polarization.

In Ref. 1 particular attention was paid to studying the polarization reversal of $LiNbO_3$ on the $Y(010)$ surface. In this case, the ferroelectric domains only develop over the surface in one direction from the electrode displacement trajectory. The domains are needle-shaped and oriented parallel to the axis of spontaneous polarization. The length of the domains increases as the applied voltage increases and at $U=2.7$ kV reaches 15 μm. It was established that the thickness of the surface region in which polarization reversal takes place does not exceed ≈ 0.15 μm.

Here we present information on the local polarization reversal of lithium niobate from the $Z(001)$ surface. We were able to obtain this new data because the usual method of visualizing ferroelectric domains by chemical etching was supplemented by an optical method of visualization based on the local variation in the birefringence of the crystal accompanying polarization reversal. Since domains of opposite sign cannot be distinguished optically in uniaxial ferroelectrics, this variation in birefringence can only occur near domain walls as a result of local elastic stresses in the crystal lattice and local electric fields.[3,4]

The birefringence pattern was studied in transmitted light using a microscope with a polarizing stage. The observations were made on the side of the working surface in contact with the moving needle-shaped electrode (''direct'' observation) and across the side surface of the sample (''side'' observation). The microscope analyzer and the polarizer were almost crossed and the samples were oriented such that their intrinsic birefringence did not impede the observations.

Figure 1a shows a photograph obtained by direction observation after parallel lines had been drawn on the Z surface of the lithium niobate sample by the contacting needle at different applied voltages ($U=2.1$ and 2.5 kV). Polarization reversal took place at a tip velocity of ≈ 1 mm/s. The optical contrast on the photograph indicates some local variation in the birefringence near these lines. As the voltage decreases, the contrast becomes lower and can no longer be identified for $U<500$ V.

Etching reveals that the local variation in the birefringence is caused by the formation of ferroelectric domains along the trajectories of the needle-shaped electrode. An examination of this surface in reflected light reveals pairs of parallel dark grooves along the sides of each line along which polarization reversal occurred (Fig. 1b). The grooves were formed as a result of the enhanced rate of etching of the ferroelectric which is usually observed at the location of domain walls.

Figure 1c shows the local variations in birefringence revealed by the observations from the side. These observations can yield information on the shape and depth of the domain penetration. Longitudinal polarization reversal was carried out on the Z surface at $U=2.5$ kV. The photograph reveals a structure of alternate light and dark bands, having an average period of ≈ 2 μm and extending from the surface into the sample to a depth of ≈ 55 μm. The photograph shows that this polarization reversal is not accompanied by the formation of a continuous domain but by a quasiregular structure

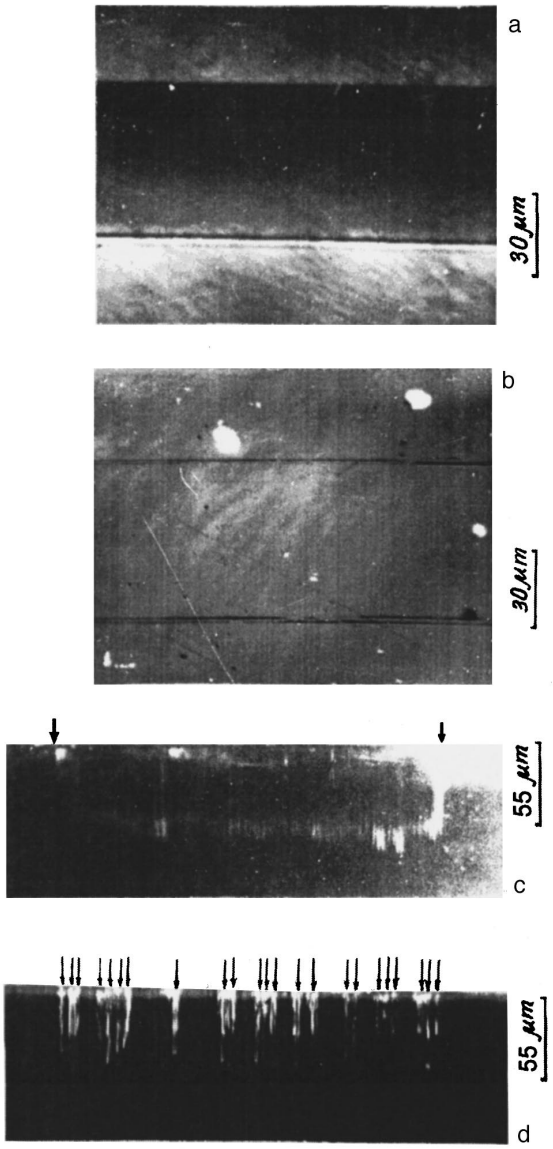

FIG. 1. Domain structure produced by local polarization reversal from the Z surface. Direct observation of the crystal surface: a—using polarized light, polarization reversal at $U=2.1$ kV (upper) and $U=2.5$ kV (lower); b—the same part of the surface in reflected light after chemical etching. Observation from the side of part of the crystal near the Z surface in polarized light, polarization reversal at $U=2.5$ kV; c—along a continuous line (the arrows indicate the beginning and end of the electrode motion); d—at isolated points (indicated by the arrows).

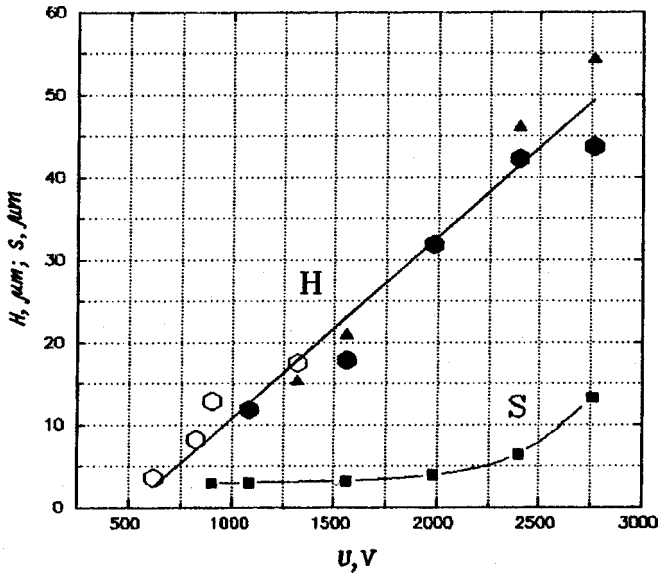

FIG. 2. Domain length H for polarization reversal from Z surface and width of etched region S for polarization reversal on Y surface versus applied voltage U.

of needle-shaped domains oriented parallel to the axis of spontaneous polarization.

The photograph shown in Fig. 1d was obtained by observations from the side after a slightly different polarization reversal procedure had been carried out from the Z surface. The voltage $U=2.5$ kV was applied over a time t to a fixed electrode in contact with this surface. The electrode was then moved to a new position and voltage was again applied. As a result of repeating this operation several times, polarization reversal was achieved at isolated points between 10 and 40 μm apart, distributed along a line segment. The time t was varied between 0.2 and 10 s. Separate regions of polarization reversal in the form of needle-shaped domains can easily be identified on the photograph. In this case, the contrast of the image is appreciably higher than that observed for polarization reversal along a continuous line, when the local variations of the electric and elastic fields are reduced because of the close proximity of the domain walls ($\approx 1\ \mu$m). As in Fig. 1c, the depth of penetration of the domains in the sample is $\approx 55\ \mu$m and remains constant for the pulse durations used. Our estimates indicate that the domain width does not exceed 2 μm.

Figure 2 gives the domain length H versus voltage for polarization reversal at isolated points on the Z surface. Also plotted is the dependence $S(U)$ which gives the width of the etched region formed on the Y surface after polarization reversal along a continuous line. The curve $S(U)$ is plotted using data from Ref. 1. In Ref. 1 we related this width to the length of the domains. These dependences differ and also for the same voltage the domain length for the Z surface is always greater.

The differences observed in the local polarization reversal characteristics may be attributed in particular to differences in the conducting and polarization properties of the regions of domain growth.

These results show that a needle-shaped electrode can be used to create domain structures in a ferroelectric which not only have a specific surface configuration but also a given depth of penetration in the sample.

[1] S. O. Fregatov and A. B. Sherman, Pis'ma Zh. Tekh. Phys. **23**(11), 54 (1997) [Tech. Phys. Lett. **23**, 758 (1997)].
[2] S. Zhu, Y. Zhu, and Z. Zhang, J. Appl. Phys. **77**, 5481 (1995).
[3] Yu. S. Kuz'minov, *Electrooptic and Nonlinear-Optical Lithium Niobate Crystals* [in Russian], Nauka, Moscow (1987), 264 pp.
[4] V. V. Antipov, A. A. Blistanov, and N. G. Sorokin, Kristallografiya **30**, 734 (1985) [Sov. Phys. Crystallogr. **30**, 428 (1985)].

Translated by R. M. Durham

Properties of GaInAsSb solid solutions obtained from antimony fluxes by liquid-phase epitaxy in the spinodal decay region

V. I. Vasil'ev, A. G. Deryagin, V. I. Kuchinskiĭ, V. M. Smirnov, G. S. Sokolovskiĭ, D. N. Tret'yakov, and N. N. Faleev

A. F. Ioffe Physicotechnical Institute, Russian Academy of Sciences, St. Petersburg
(Submitted October 22, 1997)
Pis'ma Zh. Tekh. Fiz. **24**, 58–62 (March 26, 1998)

The growth of epitaxial layers of GaSb lattice-matched $Ga_{1-x}In_xAs_ySb_{1-y}$ solid solutions by liquid-phase epitaxy from Sb-enriched liquid phases within the spinodal decay region is reported. The highest value of the composition ($x=0.4$) was achieved for growth on a GaSb(111)B substrate. Results of investigations of the luminescence and structural properties of these solid solutions are presented. © *1998 American Institute of Physics.* [S1063-7850(98)02803-1]

The existence of an extensive miscibility gap in the quaternary system of $Ga_{1-x}In_xAs_ySb_{1-y}$ solid solutions has been predicted in various theoretical studies, for example, in Refs. 1 and 2. Of practical interest are those solid solutions lattice-matched with GaSb. Theoretical models describing the miscibility gap and the region of spinodal decay within this gap have shown that GaSb lattice-matched $Ga_{1-x}In_xAs_ySb_{1-y}$ solid solutions cannot be obtained for $x \geqslant 0.29$ under practical conditions of liquid-phase epitaxy. Experimental studies of the liquid-phase growth of these solid solutions on GaSb substrates have also reported serious problems involved in producing compositions with $x>0.18$ (Refs. 3 and 4). The highest compositions of GaSb lattice-matched epitaxial layers were obtained in Refs. 2 and 4, where $x=0.23$, $y=0.2$ was obtained for growth on GaSb(100) and $x=0.26$, $y=0.23$ for growth on GaSb(111)B.

Here we report the growth of GaSb lattice-matched $Ga_{1-x}In_xAs_ySb_{1-y}$ solid solutions in the spinodal decay region by liquid-phase epitaxy from antimony fluxes (where values of $x=0.4$ were achieved). The luminescence and structural properties of these epitaxial layers were investigated.

Undoped layers of GaInAsSb solid solutions were grown by liquid-phase epitaxy from Sb-enriched fluxes on undoped (100) and (111)B-oriented p-type GaSb substrates. The use of antimony liquid phases to obtain these solid solutions was first proposed by us and was described in our earlier studies.[5–7] The composition of the layers was determined using a Camebax x-ray microanalyzer and for layer thicknesses less than 1 μm we used secondary ion mass spectroscopy data. The mismatch between the lattice parameters of the epitaxial layer and the substrate $f_\perp$ was measured by double-crystal x-ray diffraction. The photoluminescence spectra were recorded with an MDR-23 monochromator. An LG-106-M1 gas laser was used for excitation and a cooled PbS photoresistor was used as the detector. The thicknesses of the epitaxial layers were measured with a DECTAK profilometer.

The samples were grown from supercooled liquid phases at constant temperature. The supercooling $\Delta T=T_L-T_g$ (where T_L and T_g are the liquidus temperature of the liquid phase and the growth temperature, respectively) was varied between 8 and 12 °C. The values of T_g were selected in the range 575–600 °C. The ranges of compositions of the as-grown $Ga_{1-x}In_xAs_ySb_{1-y}$ epitaxial layers having lattice parameters similar to GaSb were $0.2 \leqslant x \leqslant 0.32$ for the (100) orientation and $0.25 \leqslant x \leqslant 0.4$ for the (111)B orientation. These layers had a mirror-smooth surface. The growth rate was varied between 3 and 0.05 μm/min as x increased.

Figure 1 shows the photoluminescence spectra of various samples at 77 K. We observed photoluminescence spectra having bands with a half-width of 20–25 meV (Figs. 1a and 1c) typical of GaInAsSb solid solutions of uniform composition and also broad bands ($\Delta h\nu=40-50$ meV) (Fig. 1b) with well-defined asymmetry. In the first case, the x-ray diffraction data showed that the absolute values of the lattice mismatch were close to zero (allowance for the difference between the coefficients of thermal expansion of the layer and substrate materials indicates a negative lattice mismatch at the epitaxial growth temperature). The half-widths of the diffraction reflection peaks for the layer and the substrate were similar, between 11″ and 20″. Samples for which the photoluminescence spectra were similar to that plotted in Fig. 1b had a positive lattice mismatch $f_\perp=(1-3)\times10^{-3}$. From these results it may be preliminarily supposed that the situation when the growing epitaxial layer extends along the heteroboundary is more favorable to obtain homogeneous layers in the spinodal decay region. In cases where the growing layer is compressed along the heteroboundary, the x-ray diffraction spectra differ from those normally observed, having additional peaks (Fig. 2) whose appearance may be attributed to spinodal decay processes. A distinguishing feature of the liquid-phase growth of GaInAsSb solid solutions whose compositions are within the spinodal decay region, is that the growth rate of the epitaxial layers decreases sharply (by almost two orders of magnitude).

We showed earlier[5–7] that when epitaxial layers of GaInAsSb crystallize from Sb-enriched fluxes, the stability of the substrate relative to the liquid phase increases abruptly as a result of the reduced influence of processes associated with nonequilibrium at the GaSb(solid)-[Ga-In-As-

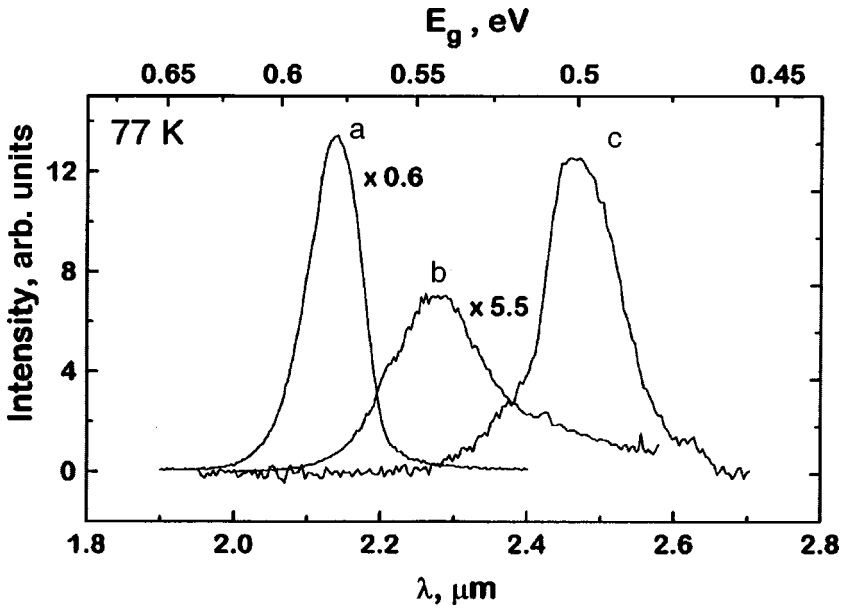

FIG. 1. Photoluminescence spectra ($T=77$ K) of $Ga_{1-x}In_xAs_ySb_{1-y}$ epitaxial layers. a—$x=0.25$, $y=0.21$, $\lambda_{max}=2.14\ \mu$m, $T_g=600$ °C, (100)-oriented substrate, $f_\perp=-7\times10^{-4}$, and thickness of epitaxial layer $d=2\ \mu$m; b—$x=0.32$, $y=0.27$, $\lambda_{max}=2.29\ \mu$m, $T_g=582$ °C, (111)B, $f_\perp=3.2\times10^{-3}$, and $d=4470$ A; c—$x=0.4$, $y=0.36$, $\lambda_{max}=2.46\ \mu$m, $T_g=576$ °C, (111)B, $f_\perp\sim0$, and $d=890$ A.

Sb](liquid) interphase boundary and differences in the lattice parameters. Under conditions of coherent growth we obtained GaInAsSb layers whose crystal quality was at least as good as that of epitaxial GaSb layers on GaSb substrates. We postulate that for liquid-phase compositions even further from equilibrium with GaSb, these characteristics of crystallization from Sb-enriched fluxes combined with the tendency to minimization of energy as a result of the coherent growth (where the lattice mismatch is completely compensated by elastic deformation) will have the result that homogeneous layers crystallize in the range of solid-phase compositions where the calculations indicate spinodal decay. This hypothesis is confirmed by the x-ray diffraction data, secondary ion mass spectroscopy, and photoluminescence measurements.

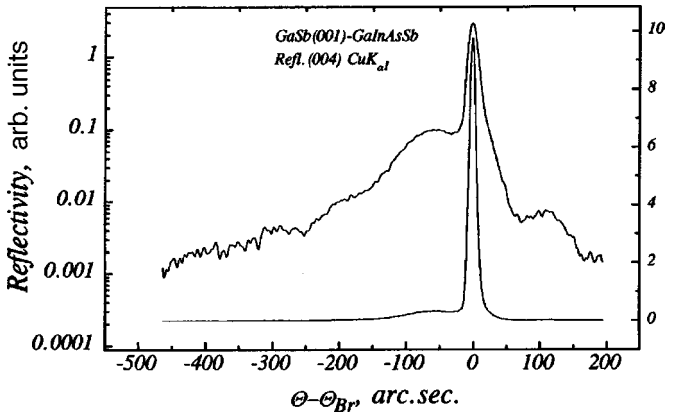

FIG. 2. Diffraction reflection curves for $Ga_{0.7}In_{0.3}As_{0.26}Sb_{0.74}$/GaSb (100) heterostructure.

These results, can now be used to study the reasons for the formation of GaInAsSb epitaxial layers whose compositions lie within the spinodal decay region when the crystallization conditions do not differ appreciably from equilibrium.

The authors would like to thank V. M. Andreev for supporting this work, and also S. Yu. Belova and B. Ya. Bera for making the measurements.

This work was supported by the Russian Fund for Fundamental Research, Project No. 96-02-17864a.

[1] G. B. Stringfellow, J. Cryst. Growth **58**, 194 (1982).
[2] A. N. Baranov, A. A. Guseĭnov, A. M. Litvak, A. A. Popov, N. A. Charykov, V. V. Sherstnev, and Yu. P. Yakovlev, Pis'ma Zh. Tekh. Fiz. **16**(5), 33 (1990) [Sov. Phys. Tech. Phys. **16**, 177 (1990)].
[3] J. C. Dewinter, M. A. Pollack, A. K. Srivastava, and J. L. Zysking, J. Electron. Mater. **14**, 729 (1985).
[4] E. Tournié, J.-L. Lazzari, F. Pitard, C. Alibert, A. Joullié, and B. Lambert, J. Appl. Phys. **68**, 5936 (1990).
[5] V. I. Vasil'ev, V. V. Kuznetsov, and V. A. Mishurnyĭ, Abstracts of Papers presented at Fourth All-Union Conference on Thermodynamics and Materials Science of Semiconductors, Moscow, 1989, Part 1 [in Russian], p. 162.
[6] V. I. Vasil'ev, V. V. Kuznetsov, and V. A. Mishurnyĭ, Izv. Akad. Nauk SSSR, Neorg. Mater. **26**(1), 23 (1990).
[7] V. I. Vasil'ev, V. V. Kuznetsov, V. A. Mishurnyi, V. V. Sazonov, and N. N. Faleev, in *Proceedings of the First International Conference on Epitaxial Growth, Budapest, 1990*, pp. 659–663.

Translated by R. M. Durham

Low-pressure inductive rf discharge in a rare gas-halogen mixture for economical mercury-free luminescence light sources

A. P. Golovitskiĭ

St. Petersburg State Technical University
(Submitted November 26, 1997)
Pis'ma Zh. Tekh. Fiz. **24**, 63–67 (March 26, 1998)

It is demonstrated that an inductive rf discharge in an $Xe+Cl_2$ mixture may be used as the active medium of an efficient, mercury-free luminescence light source. © *1998 American Institute of Physics.* [S1063-7850(98)02903-6]

Recent studies of a dc glow discharge in rare gas-halogen mixtures as sources of ultraviolet radiation have shown that these sources (excilamps) have energy characteristics (ultraviolet output powers of hundreds of watts and efficiencies of 25–30%) quite competitive with those of mercury lamps.[1–5] The main advantage of excilamps is that they are environmentally friendly because they contain no toxic mercury and the halogen content is negligible. However, the main source of environmental contamination does not come from these mercury-containing sources of ultraviolet radiation, produced in small batches for industrial and scientific applications but from the luminescence lamps produced in their millions. It is thus interesting to determine the efficiency of rare gas-halogen mixtures compared to the usual mercury-argon mixtures used in compact luminescence light sources.

The main problems involved in the development of dc excilamps remain their short life[4] caused by chemical bonding between the halogen and the electrode materials, particularly the cathode,[3] and the high voltage (2–7 kV) needed to sustain the discharge. This problem could be solved by using an electrodeless rf discharge where the discharge plasma preferably should not come in contact with the walls, because in an electrodeless discharge in chlorine-containing mixtures, the life is determined by the diffusion of chlorine in the glass, which increases as the glass temperature increases.[6,7]

A suitable method in this respect is the inductive excitation of an rf discharge which incidentally has already been suggested for excimer ultraviolet sources[10] and for mercury luminescence lamps.[8,9]

The experimental system used here was a double-walled S52-2 glass container, open at one end, which was in fact a glass Dewar vessel. Both the outer and inner walls of the container were cylindrical while the bottom was hemispherical. The distance between the outer and inner walls was everywhere ≈ 10 mm. The diameter of the vessel was 50 mm and the height 80 mm. The entire inner surface was coated with a thin layer of the phosphor used in LDS luminescence lamps. The vessel was filled with mixtures of commercially pure xenon and chlorine. A cylindrical single-layer induction coil was placed in the inner cavity of the container, as in Ref. 9. The discharge was excited by a transistor rf generator using a voltage resonance system at a frequency of 13.56 MHz. The use of high-voltage transistors allowed the supply to be taken directly from the 220 V mains. The overall dimensions of the device corresponded to those of a normal incandescent lamp. The device was fitted into a normal E27 lampholder. In all discharge regimes, the energy consumption from the mains was around 9 W. In order to monitor the discharge profile and the ultraviolet radiation intensity, a second vessel was made of uviol glass, having dimensions similar to the first and filled with the same mixture. The generator could be tuned to excite either device. The radiation spectra were recorded using an SDMS diffraction spectrograph fitted with an FÉU-106 photomultiplier and calibrated in absolute units using tungsten (SI10-300) and deuterium (DDS-30) calibration lamps. The signal from the photomultiplier was recorded by a computer. The radiation intensity of the lamp was then converted to normal units of light—lumen.

When the vessel was filled with pure xenon (up to 15 Torr), an H-type discharge was observed.[9,11] The discharge burned as a ring parallel to the turns of the coil in the central part of the vessel. The addition of chlorine caused this ring to spread. If the Xe pressure was less than 3 Torr, the discharge almost uniformly filled the entire inner region of the vessel, including the bottom, clearly forming an *E*-type discharge. The plasma was approximately 1 mm from the walls and the radiation of the rf field was almost shielded by the plasma outside it. This is an advantage over excitation of the discharge by an external inductor,[10] especially as the coil windings do not block off the luminescence.

Preliminary studies carried out using vessels of different shape showed that the vessel described above gives a better luminous efficiency for an $Xe+Cl_2$ discharge compared with the pear-shaped device proposed earlier for mercury lamps.[9]

The luminous efficiency for pure xenon did not exceed a few lumen per watt. Figure 1 gives the luminous flux of the luminescence lamp as a function of the partial pressures of xenon and chlorine. Of the various mixtures studied, the optimum was a mixture of 0.9 Torr Xe and 0.01 Torr Cl_2, for which the total luminous flux was 360 lm (which approximately corresponds to the luminous flux from a 30 W incandescent lamp) for a mains power consumption of 9 W. The luminous efficiency of the lamp was around 40 lm/W. Al-

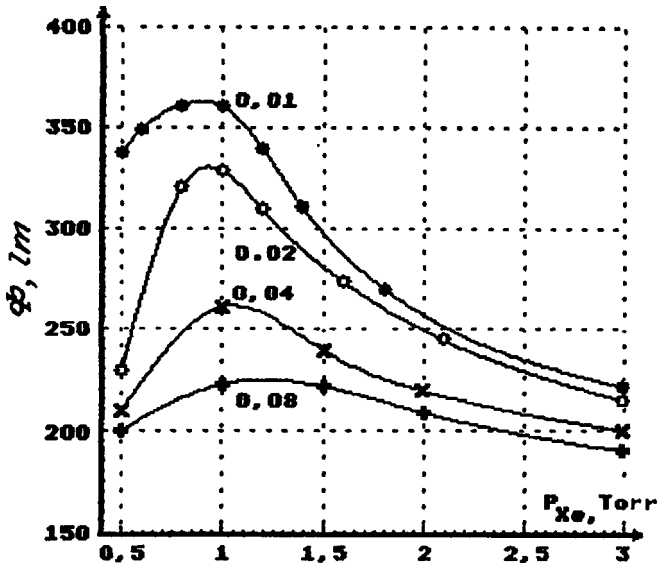

FIG. 1. Luminous flux versus partial xenon pressure. The chlorine partial pressure in Torr is indicated by the numbers on the curves.

though this value is lower than that of modern compact ''economical'' luminescence lamps (60–80 lm/W), it is appreciably higher than that of incandescent lamps, so that this lamp may also be considered to be economical. Figure 1 shows that at chlorine partial pressures below 0.01 Torr, the luminous efficiency could be even higher but unfortunately, the system used here could not accurately measure pressures below 0.01 Torr.

Further optimization of this lamp should involve carefully selecting the gas mixture as well as optimizing the rf generator and using professional phosphor deposition technology. It would be advisable to study $Xe+Br_2$, $Xe+I_2$, and $Kr+Cl_2$ mixtures in these lamps since their ultraviolet radiation spectra with maxima at 282, 253, and 222 nm, respectively, are a better match to the absorption spectrum of the phosphor (optimum for mercury radiation) compared with the spectrum of this $Xe+Cl_2$ mixture, which has a maximum around 308 nm (Ref. 1).

To sum up, it has been demonstrated that economical, compact, mercury-free luminescence light sources can be produced using an inductive rf discharge in rare gas-halogen mixtures.

[1] A. P. Golovitskiĭ, and S. N. Kan, Opt. Spektrosk. **75**, 604 (1993) [Opt. Spectrosc. **75**, 357 (1993)].
[2] A. P. Golovitskiĭ, and S. V. Lebedev, Opt. Spektrosk. **82**, 251 (1997) [Opt. Spectrosc. **82**, 227 (1997)].
[3] A. Schwabedissen and W. Bötticher, Contrib. Plasma Phys. **35**, 517 (1995).
[4] V. F. Tarasenko, M. I. Lomaev, A. N. Panchenko, and E. A. Sosnin, in *Proceedings of the XII International Conference on Gas Discharges and their Applications*, Greifswald, Germany, 1977, Vol. 11, p. 464.
[5] A. N. Panchenko, V. S. Skakun, É. A. Sosnin *et al.*, Pis'ma Zh. Tekh. Fiz. **21**(20), 77 (1995) [Tech. Phys. Lett. **21**, 851 (1995)].
[6] V. I. Svettsov, A. P. Kupriyanovskaya, and A. B. Maryshev, Zh. Prikl. Spektrosk. **35**, 205 (1981).
[7] V. I. Svettsov, A. I. Maksimov, A. P. Kupriyanovskaya, and I. D. Zimina, Élektron. Tekh. Ser. 1. Élektron. SVCh. No. 7, 36 (1977).
[8] A. P. Yushkov, Svetotekhnika No. 2. 23 (1984).
[9] A. M. Troitskiĭ and A. P. Yushkov, Svetotekhnika No. 11, 6 (1984).
[10] P. N. Barnes and M. J. Kushner, J. Appl. Phys. **80**, 5593 (1996).
[11] U. Korsthagen, N. D. Gibson, and J. E. Lawler, J. Phys. D: Appl. Phys. **29**, 1224 (1996).

Translated by R. M. Durham

Deformation defects in polyethylene. Angular dilatons

A. I. Mel'ker and D. V. Solov'ev

St. Petersburg State Technical University
(Submitted November 6, 1997)
Pis'ma Zh. Tekh. Fiz. **24**, 68–71 (March 26, 1998)

Results of calculations of the behavior of a model of a polyethylene molecule under uniaxial compression are illustrated. It is observed that as the deformation increases, the fraction of valence angles between the carbon atoms increases. This molecular configuration possesses stability and has been described by the authors as an ''angular dilation.'' © *1998 American Institute of Physics.* [S1063-7850(98)03003-1]

The concept of defects is widely used in macromolecular physics to explain the properties of polymers but ideas on the microscopic structure of these defects are still at the speculative stage.[1,2] Some progress in this field has been achieved by using dynamic computer modeling using fairly simple two-dimensional polymer models.[3–6] The question remains as to how the defects observed in two-dimensional computer models relate to those found in real three-dimensional polymers.

Here we investigate the three-dimensional atomic structure of a polyethylene macromolecule during compression. The initial globular macromolecule consisted of 500 CH_2 units. The method of obtaining an equilibrium polymer globule, the interatomic interaction potential, and also the computer modeling technique were analyzed in detail in Refs. 7 and 8. This globule was inserted between two hard parallel plates which moved at toward each other at constant velocity.

In order to understand the nature of the deformation of the polymer globule, we considered the evolution of the pair correlation functions for different groups of atoms (see Fig. 1). We shall denote these functions by the following symbols:

$$\text{C(–C–)C}, \quad \text{H(–C–)C}, \quad \text{H(–C–)H}, \quad \text{C(–C–C–)C}. \qquad (1)$$

Here the outermost symbols correspond to the atoms for which the pair correlation function is calculated while the symbols in parentheses indicate the spatial path of the covalent bonds joining the atomic pairs.

Figure 1 shows that the C(–C–)C pair correlation function undergoes the largest variation. This function initially consists of two peaks where the center of gravity of the first (broadened) peak at 0.251 nm corresponds to an equilibrium state between its second carbon neighbors in an ideal zigzag rectilinear chain. The second (sharp) peak at ~ 0.3 corresponds to an approximately 20% increase in the valence angle between the C–C bonds. As the deformation increases, the fraction of bonds with an increased valence angle between them increases and by the end of the process, almost all the valence angles are extended.

Measurements of the C–(–C–C–)–C pair correlation function also indicate that the zigzag chain becomes partially straightened and the extended zigzags tend to lie in the same plane.

These results may be explained as follows. It has already been shown that in extended anharmonic chains of atoms

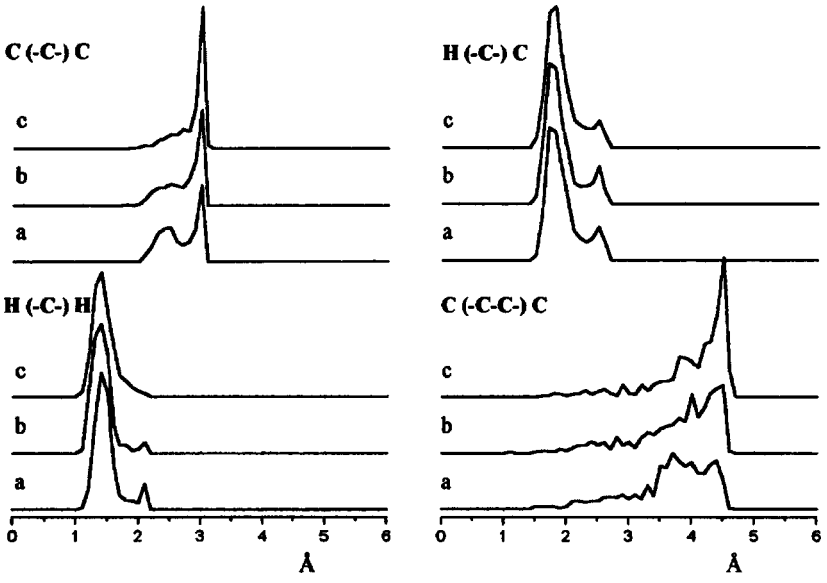

FIG. 1. Variation of the pair correlation functions for different types of pairs of atoms during deformation of a polymer globule (for explanation see text). Curves *a* correspond to the beginning of the process while curves *b* and *c* correspond to the intermediate and final stages of deformation, respectively.

there is a metastable (static[9] and dynamic[10]) atomic configuration in which one of the interatomic spacings is considerably greater than the others by a specific amount. These anomalously extended bonds, which have been called dilatons,[11] play the role of static and dynamic defects in deformed one-dimensional, quasi-one-dimensional, and even two-dimensional discrete models of solids.[3,4,12–14]

In the case of polyethylene we are dealing with extended valence angles. Mathematically, this is equivalent to the formation of anomalously extended bonds between carbon atoms not positioned at the vertex of the valence angle so that the deformation defects observed by us may be called angular dilatons.

[1] B. Wunderlich, *Macromolecular Physics* (Academic Press, New York, 1973; Mir, Moscow, 1996).
[2] G. M. Bartenev, *Strength and Mechanics of Damage to Polymers* [in Russian], Khimiya, Moscow (1984).
[3] A. I. Mel'ker and A. V. Ivanov, Fiz. Tverd. Tela (Leningrad) **29**, 1556 (1987) [Sov. Phys. Solid State **29**, 893 (1987)].
[4] A. I. Mel'ker, A. V. Ivanov, and S. V. Govorov, Mekh. Kompozit. Mater. **6**, 1007 (1988).
[5] A. I. Mel'ker, A. V. Ivanov, T. V. Vorob'eva, and S. N. Romanov, Fiz. Tverd. Tela (St. Petersburg) **38**, 2558 (1996) [Phys. Solid State **38**, 1403 (1996)].
[6] A. I. Melker, A. V. Ivanov, and S. N. Romanov, *Computer Modelling of Electronic and Atomic Processes in Solids*, edited by R. C. Tennyson and A. E. Kiv, NATO ASI. Series 3, High Technology, Vol. 22 (Kluwer Academic Publishers, Boston, 1977), p. 97.
[7] D. V. Solov'ev, *Application of the Molecular Dynamics Method to Study the evolution of Macromolecular Structures*, Master's Thesis [in Russian], St. Petersburg State Technical University, St. Petersburg (1995).
[8] D. V. Solov'ev, in *Nondestructive Testing and Computer Simulations in Materials Science and Engineering*, Abstracts of Papers Presented at International Workshop on New Approaches to Hi-Tech Materials, St. Petersburg, 1997.
[9] A. N. Orlov, Yu. M. Plishkin, and I. M. Shepeleva, Fiz. Met. Metalloved. **4**, 540 (1957).
[10] A. I. Mel'ker and T. E. Kuznetsova, Fiz. Tverd. Tela (Leningrad) **22**, 3336 (1986) [*sic*].
[11] A. I. Mel'ker, Fiz. Tverd. Tela (Leningrad) **28**(11), 3396 (1986) [Sov. Phys. Solid State **28**, 1912 (1986)].
[12] A. I. Mikhaĭlin and A. I. Mel'ker, Khim. Fiz. **4**, 15.
[13] A. V. Ivanov and A. I. Mel'ker, Fiz. Tverd. Tela (Leningrad) **28**, 3637 (1986) [Sov. Phys. Solid State **28**, 2050 (1986)].
[14] E. Ya. Baiguzin, A. I. Melker and A. I. Mikhailin, Phys. Status Solidi A **108**, 205 (1988).

Translated by R. M. Durham

Influence of an auxiliary planar short-circuited *p-n* junction positioned near a main junction

V. P. Astakhov, D. A. Gindin, and V. V. Karpov

''Sapfir'' Factory, Moscow
(Submitted October 13, 1997)
Pis'ma Zh. Tekh. Fiz. **24**, 72–76 (March 26, 1998)

A possible method of reducing the reverse currents and increasing the forward currents in small-scale planar diodes is discussed and demonstrated experimentally. This method involves using an auxiliary short-circuited planar $p-n$ junction positioned within the diffusion length of minority carriers from the planar boundaries of the diodes. © *1998 American Institute of Physics.* [S1063-7850(98)03103-6]

In some types of planar semiconductor devices such as small-scale diodes, *pin* diodes, transistors, and their corresponding optical radiation detectors, it is advisable to form regions, which have an infinitely high minority carrier recombination velocity and do not actually generate carriers, near $p-n$ junctions which perform different functions (including rectification, detection, photocarrier collection, separation of carriers in the collector of a transistor, and so on). These regions may be auxiliary, planar, short-circuited $p-n$ junctions whose topology depends on the particular applications of the main $p-n$ junctions and their topology. According to Ref. 1, an auxiliary ribbon short-circuited $p-n$ junction encircling an array of small-scale indium antimonide photodiodes fulfills two functions: it confines the region of photocarrier collection and ''extinguishes'' explosive background noise.[2]

An auxiliary $p-n$ junction positioned within the diffusion length of the main junction may ''draw off' some of the equilibrium minority carriers which are generated near or at the edge of the main $p-n$ junction and contribute to its excess current. Thus, especially when the main $p-n$ junction has a low area-to-perimeter ratio, an auxiliary $p-n$ junction can substantially reduce the dark current of the main junction when reverse biased, which is always desirable for any type of device and especially for low-background photodetectors and low-noise detectors. A positive effect may be predicted in the absence of surface channels, which can be achieved for silicon by using initial n-type crystals.

The possibility of reducing the excess currents by using an auxiliary short-circuited $p-n$ junction was confirmed by the following experiment. We fabricated arrays of planar diodes using n-type epitaxial silicon films 20 μm thick with a resistivity of 8 $\Omega\cdot$cm by boron ion implantations across an SiO_2 film. The topology of the experimental array (Fig. 1a) comprises a series of main $p-n$ junctions having dimensions of 300 μm (along the array) and 700 μm (perpendicular to the array), bordered by an auxiliary short-circuited $p-n$ junction 200 μm wide, located at a distance of 300 μm from the longitudinal edges of the areas. This distance is greater than the width of the space charge region of the $p-n$ junction at 100 V and is between three and four times smaller than the hole diffusion length in the n-base. An auxiliary $p-n$ junction 10 μm wide also passes between the areas, which are 30 μm apart. The control arrays (Fig. 1b) had no auxiliary $p-n$ junction.

The reverse branches of the current-voltage characteristics of the individual diodes and of the experimental arrays typically showed a high degree of similarity, whereas for the control arrays, the spread of currents was around an order of magnitude.

Figure 2a gives the reverse branches of the current-voltage characteristic for the worst area of the experimental arrays and the best of the control arrays. This shows that for the selected area-to-perimeter ratio of the main $p-n$ junction (10^{-2} Ω) and relative position of the main and auxiliary $p-n$ junctions, the auxiliary $p-n$ junction reduces the reverse currents of the main junction by a factor of three at

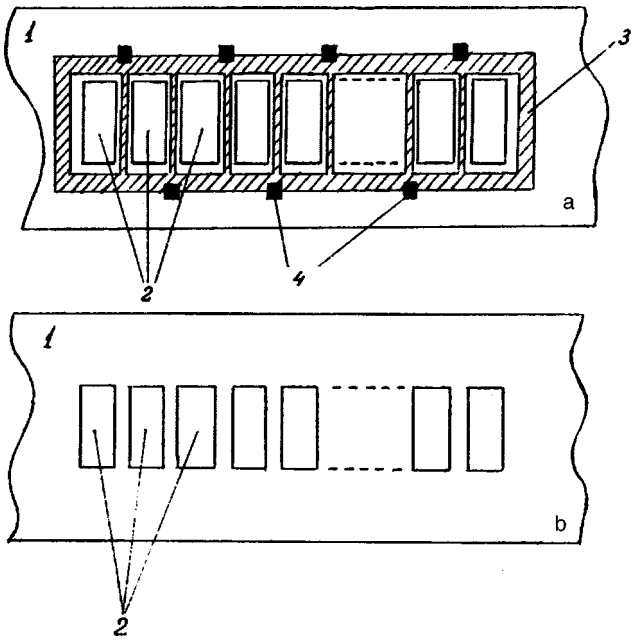

FIG. 1. Topology of experimental (a) and control (b) diode arrays: *1*—initial crystal, *2*—areas of main $p-n$ junctions (p^+ regions), *3*—auxiliary $p-n$ junction (p^+ region), and *4*—metallized sections short-circuiting auxiliary $p-n$ junction.

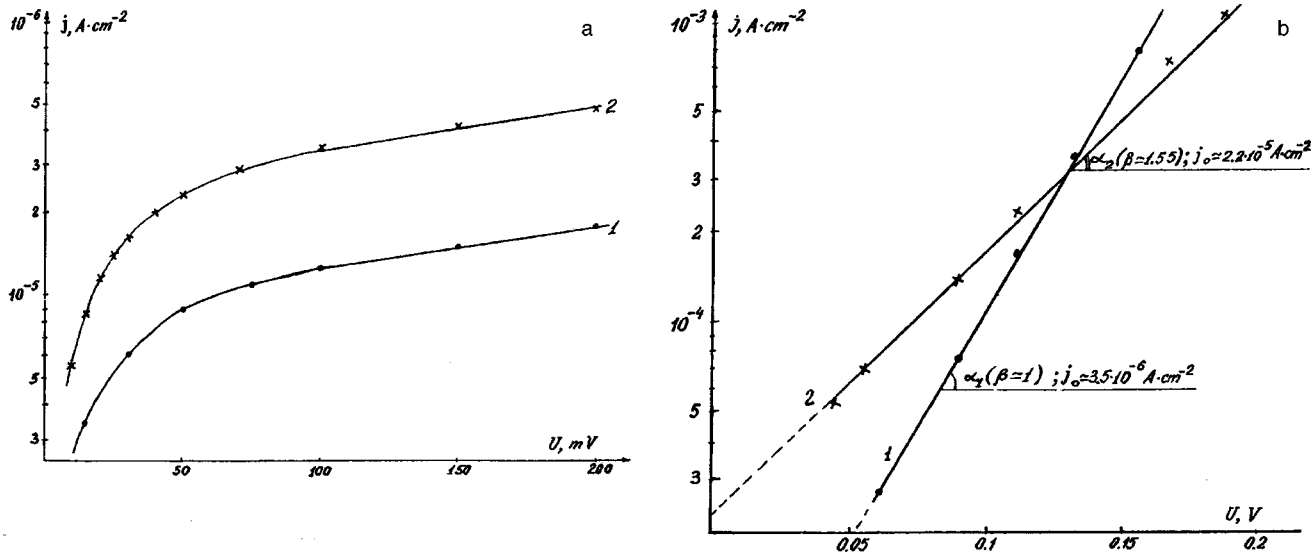

FIG. 2. Reverse (a) and forward (b) branches of the current-voltage characteristic of main $p-n$ junction in experimental (*1*) and control (*2*) arrays.

voltages above 30 mV. In both cases, the current-voltage characteristics show a fairly high degree of correspondence with the Shockley–Noyce–Sah theory[3] since at voltages above 20 mV they are approximated by the expression $I=kU^{\alpha}$ with similar exponents, close to 0.5 ($\alpha=0.545$). All these factors indicate that the auxiliary $p-n$ junction has the same confining effect on the minority carrier collection area at all bias voltages. Breakdown of the areas in the experimental and control arrays is reversible, has an avalanche character, and takes place at the same (60 V) voltage.

The auxiliary $p-n$ junction also influences the forward branch of the current-voltage characteristic of the small-scale area of the main $p-n$ junction (Fig. 2b), reducing the saturation current (j_0) almost tenfold and reducing the ideality factor β in the expression $j=j_0\cdot\exp(eU/(\beta kT))$ from 1.55 for the control arrays to 1.0. This effect is caused by an increased diffusion flux of holes injected into the base toward the auxiliary $p-n$ junction as the forward bias (injection level) is increased. The forward current in the experimental arrays exceeds that in the control arrays up to biases above 1 V.

To sum up, an auxiliary short-circuited $p-n$ junction reduces the reverse currents and increases the forward currents in small-scale diodes. This influence of the auxiliary $p-n$ junction will obviously increase when the area-to-perimeter ratio of the diode area is further reduced.

[1] V. P. Astakhov, S. V. Varganov, L. V. Demidova, V. F. Dudkin, V. P. Ezhov *et al.*, Russian Patent No. RF 1589963.
[2] V. P. Astakhov, V. F. Dudkin, B. S. Kerner, V. V. Osikov, O. V. Smolin, and I. I. Taubkin, Mikroelektronika **18**, 455 (1989).
[3] W. Shockley, R. Noyce, and C. Sah, Proc. IRE **45**, 1228 (1957).

Translated by R. M. Durham

Influence of pumping uniformity on current tuning of the emission wavelength of InAsSb/InAsSbP diode lasers

T. N. Danilova, O. I. Evseenko, A. N. Imenkov, N. M. Kolchanova, M. V. Stepanov, V. V. Sherstnev, and Yu. P. Yakovlev

A. F. Ioffe Physicotechnical Institute, Russian Academy of Sciences, St. Petersburg
(Submitted October 30, 1997)
Pis'ma Zh. Tekh. Fiz. **24**, 77–84 (March 26, 1998)

An investigation was made of continuous tuning of the emission wavelength in two types of InAsSb/InAsSbP diode heterolasers: three-layer structures with combined electrical and optical confinement and five-layer structures with separate confinement. In three-layer structures the emission wavelength initially decreases by 2–4 Å with increasing current and then increases by 10–15 Å. In five-layer structures the emission wavelength mainly decreases. This difference is attributed to the better flow of carriers in the bulk of the active region in five-layer structures as compared with three-layer ones. © *1998 American Institute of Physics.*
[S1063-7850(98)03203-0]

1. Diode laser structures made of narrow-gap materials have emission lines in that part of the spectrum which contains closely spaced absorption lines of many natural and industrial gases. Thus, continuously tunable instantaneous-response diode lasers may have applications in high-resolution laser spectroscopy. They may also be used in optical communications since they can frequency modulate an optical signal.

The desired continuous tuning of the emission wavelength has been observed in lasers with a narrow-gap InAsSb layer and InAsSbP confining layers, using both three-layer structures with combined electrical and optical confinement[1–4] and five-layer structures with separate confinement.[5]

Tuning was observed both during the current pulse[1,2] and also when varying the pump current.[3,4] In Ref. 4, tuning was observed at a rate exceeding the thermal relaxation rate. For excesses above the threshold less than 5–40%, the emission wavelength decreases with current whereas at higher excesses, it increases. The reduction in the wavelength is caused by an increase in the concentration of nonequilibrium carriers, while the increase in wavelength is caused by self-focusing of the radiation.

The aim of the present study is to determine the influence of changes in the carrier concentration and the spatial distribution of the radiation in a diode laser. For this purpose we compared the characteristics in three- and five-layer structures where the uniformity of the pumping differs substantially and thus the uniformity of the carrier distribution also differs.

2. The method of fabrication and the main electrical characteristics were described in Refs. 1 and 5. Figure 1 shows the layer configuration in the laser structure (*1*) and the layer-by-layer distribution of the band gap (*2*) in three-layer (a) and five-layer (b) structures. It should be stressed that the equilibrium carrier concentration in the narrow-gap region and its band gap E_g were the same in both types of structure. The parameters of the wide-gap confining layers were also the same. The five-layer structures differed from the three-layer ones only in that they had layers 0.5–0.7 μm thick with an intermediate value of the band gap on both sides of the narrow-gap region. These lasers had a cavity length of 300–400 μm and a stripe width of 18–20 μm.

Structures of this type were used to study the spectral composition of the radiation and the angular distribution of the laser radiation in the plane of the $p-n$ junction, and were used for current tuning of the lasing wavelength within a single mode in the red and the blue.[4,5] The frequency tuning was measured by passing the radiation through an external cavity with a variable optical length. The laser was supplied by a direct current on which was superposed a sawtooth-increasing current pulse. The direct current was set equal to the threshold current I_{th}. The amplitude of the sawtooth current was calculated so that for all values of this current I the laser operated in a single preferred mode. Both structures were investigated in the temperature range 77–90 K.

3. The results are as follows. The laser wavelength at 77 K was in the range 3.2–3.4 μm. In both types of structure where the lasers were supplied by sawtooth current pulses (Fig. 2a), the radiation transmitted by the external cavity was also sawtoothed and sinusoidally modulated (Figs. 2b and 2c). The shape of the radiation pulses did not depend on the repetition frequency of the sawtooth pulse up to frequencies of hundreds of kilohertz. The modulation is caused by the variation of the laser frequency as it runs through the natural frequencies of the external cavity. For both structures an increase in the optical length of the external cavity causes the waves to disperse from a certain point (the point of zero shift) on the radiation pulse (Fig. 2). This indicates that the lasing wavelength decreases with increasing current at levels below those corresponding to this point (blue shift) and increases at higher currents (red shift). For three-layer structures (Fig. 3a, curve *1*), the point of zero wavelength shift corresponds to a 5–40% excess current above the threshold. As the current I increases further, the blue shift is replaced by a red shift. In five-layer structures (Fig. 3a, curve *2*) a

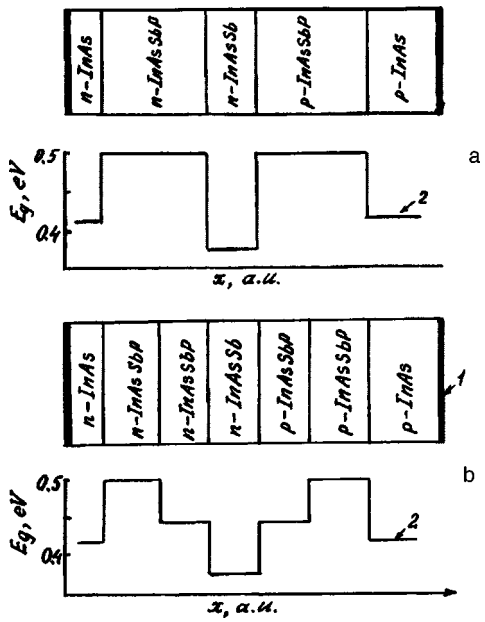

FIG. 1. Schematic of layer configuration in laser structure (*1*) and layer-by-layer distribution of band gap (*2*) in three-layer (a) and five-layer (b) structures.

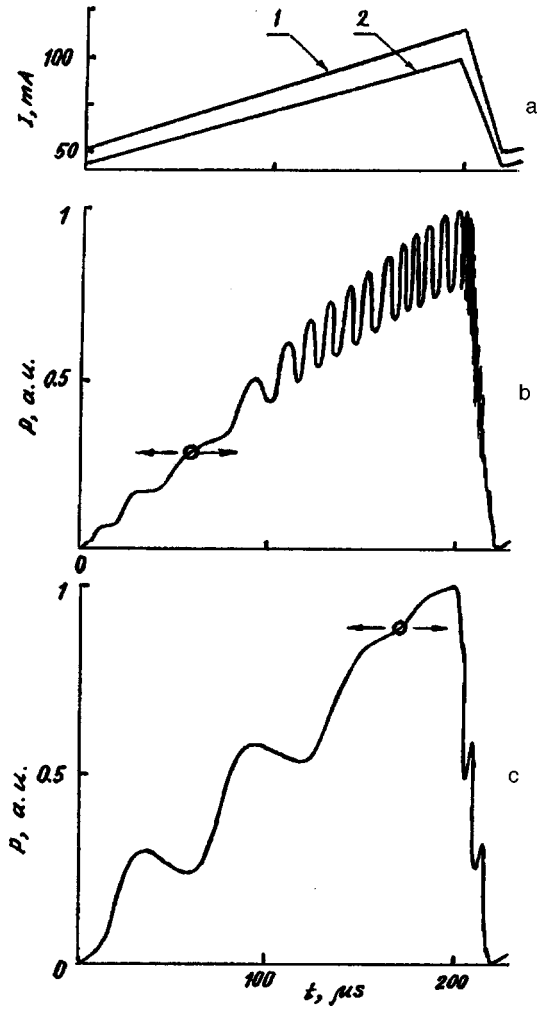

FIG. 2. Oscilloscope trace of supply current (a) for three-layer structure (*1*) and five-layer structure (*2*). Laser radiation intensity transmitted by external Fabry–Perot cavity for three-layer structure (a) and five-layer structure (b).

blue shift predominates up to high currents ($I \geqslant 1.8I_{\text{th}}$) and is only replaced by a red shift at currents around $2I_{\text{th}}$. In practice, only the blue shift can be clearly observed in five-layer structures since an increase in current beyond twice the threshold switches the laser to a different mode. In three-layer structures (Fig. 3a, curve *1*) the emission wavelength initially decreases by 2–4 Å and then increases by 10–15 Å. In five-layer structures (Fig. 3a, curve *2*) a decrease in the wavelength by 4–5 Å predominates.

As the current increases above the threshold in five-layer structures, the half-width of the angular distribution (Fig. 3b, curve *2*) remains almost constant for $2I_{\text{th}} > I > I_{\text{th}}$ and is 10–12°. In three-layer structures (Fig. 3b, curve *1*), the half-width also varies negligibly and remains the same up to 40% excess of the current over the threshold and then increases, reaching 20° at $I = 2I_{\text{th}}$. A clear correlation is observed between the variation of the angular distribution and the variation of the lasing wavelength. While the angular distribution does not change with current, the lasing line shows a short-wavelength shift with increasing current but as the angular distribution becomes broader, the emission line is shifted in the long-wavelength direction.

This behavior is observed at temperatures between 77 and 90 K. However, as the temperature increases, the range of variation of the emission wavelength with current decreases because the laser operating interval in the single-mode regime decreases.

An investigation of the laser radiation in two types of structures whose only difference is that they have or do not have layers between the active region and the optical confining layers having a wider gap than the active region and a narrower gap than the optical confining layers, yields three conclusions:

— A characteristic feature of the variation of the laser wavelength with increasing current is that it initially decreases and then increases.

— In three-layer structures the decrease is replaced by an increase at currents 5–40% above the threshold whereas in five-layer structures it is 80–100%.

— The rate of response to changes in current exceeds the thermal relaxation rate.

4. We shall analyze the experimental results. An almost instantaneous-response decrease in the laser wavelength with current was attributed in Ref. 4 to an increase in the carrier concentration, while its subsequent increase was attributed to self-focusing of the radiation with corresponding changes in the refractive index. The existence of self-focusing is confirmed by the broadening of the angular distribution.

In fact, the increase in the number of layers, with a corresponding decrease in the height of the heterobarriers between them in five-layer structures as compared with three-layer ones, should increase the flow of carriers in the bulk of the active region and equalize their concentration. In this case, the pumping rate increases slightly at those points where more radiation is generated. The variation of the refractive index over the stripe width caused by variation of

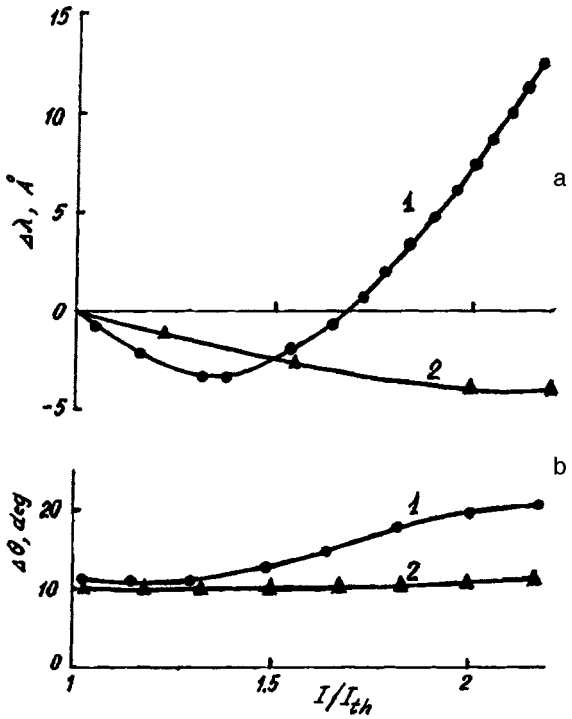

FIG. 3. Variation of the laser wavelength Δλ (a) and the half-width of the angular distribution ΔΘ (b) as a function of the ratio of the current to the threshold I/I_{th} at liquid-nitrogen temperature for three-layer (*1*) and five-layer (*2*) structures.

the radiation density and its dependence on the current are strongly suppressed. In three-layer structures however, the pumping rate is more independent of the radiation density. Since at fixed pump density an increase in the radiation intensity leads to a decrease in the carrier concentration, the coordinate dependence of the refractive index and its variation with current, which are directly related to the carrier concentration, should have a maximum in structures where the pump density does not depend on the laser radiation intensity. This condition is probably satisfied more easily in three-layer structures. As a result, a decrease in the wavelength is observed with current which is then replaced by an increase at relatively small excesses over the threshold, followed by a further substantial increase in the wavelength.

In principle, the improved flow of nonequilibrium carriers in the bulk of the active region should not significantly influence the range of variation of the wavelength, either decreasing or increasing the wavelength, but should reduce its dependence on the current. This circumstance can probably explain why the variations of the wavelength in the short-wavelength direction are the same in five-layer and three-layer structures and why the current at which the decrease is replaced by an increase is higher in five-layer structures than in three-layer ones (Fig. 3a).

To sum up, studies of laser wavelength tuning in two types of structures, whose only difference is that they have or do not have intermediate layers between the narrow-gap active region and the wide-gap confining regions, have shown that nonlinear optical effects caused by the coupling between the refractive index and the laser radiation intensity and pump uniformity play an important role in the nature of this tuning.

This work was partly supported by a grant from the Ministry of Science of the Russian Federation under the program ''Optics and Laser Physics'' and partly by INCO-Copernicus, Contract No. PL965093.

[1] A. N. Baranov, T. N. Danilova, O. G. Ershov, A. N. Imenkov, V. V. Sherstnev, and Yu. P. Yakovlev, Pis'ma Zh. Tekh. Fiz. **18**(22), 6 (1992) [Sov. Tech. Phys. Lett. **18**, 690 (1992)].
[2] Yu. P. Yakovlev, A. N. Baranov, A. N. Imenkov, V. V. Sherstnev, E. V. Stepanov, and A. Ya. Ponurovskiĭ, Kvantovaya Élektron. (Moscow) **20**, 839 (1993) [Quantum Electron. **23**, 726 (1993)].
[3] A. N. Baranov, A. N. Imenkov, V. V. Sherstnev, and Yu. P. Yakovlev, Appl. Phys. Lett. **64**, 2480 (1994).
[4] T. N. Danilova, O. I. Evseenko, A. N. Imenkov, N. M. Kolchanova, M. V. Stepanov, V. V. Sherstnev, and Yu. P. Yakovlev, Pis'ma Zh. Tekh. Fiz. **22**(16), 7 (1996) [Tech. Phys. Lett. **22**, 645 (1996)].
[5] T. N. Danilova, O. I. Evseenko, A. N. Imenkov, N. M. Kolchanova, M. V. Stepanov, V. V. Sherstnev, and Yu. P. Yakovlev, Fiz. Tekh. Poluprovodn. **31**, 662 (1997) [Sov. Phys. Semicond. **31**, 563 (1977)]

Translated by R. M. Durham

Preparation of thin films of new $ZnGa_2S_4$ wide-gap semiconductors

N. I. Popovich, N. I. Dovgosheĭ, and I. É. Kacher

Uzhgorod State University, Ukraine
(Submitted September 30, 1997)
Pis'ma Zh. Tekh. Fiz. **24**, 85–87 (March 26, 1998)

An investigation was made of a possible method of obtaining thin films of new $ZnGa_2S_4$ semiconductors by pulsed laser deposition and quasi-equilibrium deposition from a Knudsen cell. It was established that these films are transparent in the range 0.3–26 μm, their band gap is 3.79 eV, and the refractive index in the region of transparency is 2.19. © *1998 American Institute of Physics.* [S1063-7850(98)03303-5]

A possible method of obtaining films of new complex $ZnGa_2S_4$ semiconductors by pulsed laser deposition and quasi-equilibrium deposition from a Knudsen cell has been studied.

Compounds of $ZnGa_2S_4$ have wide regions of transparency, high optical strength, high photosensitivity, and high-intensity ultraviolet luminescence.[1,2] The widespread application of these materials is impeded by the difficulties involved in obtaining pure, perfect single crystals of the required dimensions so that it is promising to use these compounds as films. In addition, by studying the main physical properties of the films, it will be possible to predict data on the parameters of the single crystals not available in the literature.

Here we aim to develop the technological conditions required to produce $ZnGa_2S_4$ films and to study their influence on the optical properties of these films.

Thin films of $ZnGa_2S_4$ were prepared by pulsed laser deposition and also by quasi-equilibrium deposition from a Knudsen cell. Pulsed laser deposition was carried out using the free-running and giant-pulse modes of a LTIPCh-7 laser on quartz and NaCl substrates. Results of calculations of the formation of a monolayer $ZnGa_2S_4$ film on a substrate surface using semiempirical MO LCAO methods were taken into account.[3] A polycrystalline zinc thiogallate charge was synthesized by fusing stoichiometric quantities of elementary Zn, Ga, and S components in vacuum quartz ampoules.[4] The film condensates were studied by local x-ray spectral analysis using MS-46 and ISM-35SF microanalyzers and a IEOL LINK spectrometer at the L. Ya. Karpov Institute (Moscow). The optical properties of the $ZnGa_2S_4$ films were investigated in the fundamental absorption region using an SF-26 spectrophotometer and in the infrared, using an IKS-29 spectrophotometer.

Films of $ZnGa_2S_4$ 0.5–0.7 μm thick were obtained on NaCl and quartz substrates by quasi-equilibrium deposition from a Knudsen cell.

Investigations of the composition of the zinc thiogallate laser condensates reveal that near-stoichiometric films are obtained at low substrate temperatures in the giant pulse mode at 73 K. As the substrate temperature increases, the films become depleted in zinc.

The optical parameters of $ZnGa_2S_4$ were studied in the spectral range 0.3–30 μm. It was established that these films are transparent in the range 0.3–26 μm. The refractive index for $ZnGa_2S_4$ in the region of transparency is 2.19 and the band gap 3.79 eV. The fundamental absorption edge is approximated by a dependence typical of direct allowed transitions.

The preparation of $ZnGa_2S_4$ by discrete thermal evaporation encountered various technological difficulties such as severe spurious heating of the substrate and sputtering of powdery zinc thiogallate.

To sum up, thin films of a new wide-gap semiconductor $ZnGa_2S_4$, transparent in the range 0.3–26 μm with a band gap of 3.79 eV and a refractive index of 2.19 in the transparent range, have been obtained for the first time. It has been established that pulsed laser evaporation is the most promising method of obtaining high-quality $ZnGa_2S_4$ films.

[1] A. N. Georgobiani, S. I. Radautsan, and I. M. Tiginyanu, Fiz. Tekh. Poluprovodn. **19**, 192 (1985) [Sov. Phys. Semicond. **19**, 121 (1985)].
[2] N. A. Goryunova, *Complex Diamond-Like Semiconductors* [in Russian], Sovet-skoe Radio, Moscow (1968), 268 pp.
[3] N. Popovich, N. Dovgoshey, V. Zhikharev, and I. Kacher, Abstracts of Papers Presented at the 10th International Conference on Thin Films; 5th European Vacuum Conference, Madrid, 1996, p. 84.
[4] M. Yu. Rigan and N. P. Stasyuk, *Preparation and Properties of Complex Semiconductors* [in Russian], UMK VO, Kiev (1991), pp. 62–69

Translated by R. M. Durham

Long-wavelength uncooled sources of $\lambda = 5-6$ μm radiation using graded-index InAsSb(P) layers grown by liquid-phase epitaxy

M. Aĭdaraliev, N. V. Zotova, S. A. Karandashev, B. A. Matveev, M. A. Remennyĭ, N. M. Stus', and G. N. Talalakin

A. F. Ioffe Physicotechnical Institute, St. Petersburg

Pis'ma Zh. Tekh. Fiz. **24**, 88–94 (March 26, 1998)

Graded-index $p-n$ InAsSb/InAsSbP/InAs structures capable of emitting at the maximum of the spectral curve up to 5.4 μm with a half-width of ~ 26 meV (~ 0.6 μm) without cooling have been fabricated and studied. This is the longest-wavelength radiation obtained at room temperature in III–V structures grown by liquid-phase epitaxy and the band is the narrowest obtained for semiconductor spontaneous radiation sources. © *1998 American Institute of Physics.* [S1063-7850(98)03403-X]

Materials and heterostructures capable of emitting at wavelengths $\lambda > 5$ μm at room temperature are currently being intensively studied. Light-emitting diodes in this range have applications in spectroscopy, gas analysis, and communications.

Many researchers have been concentrating their efforts on studying the capabilities of III–V materials since these possess high thermal conductivity and metallurgical stability compared with II–VI and IV–VI systems. The authors of Ref. 1 reported the development of an InSb/$In_{1-x}Al_xSb$ light-emitting diode with a half-width of >1 μm ($\lambda = 5.5$ μm), which is not optimum for many applications in spectroscopy, using molecular-beam epitaxy. Recently, molecular-beam epitaxy was also used to produce quantum-cascade light-emitting diodes in the range 5–8 μm (Ref. 2), but these cannot operate in the cw mode.

An alternative is offered by heterostructures containing an InAsSb solid solution having a band gap between 350 and ~ 100 meV (300 K). However, because of the lack of a binary substrate lattice-matched with InAsSb of the required composition, intermediate (transition) layers of the required composition must be grown between the substrate and the working layer,[3] or strained superlattices must be produced.[4] In the first case, the wavelengths at the band maximum did not exceed $\lambda = 4.4$ μm whereas in the second case, the light-emitting diodes had a half-width >1 μm (300 K).

Earlier,[5] we proposed a method of obtaining InAsSb solid solutions with a low dislocation density ($N < 10^4$ cm^{-2}) and an Sb content which increases toward the surface. The method involves growing a graded-index InAsSbP layer by liquid-phase epitaxy under conditions where the InAs substrate exhibits high plasticity so that the mismatch stresses relax by preferential formation of dislocations in the substrate, accompanied by bending. This method was used to fabricate light-emitting diodes having maxima of the electroluminescence spectra at 4.3 and 4.7 μm and half-widths not exceeding 0.5 μm (300 K) (Ref. 6), which were used in sensors for carbon dioxide and carbon monoxide, respectively.[7] This method was also used to produce narrow-gap $InAs_{0.46}Sb_{0.54}$ layers with an abrupt optical absorption edge at 90 meV (300 K). So far, however, this method has not been used to fabricate $p-n$ structures emitting at $\lambda > 4.8$ μm (300 K).

The aim of the present study is to investigate the mechanisms responsible for radiative recombination in InAsSb/InAsSbP/InAs heterostructures fabricated by liquid-phase epitaxy under conditions of high substrate plasticity and to develop uncooled radiation sources emitting at 5–6 μm.

First, $InAs_{1-x}Sb_x$(Zn)/InAsSbP/InAs heterostructures (inset to Fig. 1) were grown by liquid-phase epitaxy at temperatures of 630–680 °C on n-InAs(111) substrates with an electron concentration of $\sim 2\times 10^{16}$ cm^{-3}. The $p-n$ junction was created during growth of the Zn-doped InAsSb layer in a purified hydrogen atmosphere. The density of inclined dislocations in the surface layer did not exceed 5×10^4 cm^{-2}. Most of the dislocations caused by mismatch between the lattice parameters of the substrate and the solid solution were located in the substrate and at the InAs/InAsSbP interface, far from the $p-n$ junction and the emitting region.

The photo- and electroluminescence was recorded with a cooled InSb photodiode using a synchronous detection system. The photoluminescence was excited using an LPI-14 GaAs diode laser ($\lambda = 0.8$ μm, $P_{\text{puls}} \sim 10$ W ($\tau = 5$ μs, $f = 500$ Hz)) whose radiation was directed onto the narrow-gap InAsSb layer in a reflection geometry. For the electroluminescence measurements we pricked out $0.5\times 0.5\times 0.2$ mm samples which were mounted with the narrow-gap InAsSb layer at the base of the holder. Current leads were soldered to the crystal with indium and the radiation was coupled out via the InAsSbP layer and the InAs substrate.

Figure 1 shows photoluminescence spectra (77 K) for structures whose narrow-gap surface p-layer has the composition $x_1 = 0.1$ (No. 1-218(5)) and $x_2 \sim 0.2$ (No. 2-232(2)), which will subsequently be called samples Nos. 1 and 2, respectively. The photoluminescence intensity in the narrower-gap solid solution ($x_2 \sim 0.2$) is five times lower than that for the $x_1 = 0.1$ composition, which is consistent

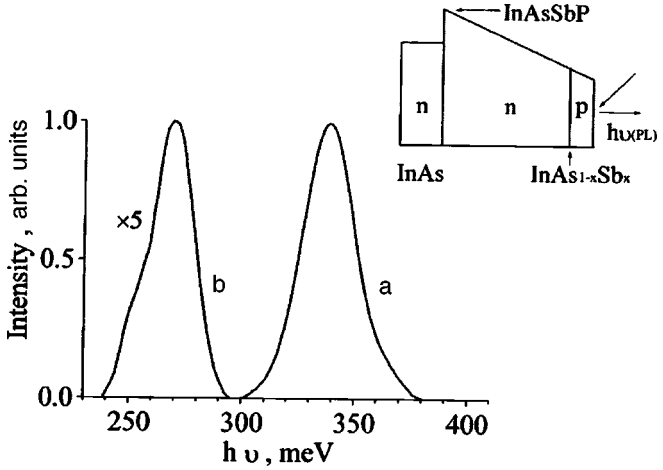

FIG. 1. Photoluminescence spectra (77 K) of structures No. 1 (a) and No. 2 (b).

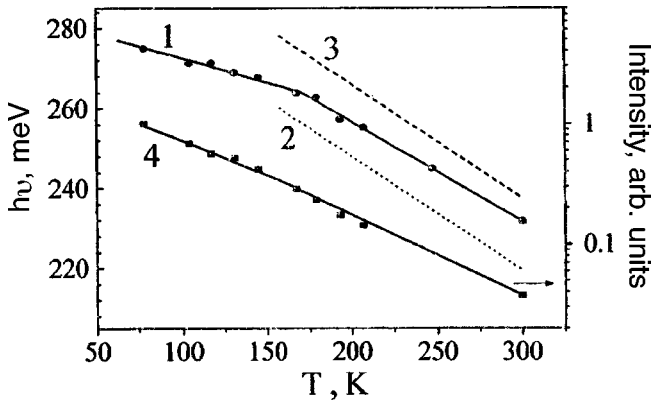

FIG. 3. Temperature dependences of the maximum energy (curve 1) and intensity (curve 4) of the electroluminescence for structure No. 2, $E_g(T) = h\nu_{max}(T) - kT/2$ (curve 2), $E_g(T) = E_g(0) - 2.85\times10^{-4}\times T$ meV ($E_g(0)$—fitting parameter) (curve *3*).

with the data given in Ref. 8. The characteristic energy of the short-wavelength trailing edge $\varepsilon_0 \sim 10$ meV is close to the thermal energy kT at 77 K, which indicates that these layers possess good structural quality. Thus, the large half-width ($\sim$26 meV) is probably attributable to the involvement of two mechanisms in the radiative recombination: band-band and band-acceptor.

Figure 2a gives the current-voltage characteristics at 77 and 300 K. It can be seen that as the antimony content increases, the cutoff voltage decreases from $U_{cut} = 0.306$ V ($x_1 = 0.1$) to $U_{cut} = 0.226$ V ($x_2 \sim 0.2$) (77 K), following the decrease in the band gap of the solid solution.

Figure 2b gives the electroluminescence spectra ($\tau = 5\ \mu$m, $f = 500$ Hz, $I = 3$ A) at 77 and 300 K, corrected to allow for the deterioration in the sensitivity of the photodetector at $\lambda > 5\ \mu$m. Similar spectra were obtained in the cw

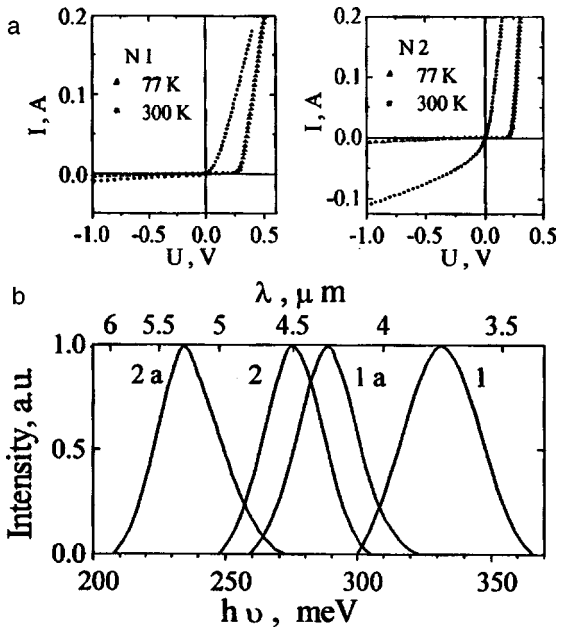

FIG. 2. a—Current-voltage characteristics (77, 300 K); b—electroluminescence spectra of structures No. 1: 77 K (1), 300 K (1a) and No. 2: 77 K (2), 300 K (2a).

mode. As the temperature increases from 77 to 300 K, the electroluminescence spectra shift toward lower energies and the radiation intensity decreases, as reported in Ref. 8, by a factor of $\sim$300 for sample No. 1 and by a factor of 16 for sample No. 2. Attention is drawn to the small change in the half-width which at 300 K is of the order of $\sim kT$. Figure 3 gives temperature dependences of the maximum energy (curve 1) and intensity (curve 4) of the electroluminescence for the structure with a narrow-gap $InAs_{0.8}Sb_{0.2}$ solid solution (No. 2). At $T = 175$ K the curve $h\nu(T)$ has a kink and the rate of temperature drift of the electroluminescence maximum increases to $\sim$0.26 meV/K ($T = 175$–300 K). Note that because of the high electron mobility, the p–n junction of the emitting region contains a p-region.

We postulate that two mechanisms, band-acceptor and band-band, are involved in the radiative recombination. Their superposition produces a fairly broad spectrum at low temperature ($\Delta h\nu_{1/2} \sim 25$ meV, 77 K). The energy of the acceptor level caused by the incorporation of Zn is $\sim$15 meV so that we predict that the acceptor level with saturate with increasing temperature, and at $T > 170$ K band-band recombination will predominate. To analyze the temperature dependence, we shall assume that the profile of the luminescence spectrum for the approximation of parabolic bands without carrier degeneracy is given by: $I(h\nu) \sim \sqrt{h\nu - E_g} \times \exp[-(h\nu - E_g)/kT]$, where $h\nu$ is the photon energy and E_g is the band gap. The band gap will then be $kT/2$ smaller than the energy of the luminescence peak (this condition is readily satisfied for binary InAs and InSb compounds and indicates that the law of conservation of momentum is satisfied). The thin dotted line in Fig. 3 (curve 2) gives the temperature dependence of the band gap for an $InAs/InAs_{0.8}Sb_{0.2}$ ternary solution in the range where band-band recombination predominates, obtained from the experimental dependence $h\nu_{max} = f(T)$, $E_g(T) = h\nu_{max}(T) - kT/2$. This curve has the same slope as the temperature dependence of the band gap of InAs: $E_g(T) = E_g(0) - 2.85\times10^{-4}\times T$ [meV] (curve 3, Fig. 3). This observation suggests that the epitaxial layer possesses good crystal quality and contains no disorder which could impair the law of conservation of the wave vector.[8]

To sum up, we have prepared and investigated graded-index $p-n$ structures of InAsSb/InAsSbP/InAs capable of emitting at the maximum of the spectral curve up to 5.4 μm with a half-width of $\sim$26 meV ($\sim$0.6 μm) without cooling. At present, this is the longest-wavelength radiation obtained at room temperature in III–V structures grown by liquid-phase epitaxy and the band is the narrowest obtained for semiconductor spontaneous radiation sources. These structures may provide the basis for efficient light-emitting diodes operating at room temperature and suitable for use in the spectroscopy of various gases, such as nitric oxide (NO).

In conclusion, the authors are grateful to Yu. P. Yakovlev for attention and interest in this work, and to T. I. Voronina, M. E. Vinogradova, A. V. Lunev, and N. D. Il'inskiĭfor technical assistance with this work.

[1] T. Ashley, C. T. Eliott, N. T. Gordon, R. S. Hall, A. D. Johnson, and G. J. Pryce, Appl. Phys. Lett. **64**, 2433 (1994).
[2] Rui Q. Yang, Chih-Hsiang Lin, S. J. Murry, S. S. Pei, H. C. Liu, M. Buchanan, and E. Dupont, Appl. Phys. Lett. **70**, 2013 (1997).
[3] X. Y. Gong, T. Yamaguchi, H. Kan, T. Makino, N. L. Rowell, Y. Lacroix, A. Mangyou, M. Aoyama, and M. Kumagawa, Jpn. J. Appl. Phys. **36**, 738 (1997).
[4] P. J. Tang, M. J. Pullin, C. C. Philips, R. A. Stradling, A. G. Norman, Y. B. Li, and L. Hart, Semicond. Sci. Technol. **10**, 1177 (1995).
[5] B. A. Matveev, N. M. Stus', and G. N. Talalakin, Kristallografiya. **32**, 216 (1988) [*sic*].
[6] M. Aĭdaraliev, N. V. Zotova, S. A. Karandashev, B. A. Matveev, N. M. Stus', and G. N. Talalakin, Pis'ma Zh. Tekh. Fiz. **17**(23), 75 (1991) [Sov. Tech. Phys. Lett. **17**, 852 (1991)].
[7] B. A. Matveev, G. A. Gavrilov, V. V. Evstropov, N. V. Zotova, S. A. Karandashov, G. Yu. Sotnikova, N. M. Stus, G. N. Talalakin, and J. Malinen, Sens. Actuators **38–39**, 339 (1997).
[8] Z. M. Fang, K. J. Ma, D. H. Jaw, R. M. Cohen, and G. B. Stringfellow, J. Appl. Phys. **67**, 7034 (1990).

Translated by R. M. Durham